1983

Experimental gas-solid reaction kinetics of lime sulfation

Daniel Walter Marsh
Iowa State University

INFORMATION TO USERS

This reproduction was made from a copy of a document sent to us for microfilming. While the most advanced technology has been used to photograph and reproduce this document, the quality of the reproduction is heavily dependent upon the quality of the material submitted.

The following explanation of techniques is provided to help clarify markings or notations which may appear on this reproduction.

1. The sign or "target" for pages apparently lacking from the document photographed is "Missing Page(s)". If it was possible to obtain the missing page(s) or section, they are spliced into the film along with adjacent pages. This may have necessitated cutting through an image and duplicating adjacent pages to assure complete continuity.

2. When an image on the film is obliterated with a round black mark, it is an indication of either blurred copy because of movement during exposure, duplicate copy, or copyrighted materials that should not have been filmed. For blurred pages, a good image of the page can be found in the adjacent frame. If copyrighted materials were deleted, a target note will appear listing the pages in the adjacent frame.

3. When a map, drawing or chart, etc., is part of the material being photographed, a definite method of "sectioning" the material has been followed. It is customary to begin filming at the upper left hand corner of a large sheet and to continue from left to right in equal sections with small overlaps. If necessary, sectioning is continued again—beginning below the first row and continuing on until complete.

4. For illustrations that cannot be satisfactorily reproduced by xerographic means, photographic prints can be purchased at additional cost and inserted into your xerographic copy. These prints are available upon request from the Dissertations Customer Services Department.

5. Some pages in any document may have indistinct print. In all cases the best available copy has been filmed.

University Microfilms International
300 N. Zeeb Road
Ann Arbor, MI 48106

Marsh, Daniel Walter

EXPERIMENTAL GAS-SOLID REACTION KINETICS OF LIME SULFATION

Iowa State University PH.D. 1983

Experimental gas-solid reaction kinetics of lime sulfation

by

Daniel Walter Marsh

A Dissertation Submitted to the
Graduate Faculty in Partial Fulfillment of the
Requirements for the Degree of
DOCTOR OF PHILOSOPHY

Major: Chemical Engineering

Approved:

Signature was redacted for privacy.

In Charge of Major Work

Signature was redacted for privacy.

For the Major Department

Signature was redacted for privacy.

For the Graduate College

Iowa State University
Ames, Iowa
1983

TABLE OF CONTENTS

NOMENCLATURE

a = gaseous reactant stoichiometric coefficient

$A(g)$ = symbol for gaseous reactant

A_ϕ = frequency factor for pore removal due to sintering

Ar = Arrhenius number, defined by Equation (32)

A_s = specific surface area of solid, m^2/g

b = solid reactant stoichiometric coefficient

$B(s)$ = symbol for solid reactant

Bi = D_{As}/kr_{go}, Biot number for a grain

Bi_m = modified Biot number, defined by Equation (47)

c = gaseous product stoichiometric coefficient

$C(g)$ = symbol for gaseous product

C_A = gaseous reactant concentration, $gmole/cm^3$

C_{Ab} = bulk gaseous reactant concentration, $gmole/cm^3$

C_{Ac} = gaseous reactant concentration at reaction interface, $gmole/cm^3$

C_{As} = gaseous reactant concentration at pellet surface, $gmole/cm^3$

C_B = solid reactant concentration, $gmole/cm^3$

C_{pb} = bulk gas heat capacity, cal/g^oK

C_{pB} = heat capacity of solid reactant, cal/g^oK

C_{pD} = heat capacity of solid product, cal/g^oK

C_{pe} = effective porous solid heat capacity, cal/g^oK

C_T = total gas concentration, $gmole/cm^3$

d = solid product stoichiometric coefficient

$D(s)$ = symbol for solid product

D = pellet diameter, cm

D_{AC} = molecular binary diffusivity of gases A and C, cm^2/sec

D_{ACe} = effective molecular binary diffusivity in product layer, cm^2/sec

D_{Ae} = effective intrapellet diffusivity, defined by Equation (55)

D_{As} = effective product layer diffusivity, cm^2/sec

D_{KA} = Knudsen diffusivity for gaseous species A, cm^2/sec

$\overline{D}_p$ = average particle diameter, cm

E_{ACT} = chemical reaction activation energy, cal/gmole

E_s = sintering activation energy, cal/gmole

h = gas phase heat transfer coefficient, cal/sec cm^2 ^oK

ΔH_{RXN} = heat of reaction per mole of A, cal/gmole

k = chemical reaction rate constant, cm/sec

k_o = frequency factor for chemical reaction, cm/sec

k_{cb} = bulk gas thermal conductivity, cal/sec cm ^oK

k_{cB} = thermal conductivity of solid reactant, cal/sec cm ^oK

k_{cD} = thermal conductivity of solid product, cal/sec cm ^oK

k_{ce} = effective pellet thermal conductivity, cal/sec cm ^oK

k_{cg} = thermal conductivity of gas phase, cal/sec cm ^oK

k_{MA} = gas phase mass transfer coefficient, cm/sec

K_o = parameter defined by Equation (57), cm

L = pellet length, cm

m_B = mass of solid reactant, g

M = 1 - c

M_i = molecular weight of species i

N_i = diffusive flux of species i, $gmole/cm^2$ sec

N_{As} = solid-state diffusive flux of species A, $gmole/cm^2$ sec

P = pressure, atm

r = radial grain position, cm

r_{go} = initial grain radius, cm

r_g = grain radius, cm

r_c = radius of grain unreacted-core, cm

R = radial pellet position, cm

R_p = pellet radius, cm

R_o = universal gas constant = 1.987 cal/gmole^oK

$\bar{R}_A$ = reaction rate per unit pellet volume, gmole/cm^3 sec

R_{Ac} = reaction rate per unit interface surface area, gmole/cm^2 sec

t = time, sec

t_{Tmax} = time at which maximum pellet center temperature occurred, sec

T = temperature, ^oK

T_b = bulk gas temperature, ^oK

T_c = Tammann temperature, ^oK

T_s = pellet surface temperature, ^oK

T_{max} = maximum pellet center temperature, ^oK

u_b = average bulk gas velocity, cm/sec

V_i = molar volume of species i, cm^3/gmole

X = local pellet conversion

X_p = volume average pellet conversion

y_o = initial slab thickness, cm

y_1 = slab thickness, cm

y_2 = reaction interface position in slab, cm

Y_A = intergrain mole fraction of A

Y_{Ab} = bulk gas mole fraction of A

Y_{Ac} = reaction interface mole fraction of A

Y_{Ag} = intragrain mole fraction of A

$\bar{Y}_A^G$ = volume average intragrain mole fraction of A

$\bar{Y}_A^P$ = volume average intergrain mole fraction of A

z = length coordinate, cm

Z_E = expansion coefficient

Greek

β_T = parameter defined by Equation (31)

δ_A = intergrain factor = $D_{Ae}/[D_{AC}(\epsilon/\tau)]$

δ_{SA} = intragrain factor = D_{As}/D_{ACe}

ϵ = pellet porosity, defined by Equation (49)

ϵ_o = initial pellet porosity

ϵ_{min} = minimum porosity

ρ_B = nonporous solid reactant molar density, gmole/cm^3

ρ'_B = nonporous solid reactant density, g/cm^3

ρ_D = nonporous solid product molar density, gmole/cm^3

ρ' = pellet density, g/cm^3

τ = pellet tortuosity

σ = Thiele-type parameter, defined by Equation (23)

σ_m = modified Thiele-type parameter, defined by Equation (46)

θ = dimensionless time

ζ_c = dimensionless zone boundary position

ζ_{ac} = average dimensionless zone boundary position

ν = bulk gas kinematic viscosity, cm^2/sec

I. INTRODUCTION

Producing energy from coal by fluidized bed combustion will become an important process in this decade. To control the sulfur emissions from this combustion process, limestone can be added to the fluidized bed combustor. At high temperature (800°C), the limestone ($CaCO_3$) calcines to form lime (CaO):

$$CaCO_3(s) \rightarrow CaO(s) + CO_2(g) \ .$$

The CaO then reacts with the SO_2, given off by the coal, by the following overall reaction at high temperature:

$$CaO(s) + SO_2(g) + \frac{1}{2} O_2(g) \rightarrow CaSO_4(s) \ .$$

At high temperature, the calcination reaction occurs more rapidly than the sulfation reaction and therefore, the sulfation reaction is rate determining.

One of the complicating features of lime sulfation is pore closure, due to the molar volume of calcium sulfate being larger than that of calcium oxide. Particles of CaO that are initially porous will react rapidly at first and then more slowly until the reaction essentially stops, usually before complete conversion. It has been shown [22] that the overall particle dimensions do not change appreciably during the reaction, but that the expanding solid product fills the void regions inside the particle until the pores are plugged and reaction ceases.

Recent interest has focused on the hydration of CaO to form $Ca(OH)_2$ and subsequent calcination of the calcium hydroxide to produce a more

highly porous form of CaO:

$$CaO + H_2O \rightarrow Ca(OH)_2$$

$$Ca(OH)_2 \rightarrow CaO + H_2O \ .$$

This highly porous lime would then be added to the combustor and would react to higher conversion levels, since higher overall conversion is favored by a highly porous solid structure.

Until recently, models of gas-solid reactions conceptualized the solid reactant as having no characteristic internal structure. In many reactions, including lime sulfation, the structural parameters of the solid will greatly affect the rate of reaction. These parameters include porosity, pore size distribution, and specific surface area. Structural models take these parameters into account and attempt to draw a more realistic picture of the physical system. Substantial advancement has been made in the development of gas-solid reaction models, but there is still a need for significant refinement.

Several structural models have been proposed and applied to lime sulfation. These models are variations of either the grain or the pore model. The grain model pictures the porous solid as being an agglomeration of dense grains that react according to the "shrinking unreacted-core model" [33]. In contrast, the pore model depicts a pellet as a solid containing a network of cylindrical pores. Since the pellets in this work were produced by pressing powder, the grain model may be a more realistic representation.

A systematic study of lime sulfation was performed using thermogravimetric analysis (TGA). The lime was produced by calcining reagent grade $Ca(OH)_2$. Use of this starting material provided a highly porous lime and eliminated the effects of chemical impurities, found in the calcines of most limestones, on the kinetic data. Kinetic data were obtained over a range of temperatures between 350° and 930°C and an SO_2 concentration range of 0.25 to 8.0 mole percent. At low temperatures, the major product of reaction was found to be $CaSO_3$, while at high temperatures, $CaSO_4$ was predominant. A quantitative measurement of the solid product distribution with temperature was made using the TGA. Reaction rate constants, activation energies and reaction orders were obtained for the formation of $CaSO_3$ and $CaSO_4$.

Mercury porosimetry, krypton adsorption, and scanning electron microscopy were used to study the effects of calcination and sulfation on $Ca(OH)_2$. The effects of sintering on the reaction kinetics were also observed. Solid-state diffusivity estimates were obtained by using two simple models applied to conversion-time data from the reaction of highly sintered CaO.

A one-dimensional expanding grain model was developed and applied to the conversion data from the sulfation of thin CaO pellets, presintered for varying amounts of time. The effects of a grain size distribution on model predictions were analyzed. In addition, a model was developed to include the effect of a continuously increasing or decreasing reaction temperature on the conversion-time behavior. This model was compared to experimental data.

II. REVIEW OF NONCATALYTIC GAS-SOLID REACTION MODELS

Chemical reactions between gases and porous solids are characterized by many interrelated mechanisms or steps. The overall reaction is the summation of these mechanisms and will thus depend on their interactions with each other. The following steps are visualized as occurring during reactions involving a porous solid and a gas [48]:

1. Mass transfer of gaseous reactant through an external gas film surrounding the solid pellet.
2. Diffusion of the gaseous reactant through the porous solid, which can consist of a mixture of solid reactant and product with solid density and porosity possibly changing during reaction.
3. Adsorption of the gaseous reactant on the surface of the solid.
4. Chemical reaction at the solid surface.
5. Desorption of the gaseous product from the surface of the solid.
6. Diffusion of the gaseous product from the interior to the surface of the pellet.
7. Mass transfer of gaseous product through the external gas film.

For reactions that are either exothermic or endothermic, the following heat transfer steps will accompany the reaction and diffusional steps:

1. Convective and possibly radiative heat transfer between the gas stream and the external solid surface.

2. Conductive heat transfer within the pellet, either in the inward or outward direction depending on whether the reaction is endothermic or exothermic, respectively.

The importance of each reaction step to the overall reaction depends on the particular reaction system and the specific conditions under interest. A useful gas-solid reaction model must take these steps into account. Numerous models have been proposed to simulate this type of reaction and may be roughly categorized as "nonstructural" and "structural" type models. Some of these models will be discussed here, but this by no means represents an exhaustive list.

The general reaction considered by most gas-solid reaction models is of the form

$$aA(g) + bB(s) \rightarrow cC(g) + dD(s) \qquad (1)$$

where a, b, c, and d are stoichiometric coefficients and g and s represent gas and solid, respectively.

A. Nonstructural Models

These models do not directly consider the structural parameters of the solid such as porosity, apparent density, or grain size distribution. However, they do make use of heterogeneous rate constants and diffusivities.

1. Homogeneous model

The basic assumption of this model is negligible pore diffusion resistance which results in a uniform gas concentration throughout the solid. Therefore, all the surface area is available for reaction and

the pellet reacts at a spatially uniform rate. External mass transfer resistance may or may not be neglected depending on the particular system. If this resistance is neglected, the concentration of gaseous reactant inside the solid becomes the same as the concentration in the bulk gas. If the reaction is zero order with respect to the solid and first order in gas concentration, a material balance on the solid gives the following relationship for conversion, X:

$$X = \frac{b}{a} kC_{Ab}t \tag{2}$$

where a and b are stoichiometric coefficients for the gas and solid, respectively, k is the kinetic rate constant, C_{Ab} is the bulk gas concentration (which equals the intrapellet concentration for no gas phase mass transfer resistance), and t represents time.

2. Shrinking unreacted-core model

The shrinking unreacted-core model by Levenspiel [33] visualizes the reaction as occurring at a sharp interface between the reacted and unreacted solid. During reaction, the interface moves inward leaving behind a porous solid product or "ash" layer.

The continuity equation for gaseous component, A, is given by

$$\epsilon \frac{\partial C_A}{\partial t} + \nabla N_A = - \bar{R}_A \tag{3}$$

where

C_A = molar concentration of A,

t = time,

N_A = molar flux of A,

$\bar{R}_A$ = molar rate of consumption of A per unit volume by chemical reaction, and

ϵ = pellet porosity.

Pseudo-steady state ($\frac{\partial C_A}{\partial t} = 0$) can be assumed if the rate of reaction interface movement is much slower than the rate of gaseous diffusion to the interface. This assumption has been evaluated by several investigators [33, 46, 53] and they have found that no significant error occurs for a solid to reactant gas molar density ratio greater than 1000. Most gas-solid systems have ratios exceeding 25,000, unless the operating pressures are extremely high.

Other assumptions made are an irreversible reaction, first order kinetics with respect to gaseous reactant, a sharp reaction interface, and equimolar counterdiffusion of product and reactant gases. For a spherical pellet, the above assumptions reduce the continuity equation for A in the ash layer to

$$r_{go} > r > r_c, \quad \frac{d}{dr}\left(r^2 \frac{dC_A}{dr}\right) = 0 \tag{4}$$

with the following boundary conditions:

$$\text{at } r = r_c, \; D_{As}\left(\frac{dC_A}{dr}\right)_{r_c} = k\, C_{Ac} \tag{5}$$

$$\text{and at } r = r_{go}, \; D_{As}\left(\frac{dC_A}{dr}\right)_{r_{go}} = k_{MA}(C_{Ab} - C_{As}) \tag{6}$$

where

r = Radial pellet position,

r_{go} = external radius of pellet,

r_c = unreacted-core radius,

D_{As} = product layer diffusion coefficient of A,

k = reaction rate constant,

k_{MA} = gas phase mass transfer coefficient,

C_{Ac} = gaseous reactant concentration at reaction interface,

C_{Ab} = bulk gaseous reactant concentration, and

C_{As} = gaseous reactant concentration at pellet surface.

Solving Equations (4-6) for the concentration profile of gaseous reactant A in the ash layer gives

$$\frac{C_A}{C_{Ab}} = \frac{\left[1 + \frac{D_{As}}{kr_c}\right]\frac{1}{r_c} - \frac{1}{r}}{\left[1 + \frac{D_{As}}{kr_c}\right]\frac{1}{r_c} - \left[1 - \frac{D_{As}}{k_{MA}r_{go}}\right]\frac{1}{r_{go}}} \quad . \tag{7}$$

The concentration at the reaction interface, C_{Ac}, can be found by substituting r_c for r in Equation (7). Rearrangement of the result gives

$$\frac{C_{Ac}}{C_{Ab}} = \frac{1}{1 + \frac{kr_c^2}{k_{MA}r_{go}^2} + \frac{kr_c}{D_{As}}\left(1 - \frac{r_c}{r_{go}}\right)} \quad . \tag{8}$$

The reaction rate per unit area, R_{Ac}, can then be expressed as

$$R_{Ac} = kC_{Ac} = \frac{kC_{Ab}}{1 + \frac{kr_c^2}{k_{MA}r_{go}^2} + \frac{kr_c}{D_{As}}\left(1 - \frac{r_c}{r_{go}}\right)} \quad . \tag{9}$$

Movement of the reaction interface, r_c, is described by the following differential equation:

$$-\frac{a\rho_B}{b}\frac{dr_c}{dt} = kC_{Ac} \tag{10}$$

with the initial condition

$$\text{at } t = 0,\ r_c = r_{go} .$$

Substituting C_{Ac} from Equation (8) into Equation (10) and then integrating gives a relation between reaction time and fractional conversion, X:

$$t = \frac{a\rho_B r_{go}}{bC_{Ab}}\left\{\frac{X}{3k_{MA}} + \frac{r_{go}}{6D_{As}}\left[1 + 2(1 - X) - 3(1 - X)^{2/3}\right]\right. \tag{11}$$

$$\left. + \frac{1}{k}\left[1 - (1 - X)^{1/3}\right]\right\}$$

where

ρ_B = solid reactant molar density, and

X = fractional conversion = $1 - \left(\frac{r_c}{r_{go}}\right)^3$.

The time required for complete conversion, t*, can be found by substituting X = 1 into Equation (11):

$$t^* = \frac{a\rho_B r_{go}}{bC_{Ab}}\left\{\frac{1}{3k_{MA}} + \frac{r_{go}}{6D_{As}} + \frac{1}{k}\right\} \tag{12}$$

where the three terms in brackets represent the respective relative resistances of mass transfer, product layer diffusion, and chemical reaction to the overall reaction.

Some examples of gas-solid reactions which closely follow the shrinking unreacted-core model are oxidation of zinc sulfide [17], reduction of iron oxide by hydrogen or carbon monoxide [30], and calcination of calcium carbonate to form calcium oxide [56].

3. Two stage model

Ishida and Wen [28] proposed the two stage model for gas-solid reactions. This model depicts the reaction as being faster near the surface than in the interior of the pellet due to diffusional limitations. The solid reactant at the surface is eventually completely reacted forming an inert product (ash) layer. This newly formed ash layer is called the diffusion zone and the rest of the pellet is the reaction zone.

The period of time prior to ash layer formation is referred to as stage I and the subsequent period is called stage II. Diffusion zone and reaction zone effective diffusivities are assumed to be constant and the reaction is assumed to be first order with respect to gaseous reactant concentration. For a spherical pellet, the relationship between solid conversion and time, during stage I, is given by

$$X = \frac{3}{\phi^2} (\phi \coth \phi - 1) \frac{\theta}{\theta^I} \quad . \tag{13}$$

The corresponding relationship for Stage II is as follows:

$$X = 1 - \zeta_c^3 + \frac{3\zeta_c}{\phi^2} [\phi \zeta_c \coth (\phi \zeta_c) - 1] \tag{14}$$

where the position of the moving boundary of completely exhausted solid, ζ_c, is found from the implicit equation:

$$\theta = 1 + \left(1 - \frac{D_{Ae}}{D'_{Ae}}\right) \ln \left[\frac{\zeta_c \sinh \phi}{\sinh (\phi \zeta_c)}\right] + \frac{\phi'^2}{6} (1 - \zeta_c)^2 (1 + 2\zeta_c)$$

$$+ \left[\frac{D_{Ae}}{D'_{Ae}} (1 - \zeta_c) + \frac{D_{Ae}}{k_{MA} R} \zeta_c\right] [(\phi \zeta_c) \coth (\phi \zeta_c) - 1]$$

$$+ \frac{D'_{Ae}}{k_{MA} R} \frac{\phi'^2}{3} (1 - \zeta_c^3) \qquad (15)$$

where

ϕ, ϕ' = Thiele modulus for reaction zone and diffusion zone, respectively = $R\sqrt{\frac{ak}{bD_{Ae}}}$,

θ = dimensionless time = $\frac{akC_A t}{bC_{Bo}}$,

θ^I = dimensionless time to complete stage I reaction,

ζ_c = dimensionless zone boundary position = $\frac{r_c}{R}$,

r_c = radial position of zone boundary,

R = pellet radius,

D_{Ae}, D'_{Ae} = effective diffusivity in the reaction and diffusion zones, respectively,

k = chemical reaction rate constant,

k_{MA} = gas phase mass transfer coefficient,

C_{Bo} = initial concentration of solid reactant, and

C_A = concentration of gaseous reactant.

For $D_{Ae} \ll D'_{Ae}$, the two stage model gives the same result as the shrinking unreacted-core model.

4. Zone reaction model

Experiments have shown that for certain gas-solid reaction systems the reaction takes place in a diffuse reaction zone. This region is bounded by the solid product and the unreacted solid. The zone reaction model was proposed by Bowen and Cheng [8] to explain this phenomenon.

They made the following assumptions in deriving this model:

1. The reaction zone is narrow and the variation of gaseous and solid concentration through the reaction zone is linear.
2. The reaction has respectively n^{th} and m^{th} order dependence on the gaseous and solid reactants.

Given these assumptions, the reaction rate, R_A, is given by

$$R_A = 4\pi \zeta_{ac}^2 (\nu' D_{Ae} k\psi)^{1/2} C_{Ao}^{(n+1)/2} C_{Bo}^{m/2} \tag{16}$$

where

$$\psi = \frac{1}{n+1} - \frac{m}{n+2} + \frac{m(m-1)}{2!(n+3)} - \frac{m(m-1)(m-2)}{3!(n+4)} , \tag{17}$$

ζ_{ac} = average dimensionless reaction zone position,

ν' = ratio of the gas concentration gradient in the reaction zone at the product interface to the mean linear gradient across the zone,

C_{Ao} = bulk gaseous reactant concentration, and

C_{Bo} = initial solid concentration.

B. Structural Models

These models take into account the structural properties of the solid reactant and the solid product. Structural parameters such as grain size and its distribution, pore size and its distribution, and porosity are taken into account in the development of the models. Therefore, the reaction rate constants and pore diffusion coefficients retain their physical meaning and can be determined independently.

1. Pore model

The pore model depicts a porous solid as containing a network of cylindrical pores. The reaction is seen as occurring on the walls of the pores initially, with the reaction front moving into the solid as time progresses.

A pore model proposed by Szekely and Evans [47] considers the solid to have parallel pores which are of equal radius and equally spaced. To simplify the mathematical treatment, the particle is considered to be infinitely thick and isothermal. A similar development was made by Ramachandran and Smith [39], but they also accounted for pore plugging due to an expanding product.

The distributed pore size model developed by Christman and Edgar [12] accounts for changes in pore structure with extent of reaction for a solid containing pores of various sizes. The evolution of the pore size distribution is obtained by numerical simulation with the experimentally measured pore size distribution as an initial condition. A similar development was performed by Bhatia and Perlmutter [3] who allowed for an arbitrary pore size distribution and

accounted for the random overlap of reacting surfaces as reaction proceeds. They also took into account external mass transfer resistance.

2. Grain model

The grain model views the solid as being a random grouping of dense grains that react according to the shrinking unreacted-core model. This model may be a more realistic representation than the pore model for solids made by pressing powder. The reactant gas diffuses from the bulk gas stream to the pellet surface and then diffuses between the grains and through the solid product layer surrounding each grain until it reaches the reaction surface and reacts (see Figure 1).

It is generally assumed that the overall pellet dimensions do not change during the reaction, while the size of the grains may change depending on the relative molar volumes of the solid product and reactant.

a. Simplified grain model The general reaction considered by this model is given by Equation (1), where henceforth it will be assumed that a = 1.

Szekely and Evans [47] and Calvelo and Smith [10] developed the initial formulation of the grain model independently. Their developments differ by Szekely's use of a generalized grain shape factor, which allows for different grain shapes, and an analysis of reaction reversibility.

The simplifying assumptions made in the development of the model are:

1. Negligible external mass transfer resistance.

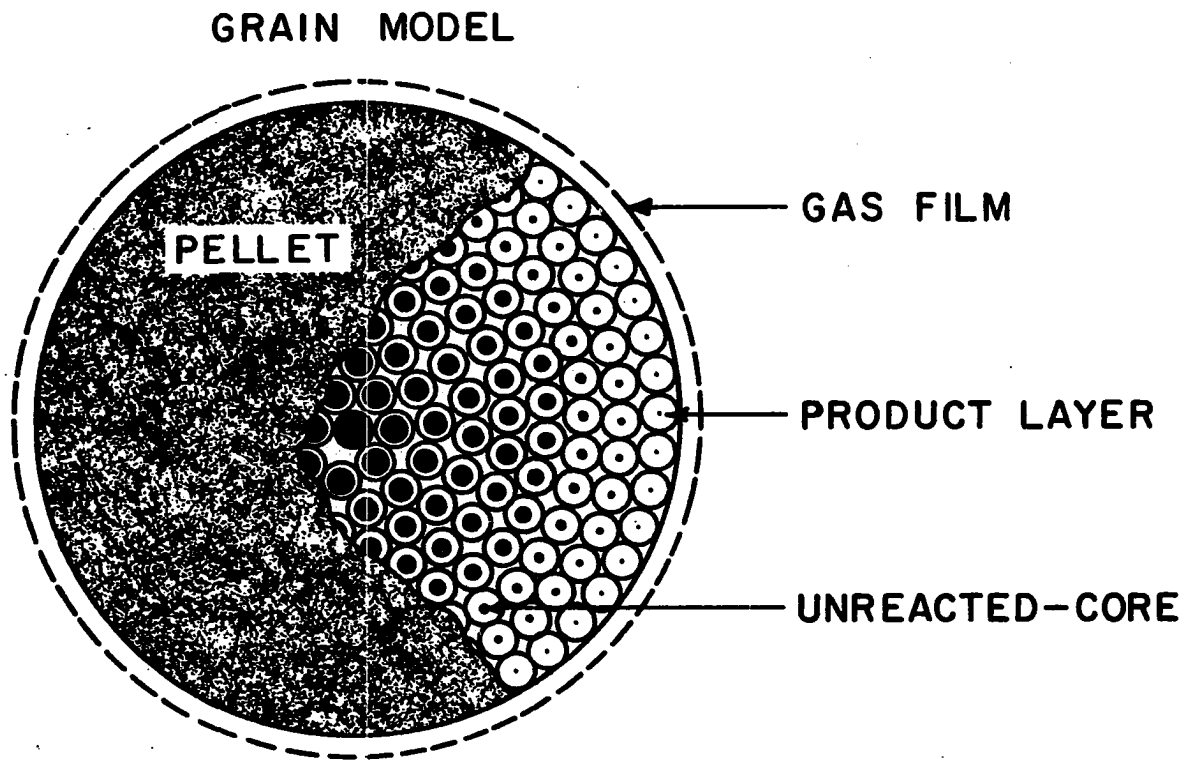

Figure 1. Depiction of the grain model

2. Solid structure is macroscopically uniform and unaffected by the reaction.
3. Isothermal pellet.
4. Equimolar counterdiffusion, or low reactant gas concentration.
5. Irreversible, first order chemical reaction.
6. Spherical pellet and grains.
7. Constant intrapellet diffusivity, D_{Ae}, and product layer diffusivity, D_{As}.
8. Pseudo-steady state.
9. Grains react according to the shrinking unreacted-core model.

Using these assumptions, a mass balance on a spherical pellet gives

$$R_P > R > 0, \quad D_{Ae}\left[\frac{d^2C_A}{dR^2} + \frac{2}{R}\frac{dC_A}{dR}\right] - \bar{R}_A = 0 \tag{18}$$

with boundary conditions

$$\text{at } R = 0 \text{ (pellet center)}, \quad \frac{dC_A}{dR} = 0 \tag{19}$$

$$\text{and at } R = R_P \text{ (pellet surface)}, \quad C_{As} = C_{Ab} \tag{20}$$

where

D_{Ae} = effective intergrain diffusion coefficient,

R = pellet radial position,

R_P = pellet radius, and

$\bar{R}_A$ = reaction rate per unit volume.

The reaction rate per unit volume, $\bar{R}_A$, is related to the rate per grain

unit area, R_{Ac}, as follows:

$$\bar{R}_A = \frac{3(1 - \epsilon_o)r_c^2}{r_{go}^3} R_{Ac} \tag{21}$$

where

ϵ_o = pellet porosity,

r_c = intragrain reaction interface position,

r_{go} = external grain radius, and

R_{Ac} = reaction rate per grain unit area.

The term multiplying R_{Ac} in Equation (21) represents the reaction interfacial area per unit volume.

An expression for R_{Ac} was developed in the analysis of the shrinking unreacted-core model and is given by Equation (8):

$$R_{Ac} = \frac{kC_{Ab}}{1 + \frac{kr_c^2}{k_{MA}r_{go}^2} + \frac{kr_c}{D_{As}}(1 - \frac{r_c}{r_{go}})} \tag{8}$$

Neglecting external mass transfer resistance around each grain ($k_{MA} \rightarrow \infty$) leads to the following expression for $\bar{R}_A$:

$$\bar{R}_A = \frac{3(1 - \epsilon_o)r_c^2 kC_A}{r_{go}^3 [1 + \frac{r_c k}{D_{As}}(1 - \frac{r_c}{r_{go}})]} \tag{22}$$

It should be noted that the bulk gas concentration, C_{Ab}, referred to in the shrinking unreacted-core analysis of the individual grains is not the same as the bulk gas concentration outside the pellet, but instead corresponds to the local gas concentration, C_A, in the void region near the particular grain in question. Therefore, each grain "sees" a different bulk concentration outside its surface.

If Equation (18) is made dimensionless, two important parameters will appear: σ, a Thiele-type modulus and Bi, the Biot number for the grain. These dimensionless parameters are defined as follows:

$$\sigma = R_p \left[\frac{3(1 - \epsilon_o)k}{D_{Ae} r_{go}}\right]^{1/2} \tag{23}$$

$$Bi = \frac{D_{As}}{k r_{go}} \quad . \tag{24}$$

σ measures the relative importance of chemical kinetics and intergrain (pore) diffusion, while Bi indicates the relative importance of intragrain (solid product) diffusion and chemical kinetics.

The effects of varying σ and Bi on conversion versus time was illustrated by Calvelo and Smith [10]. The effect of intergrain diffusion resistance is determined by the effect of varying σ at constant Bi. Figure 2 shows that conversion at any given time decreases with increasing intergrain diffusion resistance (σ increasing). The effect of product layer (intragrain) diffusion resistance can be found by varying Bi at constant σ and k as shown in Figure 3. Conversion at any given time increases with decreasing product layer diffusion resistance

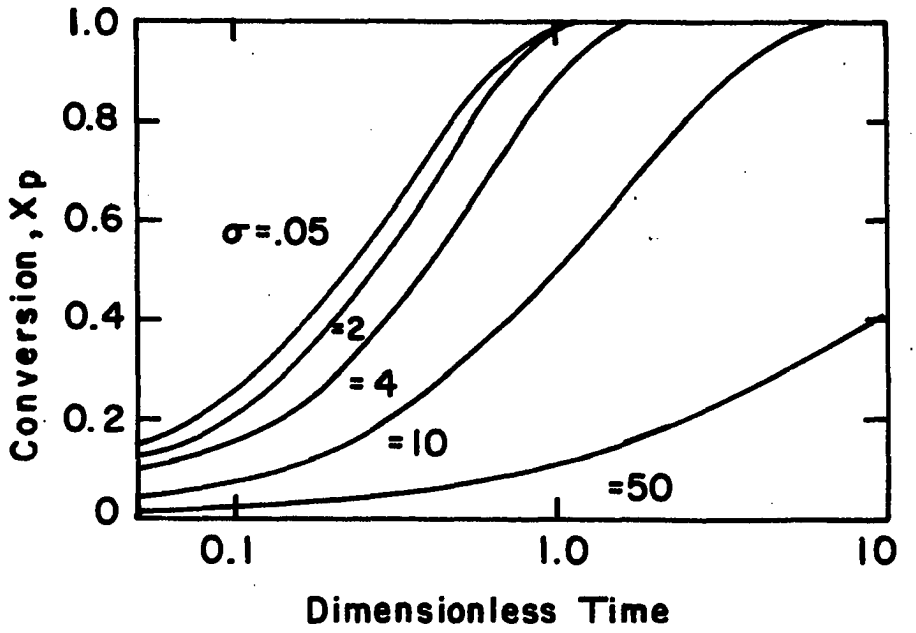

Figure 2. Effect of intergrain diffusion on conversion for Bi = 1.0 [10]

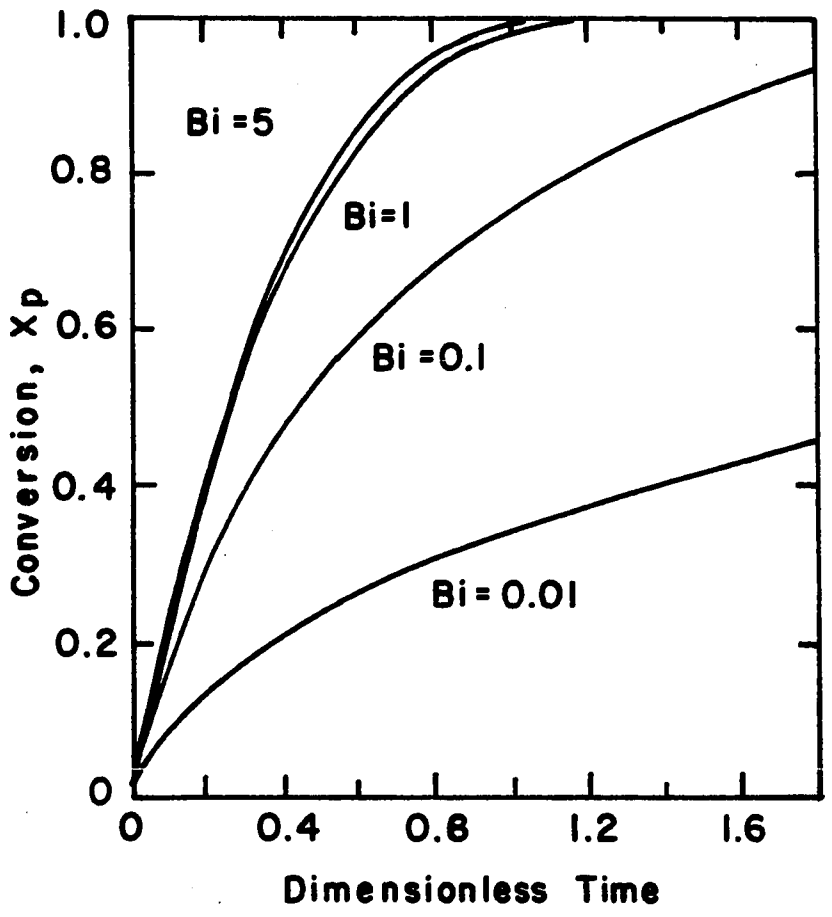

Figure 3. Effect of product layer diffusion on conversion for $\sigma = 2.0$ [10]

(increasing Bi).

The reaction of porous nickel oxide with hydrogen is predicted fairly well by the simplified grain model [49]; however, reactions that are characterized by a porosity decrease, due to an expanding product, cannot be accurately described by this model. Such a reaction is the sulfation of lime.

b. Expanding grain model Hartman and Trnka [24] modified the simplified grain model by accounting for grain expansion. The expanding grain radius, r_g, is related to local conversion, X, by the following:

$$r_g = r_{go} [1 + (Z_E - 1)X]^{1/3} \qquad (25)$$

where

r_g = expanding grain radius,

r_{go} = initial grain radius,

X = local conversion = $1 - (\frac{r_c}{r_{go}})^3$,

Z_E = expansion coefficient = $\rho_B d/\rho_D b$,

ρ_B = reactant solid molar density,

ρ_D = product solid molar density, and

b, d = stoichiometric coefficients (Equation 1).

r_{go} in Equation (8) is replaced by r_g in Equation (25); however, r_{go} in the specific reaction interfacial area term $(3(1 - \epsilon_o)r_c^2/r_{go}^3)$ of Equation (21) remains the same.

In addition, Mason and coworkers [34, 35] accounted for the effect of expanding grains on intergrain diffusion by expressing the effective

intergrain diffusion coefficient, D_{Ae}, as a function of the local porosity, ϵ:

$$D_{Ae} = \frac{1}{\frac{1}{D_{KA}} + \frac{1}{D_{AC}\epsilon^2}} \tag{26}$$

where

D_{KA} = Knudsen diffusion coefficient,

D_{AC} = binary molecular diffusion coefficient,

ϵ = local porosity = $\epsilon_o - (1 - \epsilon_o)(Z_E - 1)X$, and

ϵ_o = initial pellet porosity.

Therefore, as the reaction proceeds the expanding product around each grain causes a decrease in local porosity which reduces the effective diffusivity. This increase in diffusional resistance results in a lower reaction rate.

c. Grain model with grain size distribution One of the shortcomings of the grain model is that a uniform grain size must be assumed in order to obtain a system of differential equations that is readily solvable. Bartlett et al. [1] looked at a system with distributed grain sizes, but only considered the case of chemical reaction control.

Szekely and Propster [50] extended the simplified grain model to include a grain size distribution and considered three distributions (Gates-Gaudin-Schuhman, log-normal, and normal). By using approximate solutions, they found that the grain model predictions were substantially affected by the grain size distribution, where each distribution had

identical mean grain size values. Therefore, ignoring the grain size distribution in a mathematical model may impair the representation of experimental data.

d. Nonisothermal grain model If the reaction is highly exothermic (or endothermic), the pellet may generate (or consume) enough heat to induce substantial temperature gradients within the pellet. Since the effective intergrain and intragrain diffusivities, reaction rate constant, and total gas concentration are all functions of temperature, the resulting concentration profile, and ultimately conversion, will differ from that of an isothermal pellet. The magnitude of the temperature effect is a function of the effective pellet thermal conductivity, effective pellet heat capacity, heat of reaction, and heat transfer coefficient between the pellet surface and bulk gas stream. The grains are usually small enough to be considered isothermal.

Calvelo and Smith [10] incorporated an energy balance into the development of their grain model to determine the effects of a temperature gradient. They assumed negligible external heat and mass transfer resistances and pseudo-steady state. They also assumed constant heat of reaction, ΔH_{RXN}, and constant effective thermal conductivity, k_{ce}. With these assumptions, the energy balance gives

$$k_{ce}\left(\frac{d^2T}{dR^2} + \frac{2}{R}\frac{dT}{dR}\right) + \frac{(-\Delta H_{RXN})3(1 - \epsilon_o)r_c^{\,2}C_A k}{r_{go}^{\,3}\left[1 + \frac{r_c k}{D_{As}}\left(1 - \frac{r_c}{r_{go}}\right)\right]} = 0 \qquad (27)$$

with the boundary conditions

$$\text{at } R = 0, \frac{dT}{dR} = 0 \tag{28}$$

$$\text{and at } R = R_p, T_s = T_b \tag{29}$$

where

k_{ce} = effective pellet thermal conductivity,

T = pellet temperature,

T_s = pellet surface temperature,

T_b = bulk gas temperature,

k = reaction rate constant = $k_o \exp \frac{-E_{ACT}}{R_o T}$,

k_o = frequency factor,

E_{ACT} = activation energy, and

R_o = universal gas constant.

If the effective diffusivity, D_{Ae}, is assumed constant, Equation (27) can be combined with Equations (18) and (22) and then integrated to give the Damköhler relation:

$$T - T_s = \frac{(-\Delta H_{RXN})D_{Ae}(C_{As} - C_A)}{k_{ce}} \tag{30}$$

where C_{As} is the gaseous reactant concentration at the pellet surface. Using Equation (30), the energy balance can be eliminated from the analysis.

The effect of intrapellet temperature gradients on the conversion versus time curve using the grain model and the previous assumptions is

shown in Figure 4. The dimensionless parameters β_T and Ar are defined as follows:

$$\beta_T = \frac{(-\Delta H_{RXN})D_{Ae}C_{Ab}}{T_b k_{ce}} \tag{31}$$

$$Ar = -\frac{E_{ACT}}{R_o T_b} \quad . \tag{32}$$

Sampath et al. [43] derived a nonisothermal grain model without neglecting external heat and mass transfer resistance and without assuming pseudo-steady state. Therefore, their mass and energy balance equations included a transient term for concentration and temperature, respectively. The resulting system of nonlinear partial differential equations was solved using orthogonal collocation.

A comparison of the maximum temperatures in the pellet as a function of time, calculated from the pseudo-steady state and transient models, is shown in Figure 5. Maximum temperature refers to the overall maximum in the pellet at any given time and does not refer to the temperature at any particular radial position in the pellet. The dimensionless parameters N_1 and N_2 indicated in Figure 5 are defined as

$$N_1 = \frac{\varepsilon_o R^2 M_B C_{Ab} b k_o}{D_{Ae} \rho_B' r_{go}} \tag{33}$$

$$N_2 = \frac{R^2 \rho' C_p M_B C_{Ab} b k_o}{k_{ce} \rho_B' r_{go}} \tag{34}$$

where

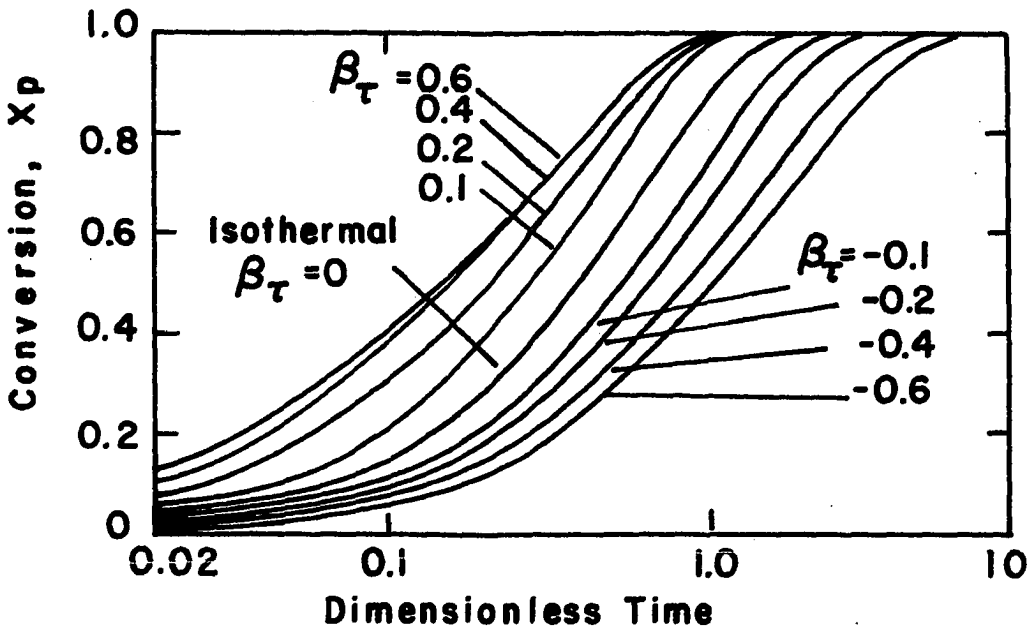

Figure 4. Nonisothermal behavior, conversion versus time with $\sigma = 4.0$, Bi = 1.0, and Ar = 20 [10]

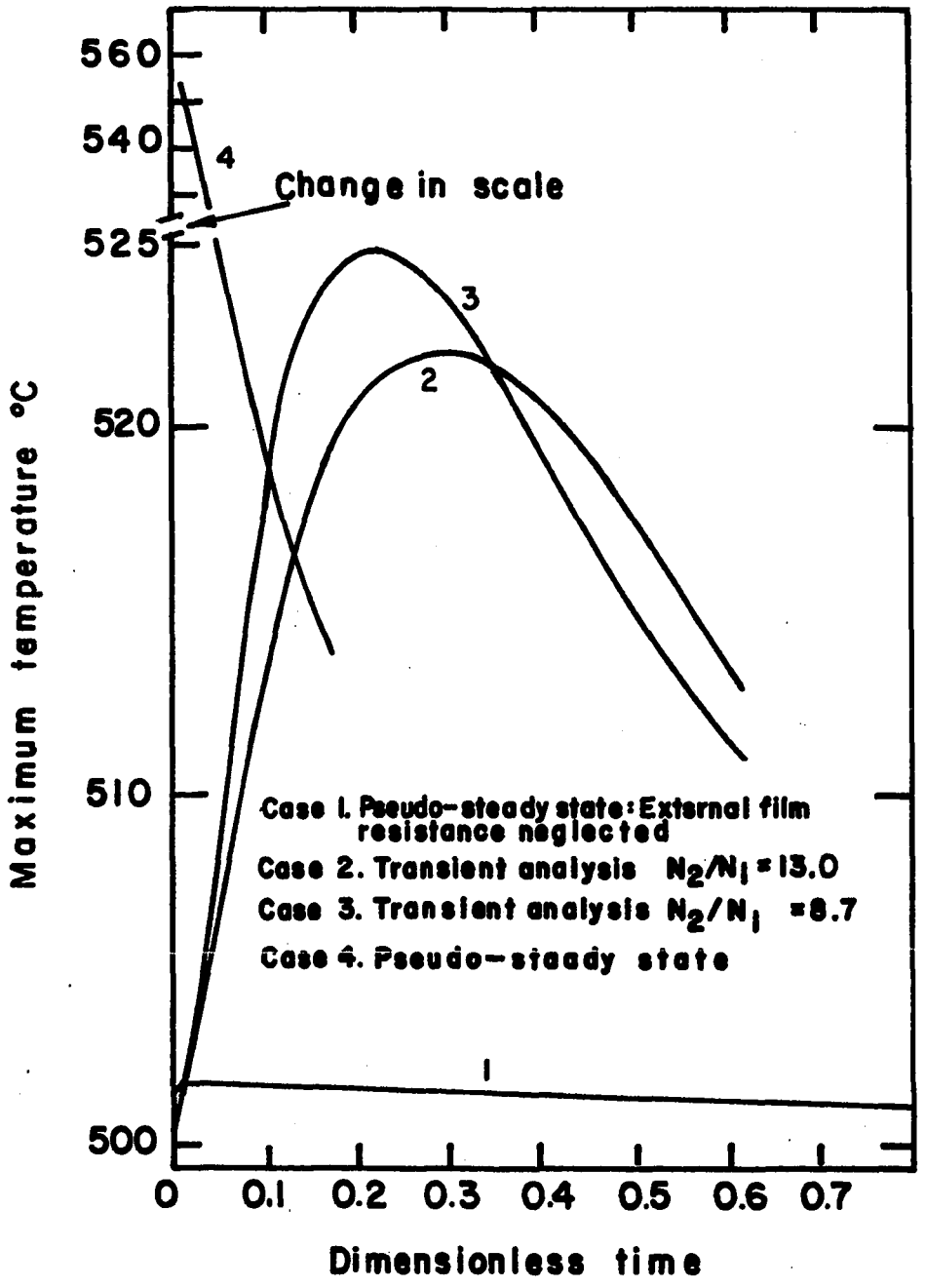

Figure 5. Comparison of the maximum temperature profile generated by the transient and pseudo-steady state models [43]

M_B = molecular weight of solid reactant,

C_p = average specific heat of the solid,

k_o = frequency factor,

ρ' = pellet density,

ρ_B' = nonporous solid reactant density, and

b = stoichiometric coefficient.

The ratio of N_2/N_1 reduces to

$$\frac{N_2}{N_1} = \frac{\rho' C_p D_{Ae}}{\varepsilon_o k_{ce}} \tag{35}$$

and therefore represents the ratio of the intrapellet heat transfer and diffusional resistances. Lower values of this ratio decrease the amount of time necessary for the system to obtain pseudo-steady state. Cases 2 and 3 (Figure 5) illustrate this effect. The pseudo-steady state analysis (cases 1 and 4) shows an instantaneous rise of temperature to a peak value, while the transient analysis shows that the peak value is reached only after a substantial elapse of time. This transient result is similar to the experimental results of Calvelo and Smith [10] where they measured the surface and center temperatures of a 1.0 cm diameter UO_2 pellet during a hydrofluorination reaction. The maximum temperature at each of these pellet locations did not occur until a definite amount of time had elapsed, especially for the center temperature which took approximately 2.0 minutes to attain its maximum. Since the highest rates of conversion occur at early reaction time, it may be

important to include the transient terms in the energy balance to adequately account for temperature effects in pellets of considerable size.

Comparison of cases 1 and 4 shows the effect of external film resistance. Neglecting this resistance results in a maximum temperature rise of $2^{o}C$ whereas including its effect gives a $55^{o}C$ maximum temperature rise for the particular reaction conditions under consideration.

e. Generalized grain model Yake [57] developed a generalized grain model which takes into account the combined effects of bulk flow (resulting from a net generation or consumption of reactant), reversible reaction, and pore closure. Assuming pseudo-steady state, negligible gas phase mass transfer resistance, isothermality, and a first order reversible reaction, a mass balance on a spherical pellet gives the following intergrain continuity equation for gaseous reactant, A:

$$\frac{d^2Y_A}{dR^2} + \frac{2}{R}\frac{dY_A}{dR} + \frac{M\delta_A}{1 - M\delta_A Y_A}\left(\frac{dY_A}{dR}\right)^2 - \bar{R}_A \frac{(1 - M\delta_A Y_A)}{D_{Ae}C_T} = 0 \qquad (36)$$

with the boundary conditions

$$\text{at } R = 0, \frac{dY_A}{dR} = 0 \qquad (37)$$

$$\text{and at } R = R_p, Y_A = Y_{Ab} \qquad (38)$$

where

$\bar{R}_A$ = gaseous reactant consumption term

$$= 3(1 - \epsilon_o) \frac{r_c^2}{r_{go}^3} k\left(\frac{Y_{Ac} - Y_{Ae}}{1 - Y_{Ae}}\right) , \qquad (39)$$

Y_A = intergrain mole fraction of A,

Y_{Ac} = reaction interface mole fraction of A,

Y_{Ae} = equilibrium mole fraction of A,

C_T = total concentration,

M = 1 - c,

c = stoichiometric coefficient (Equation 1),

δ_A = intergrain factor = $D_{Ae}\tau/D_{AC}\epsilon$,

τ = pellet tortuosity,

ϵ = pellet porosity, and

ϵ_o = initial pellet porosity.

In order to relate the reaction interface concentration to the intrapellet concentration at any given pellet position, the following intragrain continuity equation was solved:

$$\frac{d}{dr}\left(\frac{r^2 D_{As} C_T}{1 - M\delta_{SA} Y_{Ag}} \frac{dY_{Ag}}{dr}\right) = 0 \qquad (40)$$

with the boundary conditions

$$\text{at } r = r_g, \; Y_{Ag} = Y_A \qquad (41)$$

$$\text{and at } r = r_c, \; \left[\frac{D_{As} C_T}{1 - M\delta_{SA} Y_{Ag}} \frac{dY_{Ag}}{dr}\right]_{r_c} = kC_T\left(\frac{Y_{Ac} - Y_{Ae}}{1 - Y_{Ae}}\right) \qquad (42)$$

where

Y_{Ag} = intragrain mole fraction of A,

δ_{SA} = intragrain factor = D_{As}/D_{ACe}, and

D_{ACe} = effective binary diffusivity in product layer.

The analytical solution to Equation (40) is

$$\frac{1 - M\delta_{SA}Y_{Ac}}{1 - M\delta_{SA}Y_{A}} = \exp\left[\frac{kr_{go}M\delta_{SA}}{D_{As}(1 - Y_{Ae})}(Y_{Ac} - Y_{Ae})\left(\frac{r_c}{r_{go}}\right)\left(1 - \frac{r_c}{r_g}\right)\right] \quad (43)$$

where

$$r_g = r_{go}\left[1 + (Z_E - 1)X\right]^{1/3} . \quad (25)$$

Yake obtained the intrapellet concentration profile by solving Equations (36-39) using a finite difference technique. The corresponding reaction interface concentrations were calculated after each iteration by solving Equation (43) using the Regula-Falsi method. An estimate of the reaction interface position for each successive time step at any given radial position was calculated by the following expression:

$$r_c|_{t + \Delta t} = r_c|_t - \Delta t \left(\frac{bkC_T(Y_{Ac} - Y_{Ae})}{\rho_B(1 - Y_{Ae})}\right) \quad (44)$$

where Δt = time step. Overall pellet conversion was determined by numerically integrating the local conversion, X, over the pellet volume:

$$X_P = \frac{3}{R_P^3}\int_0^{R_P} XR^2 dR . \quad (45)$$

Using the bulk flow parameters $M\delta_A$ and $M\delta_{SA}$ and the reversible reaction parameter $(1 - Y_{Ae})$, Yake proposed a modified Thiele-type modulus:

$$\sigma_m = R_P \left[\frac{3(1 - \epsilon_o)k(1 - M\delta_A \bar{Y}_A^P)}{D_{Ae} r_{go}(1 - Y_{Ae})} \right]^{1/2} \tag{46}$$

and a modified Biot number:

$$Bi_m = \frac{D_{As}(1 - Y_{Ae})}{k r_{go}(1 - M\delta_{SA} \bar{Y}_A^G)} \tag{47}$$

where $\bar{Y}_A^P$, $\bar{Y}_A^G$ = volume average intergrain mole fraction and intragrain mole fraction of A, respectively.

An analysis of bulk flow and reversibility effects was presented using these two modified parameters.

f. Effect of sintering Sintering is the phenomenon by which the density of a porous solid increases while being held at a temperature below its melting point. In addition, porosity and surface area can be considerably affected.

The activation energies for sintering are high, meaning the rate of sintering increases rapidly with increasing temperature. Below a solid's Tammann temperature (.4 to .5 times the melting point), negligible sintering takes place, but above this temperature it can rapidly occur.

The principal driving force for sintering is the difference in surface energy between the unsintered and sintered solid surfaces. As sintering occurs, the surface area of the solid decreases, thus

decreasing the surface energy.

Several mechanisms have been proposed for sintering [48]:

1. Volume diffusion - This mechanism proceeds by a diffusion of atoms through the grains to the grain boundaries where "necks" form between individual grains.
2. Surface diffusion - This mechanism involves the migration of atoms across the grain surface to the necks.
3. Evaporation-condensation - The vapor pressure above a convex solid surface exceeds that above a concave surface. This difference causes evaporation from most of the grain surfaces and condensation in the necks between the grains.
4. Grain boundary diffusion - This mechanism proposes diffusion of vacancies from the necks via the grain boundaries.

Most solids are believed to sinter by grain boundary or volume diffusion, although surface diffusion may be significant at low temperatures or small particle sizes.

Kim and Smith [31] related the effects of sintering on the diffusion rate in nickel oxide pellets. Their resulting model related the pellet tortuosity, τ, to pellet porosity, ϵ, and this result was found to fit experimental data better than the random pore model ($\tau = 1/\epsilon$), as shown in Figure 6. They also studied the effect of chemical reduction on nickel oxide pellets that were initially sintered or unsintered. For pellets that were initially sintered, the diffusion rate increased greatly with extent of reduction and for pellets initially unsintered, the diffusion rate decreased slightly with extent of reduction. The

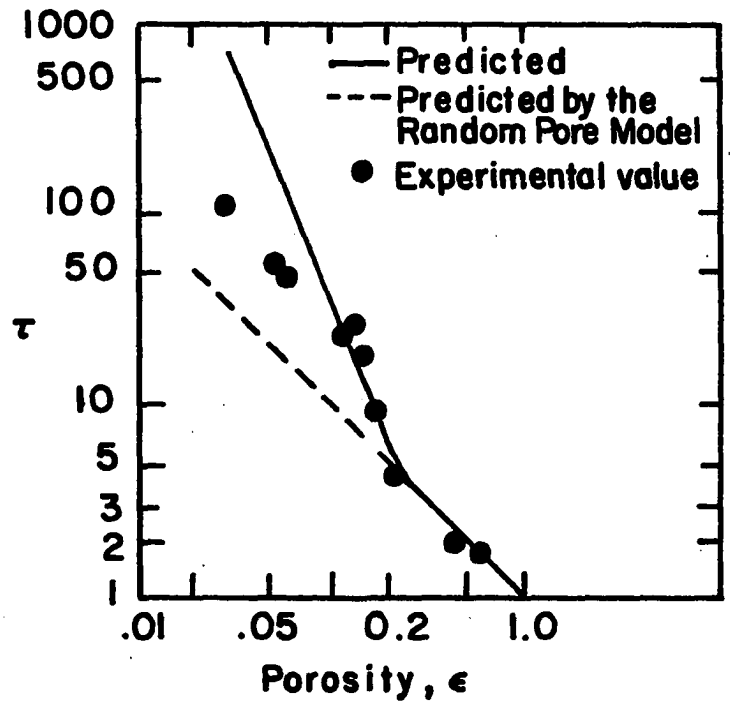

Figure 6. Predicted and experimental tortuosity factors for unreduced pellets, both sintered and unsintered [31]

number of pore interconnections was postulated to increase during reduction and thus a higher diffusion rate resulted for pellets initially sintered; however, this increase in pore interconnections was offset by a decrease in the same, caused by local sintering during reaction, for pellets that were initially unsintered.

Ranade [41] developed a model that considers grain growth as occurring by the combined mechanisms of sintering and conversion. The effects of sintering and conversion on the reactant solid specific surface area were determined independently for the gas-solid reaction involving ZnO and H_2S. These quantitative effects were then combined to obtain the simultaneous effect. By relating specific surface area to grain size, the grain model was modified to account for sintering and conversion occurring simultaneously. A comparison of the modified grain model predictions with the grain model and with experimental data is shown in Figure 7.

Ramachandran and Smith [40] also proposed a modification of the grain model to account for sintering. They used a correlation developed by Kim and Smith [31] that relates pellet tortuosity, τ, to the fraction of pores removed, ϕ, due to sintering. The variation of ϕ with time was modelled as a first-order rate process governed by an Arrhenius-type equation:

$$\frac{d\phi}{dt} = (1 - \phi)\, A_\phi \exp\left[- \frac{E_s}{R_o(T - T_c)}\right] \qquad (48)$$

where

ϕ = fraction of pores removed due to sintering,

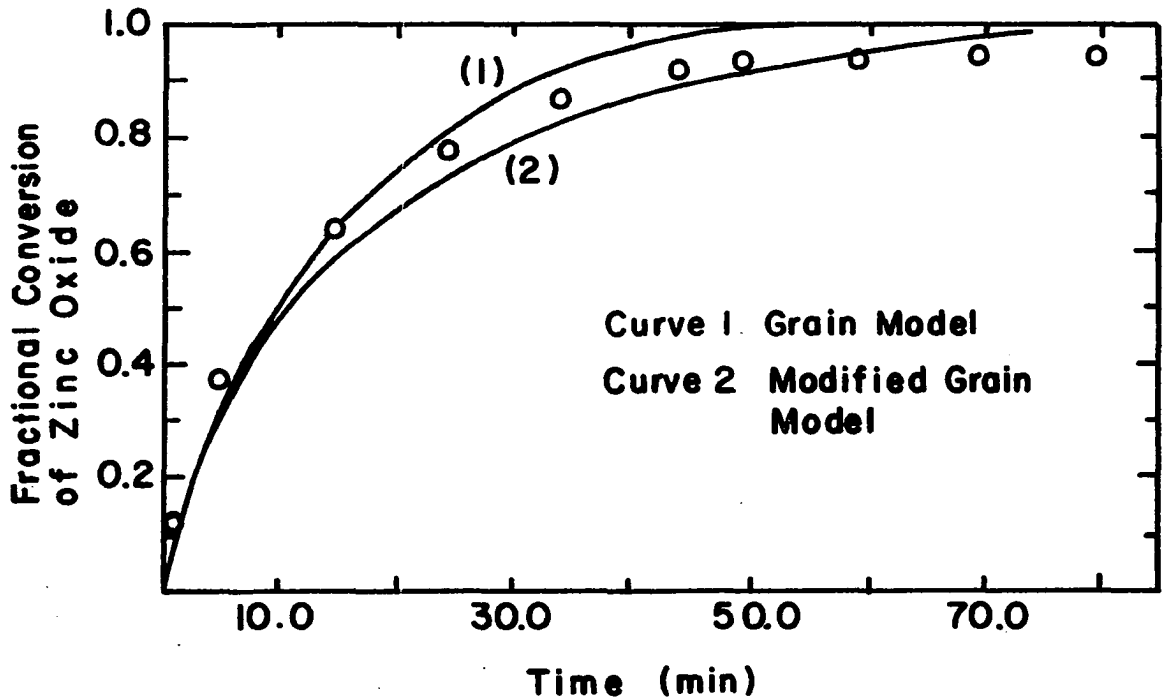

Figure 7. Comparison of predicted and experimental conversions for the reaction between ZnO and H_2S [41]

A_ϕ = frequency factor,

E_s = activation energy for the sintering process,

R_o = gas constant,

T = temperature, and

T_c = Tammann temperature.

The parameters A_ϕ, E_s, and T_c would have to be estimated using independent sintering experiments.

Ramachandran and Smith's modified grain model was compared to experimental data obtained by Calvelo and Smith [10] on the hydrofluorination of UO_2. However, it was determined that sintering for this system was negligible and therefore, the model's accuracy in predicting sintering effects was not tested.

3. Evaluation of model parameters

Most of the parameters used in gas-solid reaction models can be estimated a priori from known correlations. One exception is the chemical reaction rate constant, k, and its associated activation energy, E_{ACT}, which must be determined experimentally. Another exception is the product layer diffusion coefficient, D_{As}, for which no known correlation exists and for which no experimental measuring technique has previously been developed. D_{As} is usually determined by adjusting the value in a given model to obtain the best fit of experimental data. Evaluating D_{As} in this fashion inherently assumes that the model does indeed describe the system accurately and that the set of parameter values thus obtained is mutually exclusive. This inherent assumption could be avoided by developing an experimental method to directly measure

the product layer diffusivity. Such a method has been developed in this research effort and will be described later.

The pellet porosity is usually taken to be a linear function of local conversion for reactions characterized by product layer expansion [23]:

$$\epsilon = \epsilon_o - (1 - \epsilon_o)(Z_E - 1)X \tag{49}$$

where

ϵ = local pellet porosity,

ϵ_o = initial pellet porosity,

Z_E = expansion coefficient = $\rho_B d/\rho_D b$, and

X = local conversion.

Mercury penetration porosimetry can be used to experimentally determine initial pellet porosity, ϵ_o, as well as overall pellet porosity at different conversion levels.

Effective porous solid heat capacity, C_{pe}, can be treated as a weighted average of the solid reactant and product heat capacities:

$$C_{pe} = (1 - \epsilon)\,[(1 - X)\,C_{pB} + XC_{pD}] \tag{50}$$

where

C_{pe} = effective porous solid heat capacity, and

C_{pB}, C_{pD} = heat capacity of solid reactant and product, respectively.

Similarly, the effective pellet thermal conductivity, k_{ce}, can be related to the thermal conductivities of the solid reactant and product:

$$k_{ce} = (1 - \varepsilon)\,[(1 - X)\,k_{cB} + Xk_{cD}] \tag{51}$$

where

k_{ce} = effective pellet thermal conductivity, and

k_{cB}, k_{cD} = thermal conductivity of solid reactant and product, respectively.

Equation (51) assumes that the gas phase thermal conductivity is negligibly small. Woodside and Messmer [55] proposed the following expression for systems that have a significant gas phase thermal conductivity:

$$k_{ce} = k_{cB}\,(\frac{k_{cg}}{k_{cB}})^{\varepsilon} \tag{52}$$

where k_{cg} = thermal conductivity of gas phase.

The gas phase mass transfer coefficient, k_{MA}, and heat transfer coefficient, h, can be estimated using correlations of the general form

$$\frac{2k_{MA}R_P}{D_{AC}} = A + B(Re)^C(Sc)^D \tag{53}$$

$$\frac{2hR_P}{k_{cb}} = A + B(Re)^C(Pr)^D \tag{54}$$

where

k_{MA} = gas phase mass transfer coefficient,

h = gas phase heat transfer coefficient,

k_{cb} = bulk gas thermal conductivity,

Re = Reynolds number = $2R_p u_b/\nu$,

Sc = Schmidt number = ν/D_{AC},

Pr = Prandtl number = $C_{pb}\nu/k_{cb}$,

A, B, C, D = functions of Re, Sc, or Pr,

u_b = average bulk gas stream velocity,

ν = bulk gas kinematic viscosity, and

C_{pb} = bulk gas heat capacity.

Grain size distributions can be determined by using a scanning electron microscope (SEM), image analyzer, or Coulter counter. From the distribution, an average grain radius can be found.

The pellet effective diffusivity can be experimentally determined using several methods [48]. One such method is a modified Wicke-Kallenbach technique in which a cylindrical pellet is placed in a diffusion cell with the pellet's top and bottom exposed to separate streams of gas A. In one of the streams, a pulse of gas B is introduced and the amount that diffuses through the pellet into the other stream of gas A is determined using a thermal conductivity cell. From the data, a value for effective diffusivity can be determined.

Effective diffusivity is usually considered to be a function of the Knudsen diffusivity, D_{KA}, and the molecular diffusivity, D_{AC}. Knudsen diffusion is important for small pores where the gas molecule mean free path is comparable to the diameter of the pore. An expression relating these diffusivities is as follows:

$$D_{Ae} = \frac{1}{\frac{1}{D_{KA}} + \frac{\tau}{D_{AC}\epsilon}} \quad . \tag{55}$$

D_{KA} can be calculated using the following relation [13]:

$$D_{KA} = \frac{4}{3} (8R_o T/\pi M_A)^{1/2} K_o \tag{56}$$

where K_o is a constant (with the dimensions of length) characteristic of the porous solid. The term in parentheses represents the root mean square of the velocity of gaseous A molecules. Several expressions have been suggested for K_o [48]; among them is a result from the "dusty gas model" of Evans et al. [18] for a solid matrix composed of uniform spherical grains:

$$K_o^{-1} = \frac{128}{9} (\frac{n_d \tau}{\epsilon}) r_g^2 (1 + \frac{\pi}{8}) \tag{57}$$

where n_d = number of solid grains per unit volume of porous solid = $3(1 - \epsilon_o)/4\pi r_g^3$.

The binary molecular diffusivity, D_{AC}, can be calculated using the Chapman-Enskog equation:

$$D_{AC} = .0018583 \frac{T^{3/2} (\frac{1}{M_A} + \frac{1}{M_C})^{1/2}}{P\sigma_{AC}\Omega_{AC}} \tag{58}$$

where

M_A, M_C = molecular weight of gaseous species A and C, respectively,

P = pressure,

σ_{AC} = Lennard-Jones 12-6 potential function constant = $1/2(\sigma_A + \sigma_C)$,

σ_A, σ_C = tabulated constants [5], and

Ω_{AC} = collison integral.

III. REVIEW OF LIME SULFATION

The abatement of SO_2 emissions from fossil fuel burning power plants is a major problem in most industrialized nations. In 1970 there was approximately 35 million tons of SO_2 emitted into the atmosphere annually from the United States alone [45]. Recently, a great deal of research and development has been focused on controlling these emissions.

Numerous methods have been proposed for reducing the amount of SO_2 in stack gases and can broadly be classified as "wet" and "dry" processes. The wet methods use a slurry or solution that absorbs the SO_2 (e.g. water, ammonia, alkaline solution). In contrast, the dry methods utilize dry particles of absorbent (e.g. limestone, lime, activated carbon, alkalized alumina) in gas-solid contacting devices such as packed beds, fluidized beds, and entrainment reactors.

A further distinction between processes is whether the absorbent is regenerated or discarded. Regeneration of the absorbent can be accompanied by production of usable sulfur products such as elemental sulfur or sulfuric acid. The relative difficulty in absorbent disposal depends on the inertness of the sulfur-containing compound.

If many regeneration-type facilities are constructed, the output of sulfur products will increase with the possible effect of depressing sulfur prices. This uncertainty in the future market of sulfur products has caused recent attention to focus on "throw away" processes. One such process is the absorption of SO_2 by lime, either by injecting limestone into the system or by using a fluidized bed of lime particles

to carry out the combustion of the coal or oil. Since fluidized beds allow for longer absorbent residence times, they appear to be more promising than absorbent injection.

Because of its low cost and availability, limestone is an attractive agent for SO_2 absorption. In addition, the absorption product, $CaSO_4$, is very inert and easily disposed of. However, one of the problems associated with using limestone is the presence of magnesium carbonate impurities, which can form magnesia and ultimately magnesium sulfate. Since magnesium sulfate is soluble in water, rain water leaching of a wastedump containing this material could cause a water pollution problem. This may require the use of more expensive limestones that contain less magnesium impurities.

At high temperature, limestone calcines to form lime by the following reaction:

$$CaCO_3(s) \rightarrow CaO(s) + CO_2(g) \ . \qquad (59)$$

The CaO product then reacts with SO_2 by the following overall reaction at high temperature:

$$CaO(s) + SO_2(g) + \tfrac{1}{2}O_2(g) \rightarrow CaSO_4(s) \ . \qquad (60)$$

The condition at which the calcination reaction (Equation 59) takes place can greatly affect the internal structure of the CaO product. Ulerich et al. [51] found that calcination in an atmosphere containing CO_2 produced calcines with pores of larger diameters than those of calcines prepared in nitrogen. The overall porosity and surface area

of the calcines prepared in the presence of CO_2 were less than those produced in nitrogen as a result of the shift from finer to wider mouthed pores in the former.

Fischer [20] found that varying the temperature of calcination produced various effects. Below 950°C, the porosity of the calcine product is large and varies little with changing temperature. In the range 950-1200°C, the porosity decreases with increasing temperature due to sintering and above 1200°C, the product porosity increases with increasing temperature. This latter effect is possibly due to immediate sintering and densification of the surface which hinders the evolution of CO_2 from the particle interior, resulting in the formation of a more extensive pore structure.

Hills [26] found that the rate of calcination is controlled by the partial pressure of CO_2 and temperature and that below 800°C, the rate is quite slow, requiring several hours to reach completion. Potter [38] showed that the capacity of uncalcined limestone to react with SO_2 reached an optimum near 900°C, while the capacity of precalcined limestone decreased with increasing temperature above 700°C, possibly showing that the calcination rate is limiting for low reaction temperatures.

The sulfation reaction proceeds rapidly at first, but as the conversion increases, the reaction rate decreases rapidly due to pore closure. Since the solid product molar volume is larger than that of the solid reactant, the pores fill with the expanding product. Unless the solid is initially highly porous, the pores will plug before total

conversion, thus reducing the capacity of the CaO particle to absorb SO_2.

Ulerich et al. [51] found that increasing the mean pore diameter of CaO increases the ultimate conversion. The SO_2 which arrives at the pore mouths can do one of two things. It can react with the grains near the surface of the pellet or it can diffuse into the pores towards the center before reacting. Therefore, reaction and diffusion are seen as competing processes in the distribution of sulfur in the pellet cross-section. Sulfation of CaO containing narrow-mouthed pores results in most of the sulfur product being located at the pore mouths. However, by widening the pore mouths, the SO_2 is able to diffuse further into the pellet before surface pore closure, resulting in a more even sulfur distribution within the pellet.

Calcines produced from limestones of different geological origins have uniquely different internal structures which affect reaction rate and total conversion. However, Borgwardt and Harvey [7] showed that the initial reaction rate per unit surface area of CaO was similar for most of the calcines they tested.

A. Reaction Mechanism

Equation (60) represents the overall sulfation reaction at high temperature; however, several investigators have suggested that the reaction actually occurs in several steps. O'Neill et al. [36] proposed the following mechanism: Adsorption of SO_2 on the CaO surface forms unstable calcium sulfite, $CaSO_3$, which immediately disproportionates to CaS and $CaSO_4$:

$$CaO + SO_2 \rightarrow CaSO_3 \tag{61}$$

$$4CaSO_3 \rightarrow 3CaSO_4 + CaS \ . \tag{62}$$

The following two reactions then compete for the available calcium sulfide, CaS:

$$3CaSO_4 + CaS \rightarrow 4CaO + 4SO_2 \tag{63}$$

$$CaS + 2O_2 \rightarrow CaSO_4 \ . \tag{64}$$

Fieldes et al. [19] studied the effect of SO_3 on the sulfation of lime and proposed two reaction sequences by which sulfation may take place:

$$CaO + SO_2 \rightleftarrows CaSO_3 \tag{65}$$

Route 1

$$CaSO_3 + \tfrac{1}{2}O_2 \rightarrow CaSO_4 \tag{66}$$

$$SO_2 + \tfrac{1}{2}O_2 \rightleftarrows SO_3 \tag{67}$$

Route 2

$$CaO + SO_3 \rightarrow CaSO_4 \ . \tag{68}$$

Their experimental results showed that the overall solid conversion was less for limestone particles exposed to high SO_3 concentrations than those exposed to low concentrations. One explanation for this behavior is that Route 2 (Equations 67 and 68) is faster than Route 1 (Equations 65 and 66) and thus, a high concentration of SO_3 causes rapid reaction at the pore entrances which results in surface pore closure and low overall

conversion. In contrast, Route 1 would predominate for low SO_3 concentrations allowing for diffusion of reactant gas deeper into the pellet and a higher overall conversion.

Infrared studies by Hatfield et al. [25] show that $CaSO_3$ is the major product of sulfation below 640°C, and that the $CaSO_3$ oxidizes to $CaSO_4$ at about 720°C. This would correspond to Route 1 (Equations 65 and 66) proposed by Fieldes et al. [19]. In addition, Hatfield et al. [25] showed that the $CaSO_3$ formed begins to decompose (to form CaO and SO_2) and disproportionate (Equation 62) at around 720°C. The CaS, produced from disproportionation of the $CaSO_3$, was found to oxidize to $CaSO_4$ at temperatures above 880°C. These last two findings correspond to Equations (62) and (64), proposed by O'Neill et al. [36]. Christman and Edgar [14] used x-ray diffraction to confirm the results of Hatfield et al. [25].

B. Reaction Rate Constant

The reported values of the reaction rate constant vary greatly in the literature. Borgwardt and Harvey [7] measured the rate constant at 1250°K and obtained $k = .22 \pm .05$ cm/sec. This value was determined by varying the size of the calcine sample until the SO_2 removal rate became independent of particle size, resulting in a kinetically controlled situation in which the rate constant could be measured directly.

In contrast, Hartman and Coughlin [23] obtained a value of $k = 6.6$ cm/sec at 1123°K, a factor of 30 higher than that found by Borgwardt and Harvey. Their value was derived by using the grain model to fit experimental data in the limit of low fractional conversion ($X = .04$).

Simons and Rawlins [44] suggest that the four parameters (grain radius, gas phase diffusion coefficient, heterogeneous rate constant, and product layer diffusivity) used by Hartman and Coughlin [23] in their grain model were not uniquely determined and thus, the large discrepancy between their reaction rate constant and that of Borgwardt and Harvey [7]. Using a pore model in the limit of low fractional conversion (negligible product layer build-up), Simons and Rawlins [44] obtained a value of $k = .36 \pm .18$ cm/sec at $1250^{\circ}K$. This value was determined by varying the value of k in the model until the predicted results matched the early time conversion data of Borgwardt and Harvey [7].

Bhatia and Perlmutter [4] applied their random pore model to the data of Hartman and Coughlin [23] and showed that the conversion-time curves are not sensitive to the choice of k over the range of values reported by previous investigators. Hartman and Coughlin [23] noted the same behavior with the grain model, indicating that the reaction is strongly controlled by product layer diffusion under the conditions of their study. This insensitivity of the conversion-time curves to k helps to explain how their reported value of k could differ so greatly from that of Borgwardt and Harvey [7].

The influence of temperature on the chemical reaction rate of lime sulfation is important as activation energies between 8 and 18 kcal/gmole have been reported [6, 32, 54]. Borgwardt [6] found that the initial reaction rate of small ($\bar{D}_p$ = .096mm) precalcined particles of limestone increased with increasing temperature between 650° and $950^{\circ}C$.

C. Reaction Order

The rate of reaction between SO_2 and CaO is believed to be first order with respect to SO_2 and zero order with respect to O_2 and CaO [6, 32, 36]. However, Kito and Wen [32] have suggested that the reaction is zero order with respect to SO_2 at low SO_2 concentration.

D. Miscellaneous

The sulfation of lime is highly exothermic with a heat of reaction of -115.3 kcal/mole at 500°C. Table 1 shows heat of reaction values at various temperatures.

Table 1. Heat of reaction for lime sulfation

T (°C)	ΔH_{RXN} (kcal/gmole)
25	-116.4
300	-116.1
400	-115.7
500	-115.3
600	-114.6
700	-113.9
800	-113.0
900	-111.9
1000	-110.7

Reid [42] has shown that the equilibrium partial pressure of SO_2 for this reaction is below 1 ppm at temperatures below 1000°C and therefore, the reaction can be considered irreversible at temperatures below 1000°C. The equilibrium constant at this temperature is 1.7×10^6.

The relative magnitude of pore closure effects in gas-solid reactions can be measured with the expansion coefficient, Z_E:

$$Z_E = \frac{\rho_B{}^d}{\rho_D{}^b} = \frac{\text{Molar volume of solid product}}{\text{Molar volume of solid reactant}} \tag{69}$$

For lime sulfation, the stoichiometric coefficients b and d are both equal to 1 and the molar densities of the reactant and product are:

$$\rho_B = \rho_{CaO} = .0592 \text{ gmole/cm}^3$$

$$\rho_D = \rho_{CaSO_4} = .0192 \text{ gmole/cm}^3 .$$

Substituting these values into Equation (69) gives a value of $Z_E = 3.08$. This is a relatively large value for the expansion coefficient which indicates that the reaction is substantially affected by pore closure due to product layer expansion.

The melting points of CaO and $CaSO_4$ are 2570° and 1450°C, respectively. Since solid materials begin sintering at temperatures as low as 0.4 times the melting point temperature, the $CaSO_4$ product may sinter when the reaction temperature is above 420°C, while the CaO reactant may begin to sinter above 860°C.

E. Lime Sulfation Models

Coutant et al. [16] carried out a series of experiments in which particles of limestone (average diameter of .00895 cm) were injected into a current of hot gas which flowed upward through an insulated tube. The exposure time varied from a fraction of a second to about 3 seconds. Interpretation of the data was attempted using an equation from classical corrosion theory, which stated that the reaction rate should be proportional to the square root of reaction time. This relationship is due to the changes in product layer thickness which the SO_2 has to diffuse through to reach the active reaction surface. In other words, diffusion control was assumed. They found that several sets of data did not follow such a relationship and could not find a systematic relationship between their "rate constants" and gas composition, temperature, or particle size.

Pigford and Sliger [37] extended the reaction model of Coutant et al. [16] by using the grain model of Szekely and Evans [47]. They assumed that the reaction rate is controlled either by the diffusion of SO_2 through the pores or by its diffusion through the developing shells of product on the grains. Their "combined diffusion theory" ignored the effect of chemical reaction rate and thus yielded a comparatively simple solution. They also ignored the change in pellet porosity due to sulfate formation, which meant the model was applicable only at small exposure times.

As a consequence of the assumptions, the following expression was obtained for the internal particle reaction rate:

$$v(r, t) = \left(\frac{D_{As}\rho_B}{2}\right)^{1/2} \frac{C(r, t)}{\left(\int_0^t C(r, p)dp\right)^{1/2}} \tag{70}$$

where

v = reaction rate on internal particle surface,

r = radial particle position,

t = time,

D_{As} = diffusivity of SO_2 through solid product shell,

ρ_B = molar concentration of solid reactant, and

C = local concentration of SO_2.

Equation (70) indicates the reaction rate is not linear with local SO_2 concentration, C. This is contrary to the usual result that the rate of reaction at the grain reaction interface is proportional to the local concentration of the gaseous reactant (assuming the grain follows the unreacted shrinking-core model) as shown in Equation (22).

Wen and Ishida [54] applied a grain model (Model 2) they had developed earlier [29] to the sulfation of lime. The model predictions were compared to the experimental conversion-time data of Borgwardt and Harvey [7] for three particle sizes as shown in Figure 8. There is fairly good agreement except for large time values where the model predicts a high value of conversion for each particle size.

In addition, Wen and Ishida [54] reacted a spherical pellet of CaO having a radius of .55 cm in an airstream containing .39% SO_2 at 760°C. After six hours of reaction, the pellet was cut into halves and a few

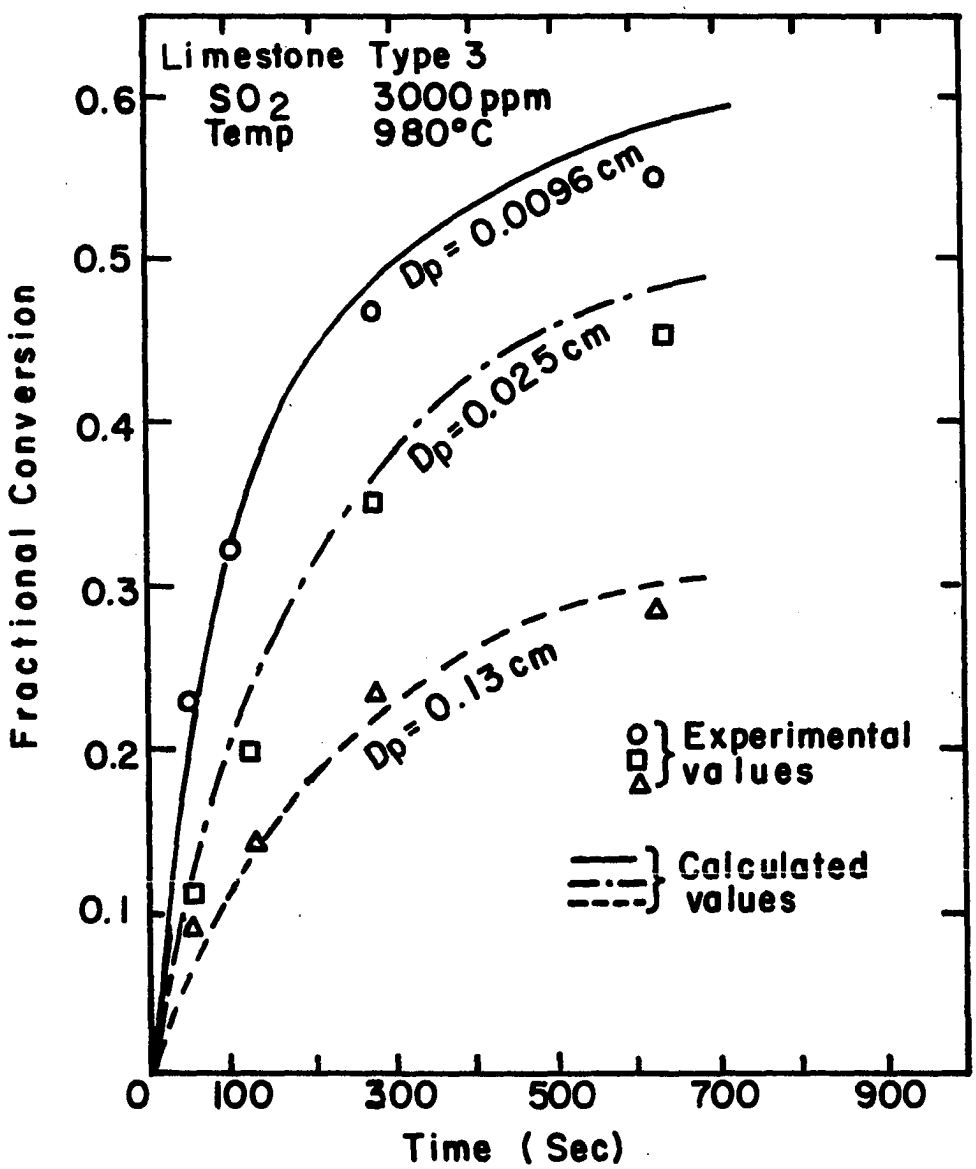

Figure 8. Comparison of predicted and experimental conversions for the sulfation of calcined limestone [54]

drops of phenolphthalein solution were placed on the cut surface which caused the unreacted center to turn pink. Assuming the white outer layer had completely reacted, a conversion of 97.4% was calculated. However, the actual conversion measured from the weight change was only 54.4%. Therefore, the solid in the outer layer was not all $CaSO_4$, but also contained unreacted CaO, possibly in the interior of the grains, thus supporting the use of the grain model for the analysis of this reaction system.

Hartman and Coughlin [22] developed a general relation between the porosity of reacting limestone and its conversion:

$$\epsilon = 1 - (1 - \epsilon_{LS})\rho_{LS} \frac{y}{M_{CC}} [V_{CC} - X_C(V_{CC} - V_{CO}) + X(V_{CS} - V_{CO})]$$

$$- (1 - \epsilon_{LS})(1 - y \frac{\rho_{LS}}{\rho_{CC}}) \qquad (71)$$

where

ϵ = porosity of sulfate loaded particle,

ϵ_{LS} = porosity of natural limestone,

ρ_i = true density of species i,

y = weight fraction $CaCO_3$ in limestone,

M_i = molecular weight of species i,

V_i = molar volume of pure component i,

X = conversion of CaO to sulfate, and

X_C = degree of calcination of $CaCO_3$.

Subscripts:

CC = calcium carbonate,

CO = calcium oxide,

CS = calcium sulfate, and

LS = limestone.

Equation (71) was compared with data from Borgwardt and Harvey [7] and good agreement was observed. The maximum conversion possible can be found by setting $\epsilon = 0$ and solving for X:

$$X_{max} = \frac{1}{V_{CS} - V_{CO}} \left\{ \frac{M_{CC}}{(1 - \epsilon_{LS})\rho_{LS} y} \left[1 - (1 - \epsilon_{LS})\left(1 - y \frac{\rho_{LS}}{\rho_{CC}}\right)\right] \right.$$

$$\left. + X_C(V_{CC} - V_{CO}) - V_{CO} \right\} \quad . \tag{72}$$

From Equation (72) it can be seen that X_{max} can be increased by increasing any of the following parameters: degree of calcination, X_C; weight fraction of $CaCO_3$ in the limestone, y; or porosity of the limestone, ϵ_{LS}. It was found from experiment that particles with a theoretical maximum conversion of over 50% obtained an actual conversion of only 42.5% after an exposure time of eight hours. A possible explanation of this result is that the product shell around each grain becomes so large that the SO_2 can no longer reach the active CaO. Even though the spaces between the grains are large enough to allow the SO_2 to diffuse into the interior of the particle, the reaction essentially stops.

In a later study, Hartman and Coughlin [23] developed a version of the grain model which took into account the rapid decrease in porosity of the reacting particles. The effective diffusivity was written as a

linear function of average pellet porosity:

$$D_{Ae} = D\varepsilon \tag{73}$$

where

D = diffusion coefficient of reactant gas in pores, experimentally determined, and

ε = average pellet porosity (Equation 71).

The radial gradient of D_{Ae} was assumed negligible.

Experimental data were obtained by sulfating a thin layer of uncalcined limestone in a differential reactor. The amount of sulfate in the reacted limestone was determined by titrating with .005 N $Ba(ClO_4)_2$ solution in isopropyl alcohol.

Figure 9 shows a comparison of their experimental data with the revised grain model predictions. The agreement is good for the two larger particles (.90, 1.12 mm), but not as good for the smallest particle (.57 mm) at later exposure times (> 12.5 min). From Figures 8 and 9, it can be seen that the smallest particles reacted faster and obtained a higher final conversion than the larger particles. This shows the effect of the developing product layer near the outside of the particles; the larger particles have less conversion near the center. It should be noted that if the model did not account for changes in D_{Ae} with time (or conversion) it would predict 100% conversion within 10 minutes.

The grain model was further modified by Hartman and Trnka [24] to include the effect of an expanding grain radius on the gaseous reactant

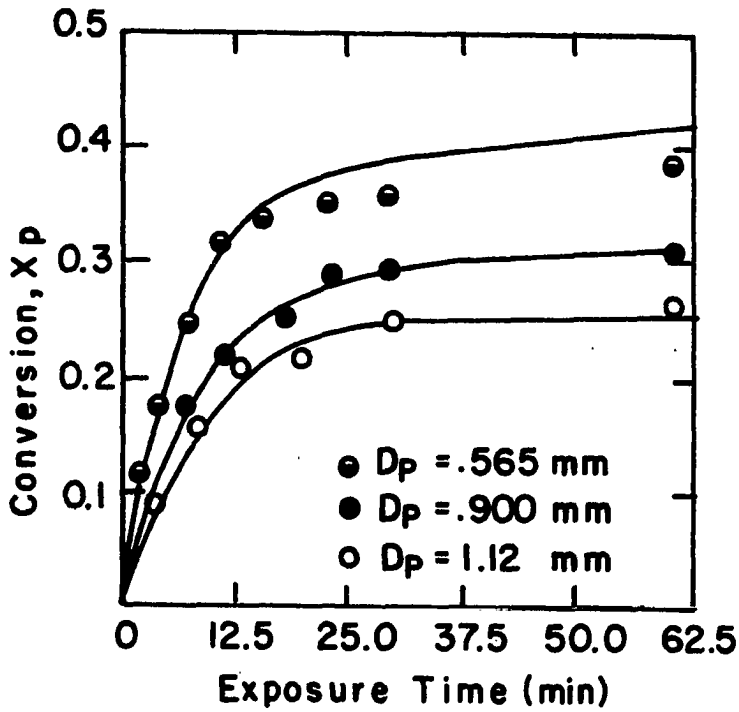

Figure 9. Comparison of predicted and experimental conversion for the sulfation of uncalcined limestone at 850°C [23]

concentration at the reaction interface. Essentially, r_{go} in Equation (8) was replaced by r_g in Equation (25). In addition, they relaxed the assumption that D_{Ae} was not a function of pellet radius. Comparison of their new model with the previous grain model revealed some changes in prediction, but these changes were reportedly nondramatic.

The quantitative effect of calcination temperature on mean grain radius was also studied [24]. The following expression was found to relate the two quantities:

$$\log r_g = -22.70 + 5.99 \log T \qquad (74)$$

where the units of r_g and T are cm and ^{o}K, respectively. Increasing the calcination temperature increased the mean grain radius and thus decreased the amount of surface area per unit volume, which in turn decreased the subsequent sulfation rate. For simultaneous calcination-sulfation, the optimum temperature was found to be in the range 850° - 900°C, which is similar to the findings of Potter [38].

Chrostowski and Georgakis [15] developed a model which treats the solid as a single pore, with a diameter that varies with extent of reaction. Georgakis et al. [21] compared the predictions of this pore plugging model with lime sulfation data from Hartman and Coughlin [23], as shown in Figure 10. The solid curve represents the model predictions when k and D_{As} are evaluated from the experimental data and is seen to overestimate conversion. When k and D_{As} are adjusted to force the model to match the initial rate data, the model underestimates final conversion, as shown in the lower dashed curve.

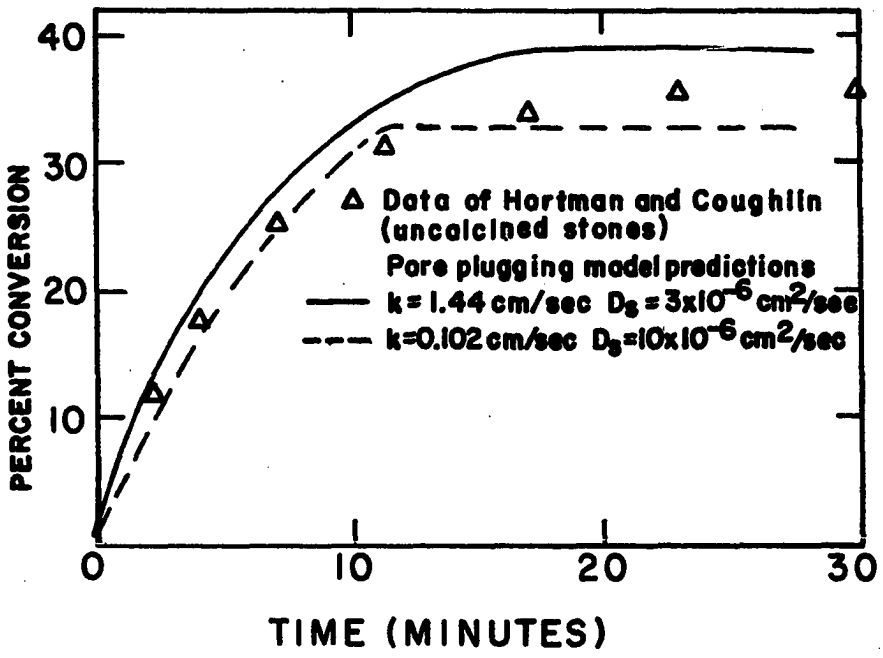

Figure 10. Comparison of predicted and experimental conversion for the sulfation of uncalcined limestone at 850°C [21]

Christman and Edgar [12] incorporated a pore size distribution into the pore model and accounted for solid product build-up. The evolution of the pore size distribution, as a function of time and location, was followed by use of a population balance. By integrating over the pore size distribution, the macroscopic properties necessary to obtain the pseudo-steady state concentration profile in the pellet were obtained. Figure 11 shows the predictions of the model as compared to experimental data taken by Ulerich et al. [51]. During the initial reaction period, the model closely fits the experimental data; however, at later times, the model is seen to overestimate solid conversion.

F. Solid-State Diffusivity

The solid-state diffusion coefficient, D_{As}, of SO_2 through a nonporous layer of $CaSO_4$ is required to appropriately model this gas-solid reaction. A number of values for this parameter have been reported in the literature, as shown in Table 2. All of the values shown were obtained by adjusting D_{As} in a pore or grain model until the model fit the experimental data of interest. In other words, D_{As} was treated as a "best fit" parameter.

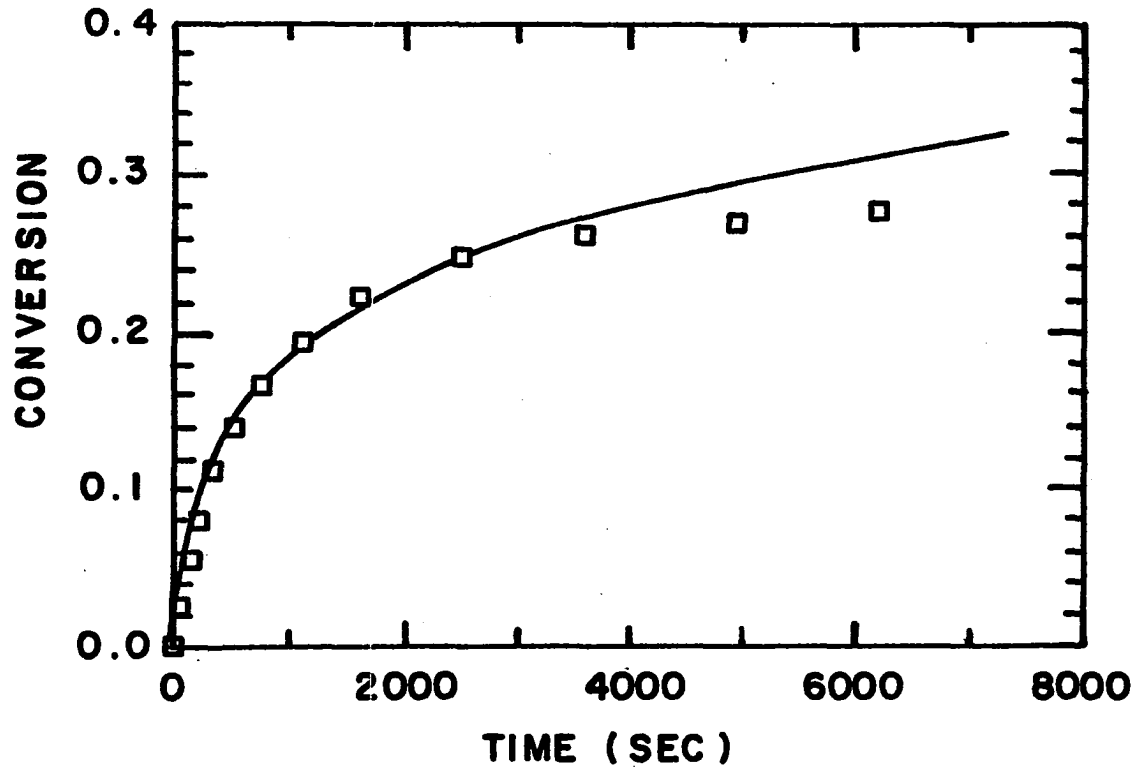

Figure 11. Comparison of predicted and experimental conversion for the sulfation of calcined limestone at 815°C [12]

Table 2. Solid-state diffusivity estimates

Investigator	Source of data	Model	Temp (°C)	Solid-state diffusivity (cm^2/sec)	Activation energy (kcal/mole)
Bhatia and Perlmutter [4]	Borgwardt [6]	Pore	650	1.3×10^{-8}	28.7
			760	6.0×10^{-8}	
			870	19×10^{-8}	
			980	69×10^{-8}	
	Hartman and Coughlin [23]		850	0.86×10^{-8}	
Hartman and Coughlin [23]	Own data	Grain	850	0.6×10^{-8}	
Christman and Edgar [12]	Own data	Pore	650	3.8×10^{-8}	24.2
			800	24×10^{-8}	
Georgakis et al. [21]	Hartman and Coughlin [23]	Pore	850	$(300\text{-}1000) \times 10^{-8}$	
		Grain	850	0.8×10^{-8}	
	Borgwardt [6]	Grain	980	200×10^{-8}	

IV. EXPERIMENTAL

A. Thermogravimetric Equipment

The thermogravimetric equipment used in this study is shown in Figure 12. It consists of a Cahn 1000 electrobalance and a Lindberg model 54341 tube furnace, with a Lindberg Type 2200 solid-state controller capable of controlling the temperature to within $\pm$ 0.5°C. The balance housing was connected to an 18 mm I.D. quartz furnace tube by a 6 mm I.D. Pyrex tube. The solid sample was supported from the balance by a series of 1 mm O.D. quartz rods with hooked ends, and was allowed to hang inside the furnace tube. When the solid was in pellet form, it was suspended from the bottom hook by a small quartz basket.

Nitrogen, oxygen, and sulfur dioxide gases were dried and metered and then fed into the bottom of the reactor where they flowed upward through 46 cm of quartz packing (for preheating the gas), and contacted the reactant solid. Changes in sample weight with time were recorded on an Omniscribe strip chart recorder. Nitrogen gas was purged through the balance chamber and exited the top surge chamber, while the reactant gases exited the bottom surge chamber. A sufficient flow of nitrogen purge was provided to prevent diffusion of SO_2 into the balance chamber.

B. Materials and Materials Preparation

Initially, pellets were made by pressing CaO powder that had been produced by calcining reagent grade $Ca(OH)_2$. This procedure gave rise to pellets with a black deposit on their surface when pressed at 20,000 psig. To avoid this problem, pellets were produced by pressing $Ca(OH)_2$ powder

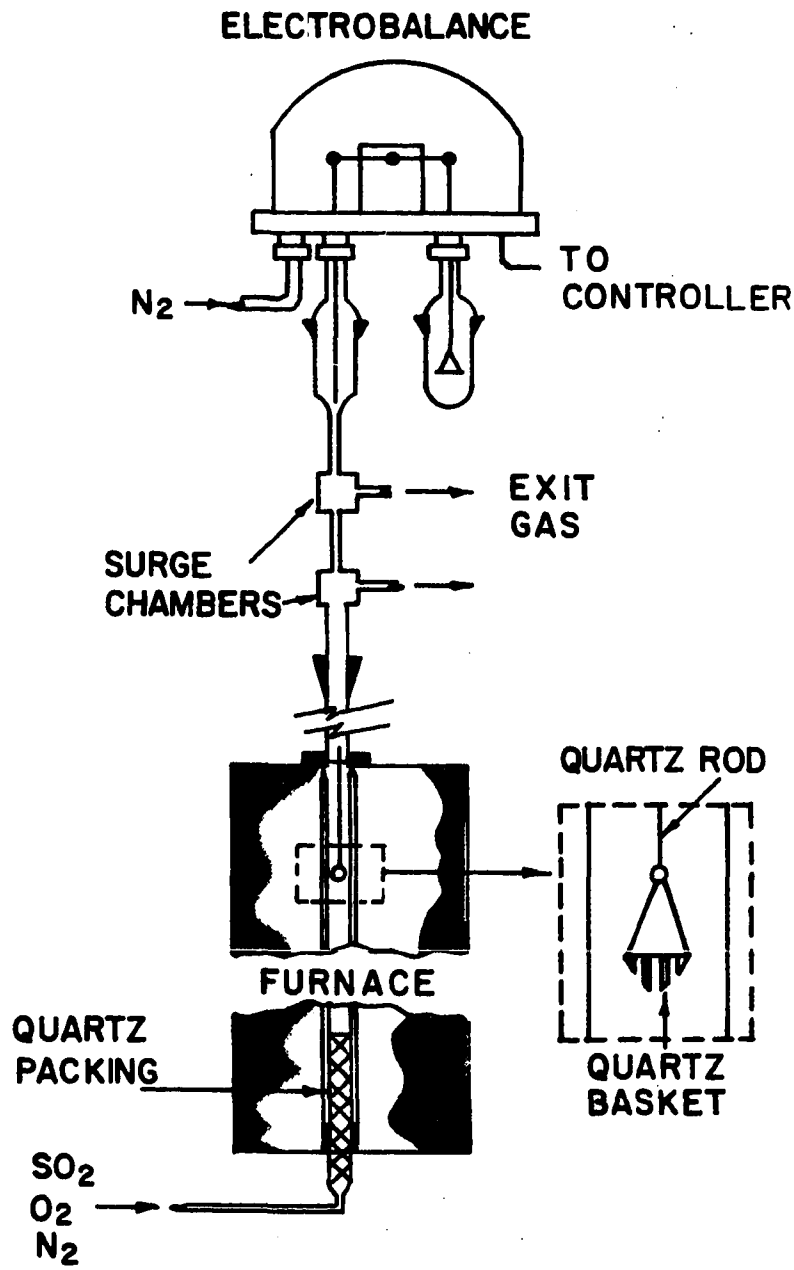

Figure 12. Thermogravimetric analysis equipment for lime sulfation

into pellet form and then calcining the pellets in the TGA system, where they would later be sulfated. No black deposit was found when using this procedure.

The calcination reaction was performed at 570°C in a nitrogen atmosphere and was completed in approximately 15 minutes for cylindrical pellets 0.965 cm in diameter and 0.100 cm in length. After calcination was completed, the pellet was removed from the TGA and the furnace was allowed to heat-up or cool down to the desired sulfation temperature. When the reaction temperature had been obtained, the pellet was replaced in the system and allowed to thermally equilibrate for 5 minutes, after which the reaction was initiated. It was important to keep the CaO pellets in a water-free atmosphere because of their high reactivity with with water to form $Ca(OH)_2$. For this reason, the pellets were sealed inside a small test tube during the furnace heat up (or cool down) period.

The overall dimensions of the $Ca(OH)_2$ pellets decreased during the calcination reaction. For a pellet originally 0.965 cm in diameter and 0.100 cm in length, the calcined pellet dimensions reduced to 0.920 cm and 0.090 cm, respectively. However, the sulfated pellet dimensions did not change appreciably from that of the calcined pellet, up to temperatures of 750°C. At reaction temperatures above 750°C, the dimensions decreased with increasing temperature, probably due to sintering of the solid product and possibly solid reactant.

An attempt was made to obtain a chemically controlled regime using the thin pellets (0.920 cm diameter, 0.090 cm length) described previously. However, initial rate data showed the reaction was controlled

by internal diffusion resistances during the early reaction period and therefore, the reaction rate constant could not be obtained directly from the data. Pellets pressed at very low pressures, to produce high initial porosities, and pellets made from a mixture of inert and CaO were also found internally diffusion limited during their initial reaction period.

A chemically controlled regime was obtained by depositing a thin layer of $Ca(OH)_2$ onto a plate of quartz glass by dipping the plate (14 mm x 51 mm x 1 mm) into a slurry mixture of $Ca(OH)_2$ and water, and then allowing the material on the plate to dry at atmospheric conditions. The plate was then suspended in the TGA system and the attached $Ca(OH)_2$ was calcined at 570°C and then sulfated to obtain initial rate data. Each plate contained a 3 mm diameter hole near one edge from which it could be vertically suspended from the bottom quartz hook. The plates contained approximately 0.01 g of $Ca(OH)_2$ and no detectable amount of solid flaked off during either the calcination or sulfation reactions. Therefore, this proved to be a good method for supporting the solid.

At high temperatures (740°C and above), the chemical reaction rates of the material on the quartz plates were so fast that external mass transfer became limiting. Even a superficial gas velocity of 170 cm/sec was insufficient to eliminate this resistance. This was the highest attainable velocity due to equipment limitations, namely, the sample would begin to erratically swing and strike the sides of the reactor tube. In order to reduce the chemical reaction rate at these temperatures, the specific surface area of the samples was reduced by sintering at 1000°C

for 30 minutes, prior to reaction. This reduced the initial surface areas by a factor of 20 which made chemical reaction control attainable, and made possible the direct determination of reaction rate constants at the higher temperatures.

The reactions in all cases were initiated by turning a valve which introduced the metered SO_2 flow into the reactant gas line. When high gas velocities were used in conjunction with high concentrations of SO_2, the buoyancy effect of the SO_2 gas contacting the sample, and the sample support, was quite significant. As soon as the SO_2 valve was turned, the apparent weight of the sample would drop since the gas was flowing upward. Figure 13a shows a typical weight versus time response for a CaO sample reacting in a relatively fast stream of gas (100 cm/sec), with a SO_2 molar concentration greater than one percent. As can be seen, the apparent weight of the sample drops rapidly, levels off, and then begins to rise. In order to obtain the actual weight versus time data, a blank run needs to be performed. Figure 13b shows the weight versus time data for SO_2 contacting the sample support (basket or plate), at the same conditions as Figure 13a, but with no CaO present. To obtain the actual weight versus time data, one needs to superimpose the blank curve onto the original curve (Figure 13c) and calculate the difference at any given time. These differences represent the actual weight versus time data for that particular experiment (Figure 13d).

A procedure was designed to quantitatively measure the product distribution using the TGA apparatus. A quartz plate containing CaO was reacted to a given conversion level, at which point the SO_2 and O_2 flows

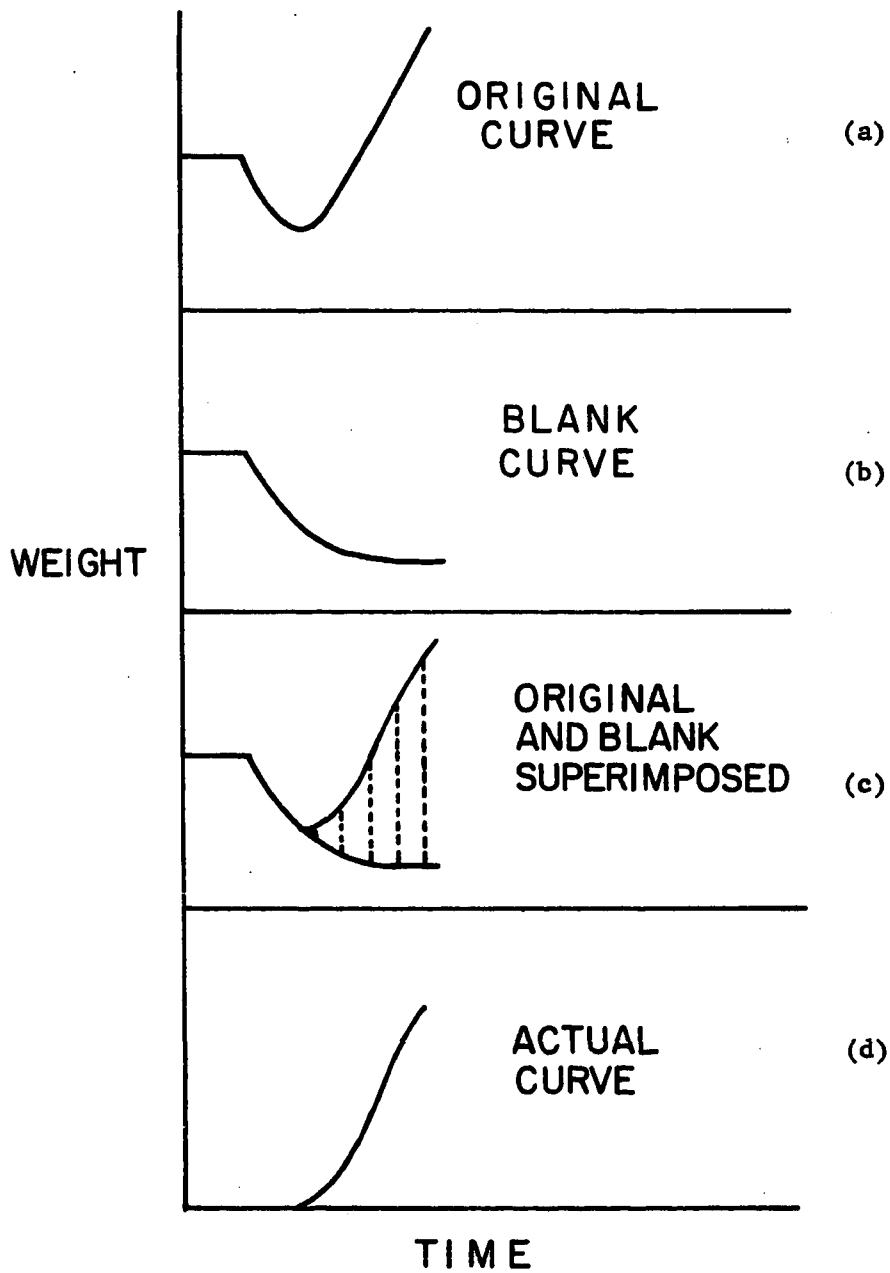

Figure 13. Buoyancy correction for experimental weight vs time curve

were shut off. The reactor temperature was then increased to note any effect on the product. If $CaSO_3$ was present in the product, a weight loss was observed due to its decomposition into CaO and SO_2. From this weight loss, and the original weight gain, the fraction of $CaSO_3$ in the original product could be determined, assuming none of the $CaSO_3$ disproportionated into $CaSO_4$ and CaS during the decomposition period. This period required between 1 and 4 minutes.

In the case of sulfation without oxygen present, the sample lost weight immediately after the SO_2 flow was shut off, and no temperature increase was needed for $CaSO_3$ decomposition. The decomposition period required only 3 seconds in this case. In each case, the decomposition was performed in a nitrogen atmosphere.

Surface area measurements were made using a Micromeritics Accusorb surface analyzer. Pore size distributions and the effects of sintering and sulfation on the distributions were studied using a Quantachrome mercury porosimeter. Scanning electron micrographs were taken of the reacted and unreacted solids.

V. EXPERIMENTAL RESULTS

A. Reaction Order

In order to establish the reaction order of lime sulfation, it was first necessary to experimentally obtain a chemically controlled regime. This was first attempted by using pellets of CaO, produced by pressing $Ca(OH)_2$ powder at 20,000 psig in a cylindrical die. The $Ca(OH)_2$ pellets were calcined at 570°C to form CaO, and then reacted over a range of temperature (450° to 930°C). The CaO pellets had an initial porosity of 0.59 and were all 0.920 cm in diameter and 0.090 cm in length. The gas composition used for reaction was 2% SO_2, 20% O_2 and the balance N_2 (where % indicates mole percent). Initial rates were calculated from the initial, linear portion of the TGA weight versus time curve, which existed up to about 4% conversion. From the data, an activation energy was computed by plotting the natural logarithm of initial rate versus the inverse reaction temperature. A value of 1.4 kcal/mole was computed.

The small magnitude of the activation energy indicated either external mass transfer or internal diffusion was controlling the reaction during the initial rate period. It was shown that the gas velocities used (80-120 cm/sec) were sufficiently large to exclude external mass transfer resistance. This was done by simply increasing the velocity and observing no significant increase in the initial rates. Therefore, the low activation energy could be attributed to internal pore diffusion limitations, which are apparently important even at early reaction time.

Another set of pellets was produced by pressing $Ca(OH)_2$ powder at 2000 psig rather than 20,000 psig. These pellets had an initial porosity

of 0.68, as compared to 0.59 for those compressed at 20,000 psig. From the initial reaction rates of these pellets, an activation energy of 3.0 kcal/mole was determined. Although this value was larger than the previous value, it was still too small for chemical control and indicated internal diffusion was still controlling the reaction. An increase in activation energy with an increase in initial porosity is what was expected. As porosity increases, the reaction is less controlled by internal diffusion and more controlled by the chemical reaction, giving rise to a higher activation energy.

Pellets made from a mixture of CaO and inert powder were reacted to try to achieve chemical control. Groups of pellets containing 20 wt %, 10 wt %, and 1 wt % CaO were reacted and were all found to be internally diffusion controlled.

A chemically controlled regime was finally obtained by depositing a thin layer of $Ca(OH)_2$ onto a plate of quartz glass, calcining the $Ca(OH)_2$ to form CaO, and then sulfating the CaO. The layer of $Ca(OH)_2$ was deposited by dipping the plate into a slurry mixture of $Ca(OH)_2$ and water and allowing the plate to dry at atmospheric conditions. Figure 14 shows a logarithmic plot of initial rate versus SO_2 concentration for reaction data taken at 560° and 640°C. In each case, the curve is linear up to an SO_2 concentration of around 3×10^{-7} mole/cm^3 (2 mole %), at which point the curve becomes horizontal. An explanation for this behavior is that the overall reaction is controlled by external mass transfer for low SO_2 concentrations and at higher concentrations, the reaction is controlled by the chemical reaction rate, which appears to be zero order at these temperatures. External

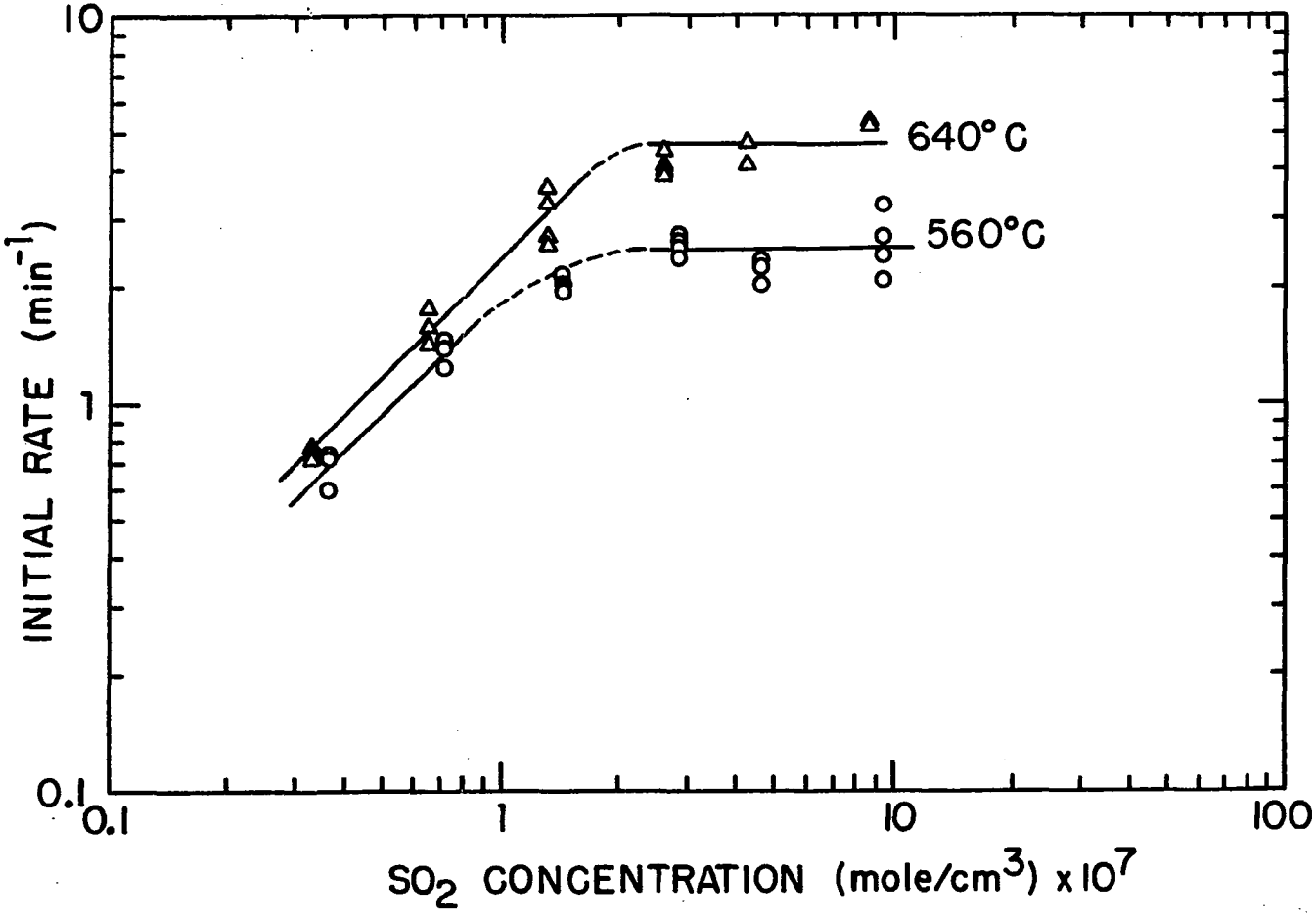

Figure 14. Initial rate vs SO_2 concentration for CaO on quartz plates

mass transfer resistance at the lower SO_2 concentrations was substantiated by increasing the gas velocity at these concentrations and observing an increase in the initial rates, up to an asymptotic value corresponding to the rate at high SO_2 concentration.

Another way of showing that the reaction rates, at low SO_2 concentration, are externally mass transfer limited is by comparing the relative differences between the two curves, in Figure 14, at any given SO_2 concentration. At low concentrations, the difference in height between the curves is quite small. At high concentrations, the difference is relatively large. These differences correspond directly to activation energies and therefore, the activation energy at low concentrations is smaller than that at high concentrations. Since the activation energy for diffusion is usually smaller than that for chemical reaction, the initial rates at low SO_2 concentration must be diffusion controlled.

The reaction was shown to be zero order at temperatures below 560°C as well. Initial rates measured at 470°C showed similar behavior to that shown in Figure 14 for 560° and 640°C.

At temperatures above 640°C, it was determined that the initial reaction rate was controlled by external mass transfer throughout the entire range of SO_2 concentrations studied (0.25 - 8.0 mole %). Even a superficial gas velocity of 170 cm/sec was insufficient to exclude this resistance, and that was the highest velocity attainable. Therefore, it was necessary to reduce the specific surface area of the solid, and thus, the specific chemical reaction rate, in order to obtain chemical reaction control. This was done by sintering the CaO, on the quartz

plate, in an oven at 1000°C for 30 minutes. The sintered material was then placed in the TGA system and reacted with SO_2.

Figure 15 shows the initial rate data for the sintered CaO, reacted at 742°, 836°, and 929°C. A linear least squares fit of the data gives an average slope of 1.0, which indicates the reaction is first order in this temperature range. In order to verify that external mass transfer resistance was negligible, a run was performed at 929°C using 1% SO_2 and a superficial gas velocity over 3 times higher than that used for these data (50 cm/sec). The initial rate increased by only 9%, which is small compared to the increase expected if external mass transfer was controlling the reaction.

First order kinetics (in SO_2) at high temperature is in agreement with the findings of other workers [6, 32]. However, little work has been done on lime sulfation at temperatures below 560°C, and no reaction order data were found to compare with the zero order kinetics found in this study.

The reaction was shown to be zero order in oxygen at all conditions studied, which supports the results of other researchers [6, 32].

B. Lime Sulfation Product Distribution

The shift from zero to first order kinetics, as temperature is increased, was expected to be the effect of different reactions at different temperatures. This was verified by determining the product distribution with temperature, as outlined in the Experimental section. Essentially, the amount of $CaSO_3$ present in a sample on a quartz plate was determined by decomposing the $CaSO_3$ to form CaO and SO_2. From the

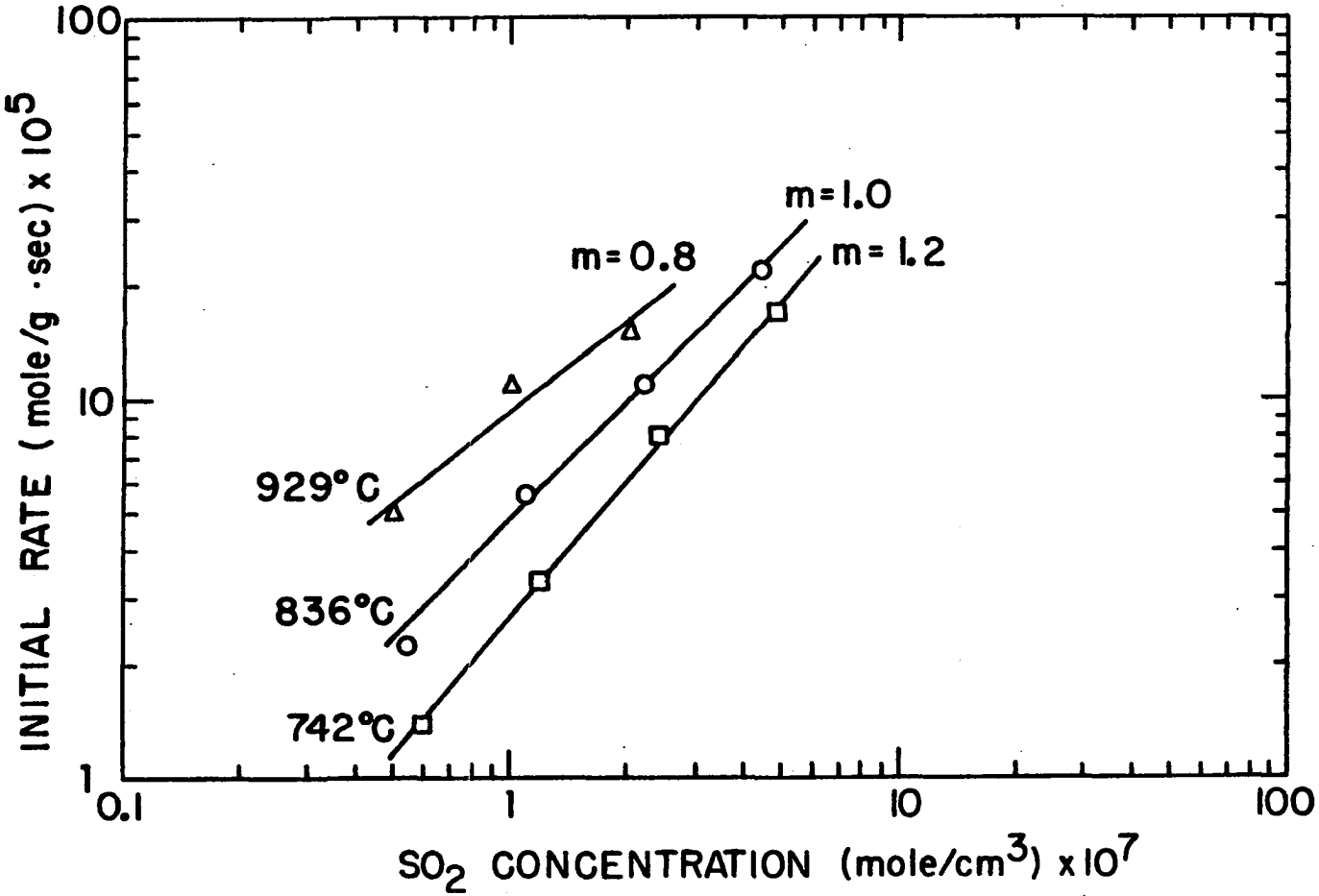

Figure 15. Initial rate vs SO_2 concentration for CaO on quartz plates, sintered at 1000°C for 30 min.

weight loss incurred in the decomposition and the weight gain from the sulfation reaction, the amount of $CaSO_3$ in the sample could be determined.

Table 3 lists the results for the determination of the product distribution. The column heading, X, refers to overall CaO conversion. It can be seen from Table 3 that the composition of the solid product depends on temperature, reactant gas composition, and reaction time. At 450°C, the product after one minute of reaction is all $CaSO_3$ and is probably formed by the reaction:

$$CaO + SO_2 \rightarrow CaSO_3 \ . \qquad (61)$$

In the presence of oxygen, as the temperature is increased above 450°C, the product becomes a mixture of $CaSO_3$ and $CaSO_4$ up to a temperature around 740°C, at which point it is all $CaSO_4$. $CaSO_4$ is produced from the overall reaction:

$$CaO + SO_2 + 1/2\ O_2 \rightarrow CaSO_4 \ . \qquad (60)$$

In the absence of oxygen, above 560°C, the product becomes a mixture of $CaSO_3$, $CaSO_4$, and CaS up to a temperature of 830°C, at which point it contains only $CaSO_4$ and CaS. With no oxygen present, $CaSO_4$ and CaS are formed by one or both of the following reactions:

$$4\ CaSO_3 \rightarrow 3\ CaSO_4 + CaS \qquad (62)$$

$$4\ CaO + 4\ SO_2 \rightarrow 3\ CaSO_4 + CaS \ . \qquad (75)$$

At any given temperature, the weight fraction of $CaSO_3$ in the product tends to decrease with reaction time, probably due to disproportionation

Table 3. Lime sulfation product distribution

T (°C)	2% SO_2 20% O_2 78% N_2				2% SO_2 98% N_2			
	1 min		20 min		1 min		20 min	
	X	wt% $CaSO_3$	X	wt% $CaSO_3$	X	wt% $CaSO_3$	X	wt% $CaSO_3$
450	.23	100	.30	70				
560	.31	78	.41	35	.34	100		
640	.43	20	.53	0	.48	89	.58	53
735	.53	0			.56	67		
830	.49	0			.34	0		

(Reaction 62). This could also be caused by oxidation of $CaSO_3$ to $CaSO_4$ if oxygen was present in the reactant gas:

$$CaSO_3 + 1/2\ O_2 \rightarrow CaSO_4 \ . \qquad (66)$$

Therefore, as the reaction proceeds, more and more of the $CaSO_3$ that has been produced will tend to disproportionate and/or oxidize, causing the $CaSO_3$ weight fraction to decrease.

The data in Table 3 show that conversion after one minute, with or without oxygen, increases with temperature up to around 735°C, and then decreases with increasing temperature. This can be attributed either to sintering of the reactant solid prior to reaction or sintering of the product layer during reaction, or both. Sintering results in a reduction of the surface area available for reaction and thus, reduces the reaction rate and ultimate conversion.

In the presence of oxygen, any CaS that is formed will oxidize to $CaSO_4$ at high temperature, as shown by Christman and Edgar [14]. However, without oxygen present the CaS should remain unchanged. An attempt was made to measure the amount of CaS in a sample reacted at 830°C in 2% SO_2 and 98% N_2. After 20 minutes of reaction, the SO_2 flow was shut off and the furnace was allowed to heat up to 930°C, at which point an oxygen flow was admitted into the reactor. A weight increase due to the oxidation of CaS to $CaSO_4$ was expected, but only a negligible increase was seen. However, since CaS can only be formed by Reaction 62 or 75, the weight fraction of CaS could never be more than 0.15, due to stoichiometric considerations.

After one minute of reaction, the weight fraction of $CaSO_3$ is higher when reaction is carried out without oxygen. This shows the importance of Reactions 60 and 66 which occur only in the presence of oxygen. The conversion levels are also higher when no oxygen is present, which was also shown by Christman and Edgar [14].

From Table 3, it can be concluded that the transition in reaction order, with respect to SO_2 concentration, corresponds to the transition in solid product composition. At low temperatures, where the primary product is $CaSO_3$, the reaction is zero order and at higher temperatures, where $CaSO_4$ is the major product, the reaction is first order.

Since the values of weight percent $CaSO_3$ in Table 3 are based on the assumption that disproportionation did not occur during the decomposition period, the accuracy of the values would be impaired (the reported values would be too low) if some disproportionation did indeed occur. The values that would be most impaired are those at 450° and 560°C, in the presence of oxygen, since the decomposition period was of considerable duration (4 min). Because of the possibility of disproportionation during decomposition, the values in Table 3 should not be taken as exact estimates, but they do serve to demonstrate the general effects of the reaction conditions on the product distribution.

C. Reaction Rate Constant

In order to obtain estimates of the reaction rate constants for lime sulfation, it was necessary to combine the initial rate data with information on the initial surface area of the reacting solid. Surface areas were measured using a Micromeritics Accusorb surface analyzer.

Nitrogen was used as the adsorbate gas for these measurements. A detailed explanation of the experimental procedure for measuring surface areas by this method can be found elsewhere [27].

Table 4 shows the values obtained using this method on $Ca(OH)_2$ and CaO samples prepared in different manners. Each value listed is the average value from three separate experiments. The first preparation method consisted of placing reagent grade $Ca(OH)_2$ powder directly into the BET flask. The second method was coating the surface of a large sheet of glass with a slurry of $Ca(OH)_2$ and water, allowing the deposit to dry, and then scraping it off with a razor blade and placing it inside a BET flask. For the third method, $Ca(OH)_2$ was pressed into pellet form and placed in a BET flask. In each case, the CaO samples were prepared by placing the appropriate $Ca(OH)_2$ sample in an oven at 570°C for 30 minutes. This allowed enough time for total conversion of the $Ca(OH)_2$ to CaO. A fourth method attempted was to deposit $Ca(OH)_2$ on the inside

Table 4. Surface area measurements

Material	Reagent grade powder (m^2/g)	Deposited on glass, then scraped off (m^2/g)	Pressed into pellet form (m^2/g)
$Ca(OH)_2$	16.3 ± 0.3	15.3 ± 0.3	15.0 ± 0.1
CaO	16.4 ± 0.3	13.5 ± 0.1	33.0 ± 0.3

walls of a BET flask, using a $Ca(OH)_2$ slurry. However, this did not provide enough sample to accurately measure the surface area. This method would have provided the best estimate for the initial surface area of CaO deposited on a plate, but since it failed, the second method was chosen as the most representative.

As seen from Table 4, the specific surface areas measured for $Ca(OH)_2$ did not vary greatly among the different methods. On the other hand, the CaO samples did show some variation among methods of preparation. The largest difference occurred between CaO in pellet form (33.0 m^2/g) and CaO produced from the $Ca(OH)_2$ precipitate (13.5 m^2/g). One possible explanation for this discrepancy is that even though the $Ca(OH)_2$ grains in the pellet tend to shrink during calcination, the grains produced from the precipitation process may tend to shrink more since there is less binding force among the grains. The result would be a less extensive micropore structure within the grains of the precipitate and thus, a lower surface area.

The initial surface area of deposited CaO, sintered at 1000°C for 30 minutes, was first estimated by sintering $Ca(OH)_2$, that had been scraped from a large sheet of glass, in an oven at 1000°C for 30 minutes and then measuring the surface area of the resultant powder. This procedure provided enough sample to do a meaningful surface area measurement and gave an average value of 4.3 m^2/g. When this value is compared to the value of the initial surface area of unsintered CaO on a plate (13.5 m^2/g), it would be expected that the initial rates of the sintered CaO samples would be about one-third those of the unsintered

samples, assuming chemical reaction control. However, the measured initial rates of the sintered samples were actually one-twentieth those of the unsintered samples when reacted at 570° and 650°C. A possible explanation for this is that during transfer of the sample from the oven to the BET flask, it may have reacted with H_2O in the air, causing swelling and cracking of the grains which may have induced a higher surface area. CaO is very hygroscopic, which presents difficulties when transferring samples from one location to another. Another explanation is that the powder attached to a quartz plate sinters at a higher rate than loose powder in a ceramic boat.

The initial surface area of the presintered CaO was then estimated by comparing the initial rates of sintered and unsintered samples when reacted at 570° and 650°C, where the initial reaction rates of unsintered samples were known to be under chemical reaction control. Since the initial surface area of an unsintered sample was known, the surface area of the sintered samples could be obtained by multiplying the ratio of the sintered rate to the unsintered rate by 13.5 m^2/g. Doing this for five samples gave an average value of 0.64 m^2/g for the surface area of sintered CaO on a quartz plate. Another estimate of this surface area was made by depositing $Ca(OH)_2$ on small (0.5 cm) fragments of quartz glass and then sintering the material for 30 minutes at 1000°C. The fragments were then transferred to a BET flask and the surface area of the material was determined using krypton as the adsorbate gas. By this method, the specific surface area of the sintered CaO was found to be 0.58 m^2/g, which is in good agreement with the value determined using

initial rate comparisons.

The first and zero order reaction rate constants were calculated using the initial rate data and the initial specific surface areas. Arrhenius plots were then constructed to determine the activation energies of the two reactions. Figure 16 shows a plot of reaction rate constant versus the inverse reaction temperature for the first order formation of $CaSO_4$. The reaction rate constants used in Figure 16 were computed from the initial rate data in Figure 15 at 0.5 and 1.0 mole % SO_2. The curve drawn in Figure 16 represents the linear least squares fit of the data and has a slope of $9600^{\circ}K^{-1}$, which corresponds to an activation energy of 19.1 kcal/mole. This compares fairly well with the range of values reported by Borgwardt [6] for calcines of different limestones. He reported values between 8.1 and 18.1 kcal/mole, calculated from initial rate data between 650° and 980°C. Wen and Ishida [54] reported an average value of 17.5 kcal/mole, found by applying the grain model to other researchers' data. They also reported that sulfation of pure CaO resulted in a slightly higher value. Hatfield et al. [25] found a range of 15.6-17.8 kcal/mole.

To determine the activation energy corresponding to the zero order formation of $CaSO_3$, initial rate data were obtained between 350° and 452°C where it is known the product is all $CaSO_3$ (at least during the initial reaction period). Table 5 lists the initial rates determined at these temperatures where the gas composition was 2% SO_2, 20% O_2, and the balance N_2. From the data, reaction rate constants were calculated and plotted against the inverse reaction temperature, as shown in

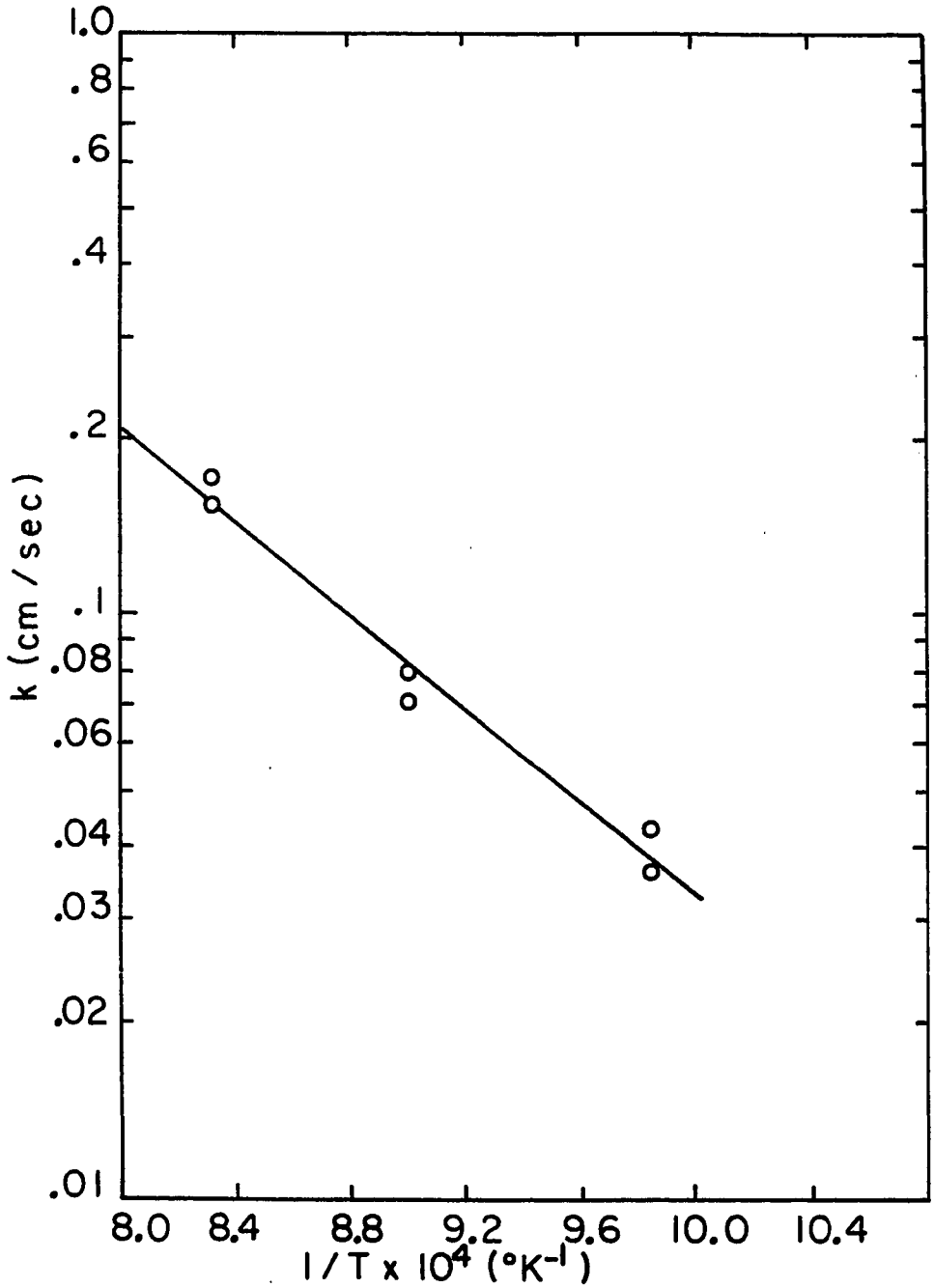

Figure 16. Arrhenius plot of reaction rate constant vs inverse temperature for the sulfation of CaO at high temperature

Table 5. Initial reaction rates at low temperatures

T (°C)	Initial rate (min^{-1})
350	.19
394	.52
452	1.14

Figure 17. An activation energy value of 15.4 kcal/mole was calculated from the slope of the curve in Figure 17. Christman and Edgar [14] determined an activation energy of 12.1 kcal/mole for temperatures between 200° and 400°C and attributed this to the formation of $CaSO_3$. However, they also noted that pore diffusion resistance may have been limiting their initial reaction rates, and thus, their value of 12.1 kcal/mole may be too low.

The reaction rate constants were written in the following form:

$$k = k_o \exp\left(-\frac{E_{ACT}}{R_o T}\right) \tag{76}$$

where k_o is the frequency factor and E_{ACT} is the activation energy. Using the data obtained at high temperature, the following expression was determined for the reaction rate constant for $CaSO_4$ formation:

$$k = 445 \exp\left(-\frac{19100}{R_o T}\right) \tag{77}$$

where the units of k are cm/sec, R_o is equal to 1.987 cal/mole °K, and

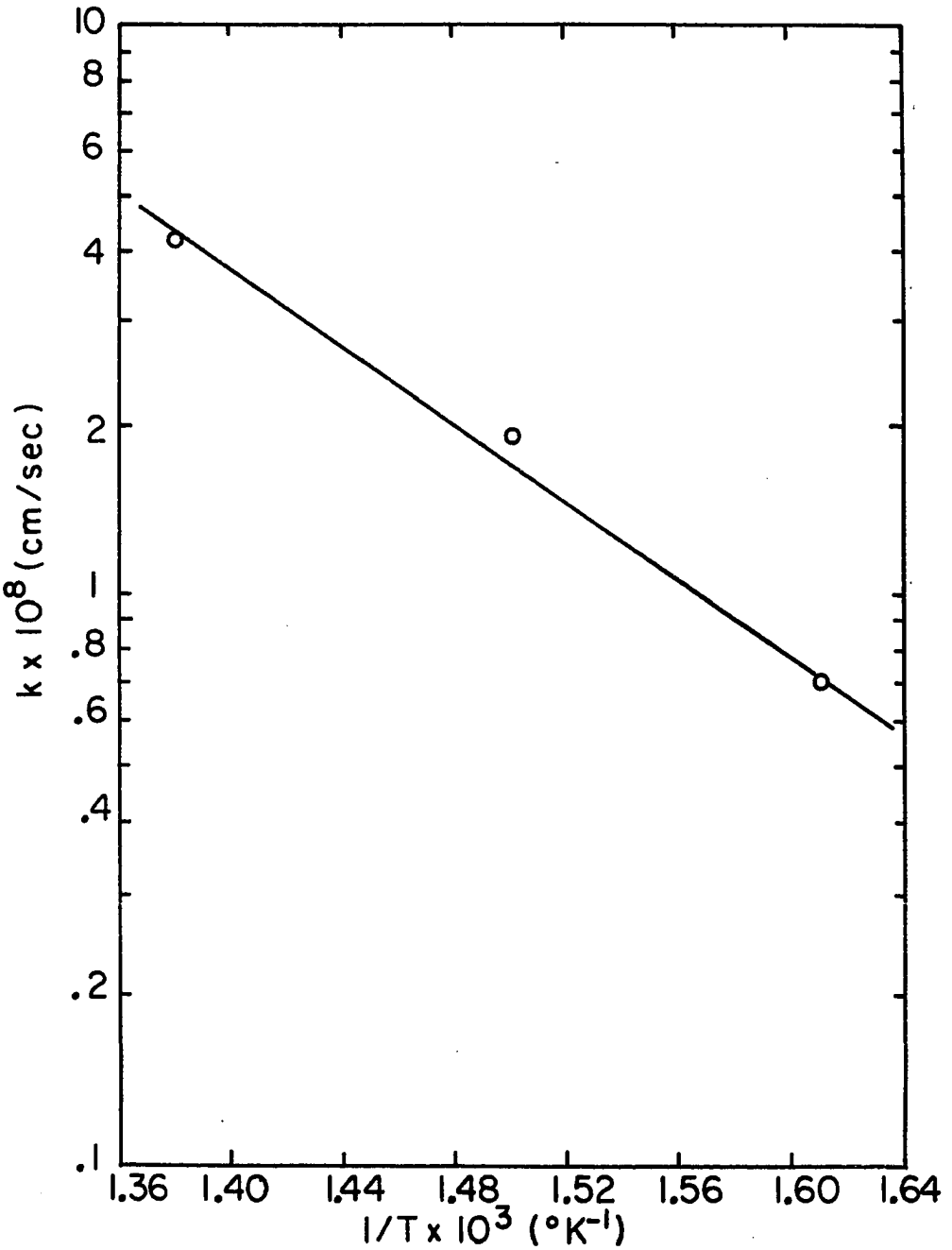

Figure 17. Arrhenius plot of reaction rate constant vs inverse temperature for the sulfation of CaO at low temperature

T is expressed in ^{o}K. Using Equation (77), the first order reaction rate constant at 980°C can be found to be 0.21 cm/sec. This value compares very well with the value of 0.22 cm/sec reported by Borgwardt [6] for the sulfation of calcined limestone at 980°C.

Similarly, the reaction rate constant for the zero order formation of $CaSO_3$ can be expressed as

$$k = 1.84 \times 10^{-3} \exp\left(-\frac{15400}{R_o T}\right) \qquad (78)$$

where all of the units are the same as in Equation (77). No literature values were found to compare with the estimates from Equation (78).

D. Pore Size Distribution Measurements

To gain a further understanding of the solid structure of the $Ca(OH)_2$ and CaO powders deposited on the quartz plates, the pore size distributions of the materials were examined using a Quantachrome mercury porosimeter. Figure 18 shows a plot of cumulative pore volume versus mercury intrusion pressure for five different solids. Curve 1 is for CaO powder produced by calcining deposited $Ca(OH)_2$ (denoted by the downward arrows in Figures 18 and 19). The $Ca(OH)_2$ deposit was scraped from a glass plate prior to calcination. Curve 2 is for solid 1 that has been sintered for one hour at 1000°C. Curve 3 represents reagent grade $Ca(OH)_2$ powder, while Curve 4 is for deposited $Ca(OH)_2$. Curve 5 represents the solid of Curve 1 that has been sulfated at 740°C to 50% conversion.

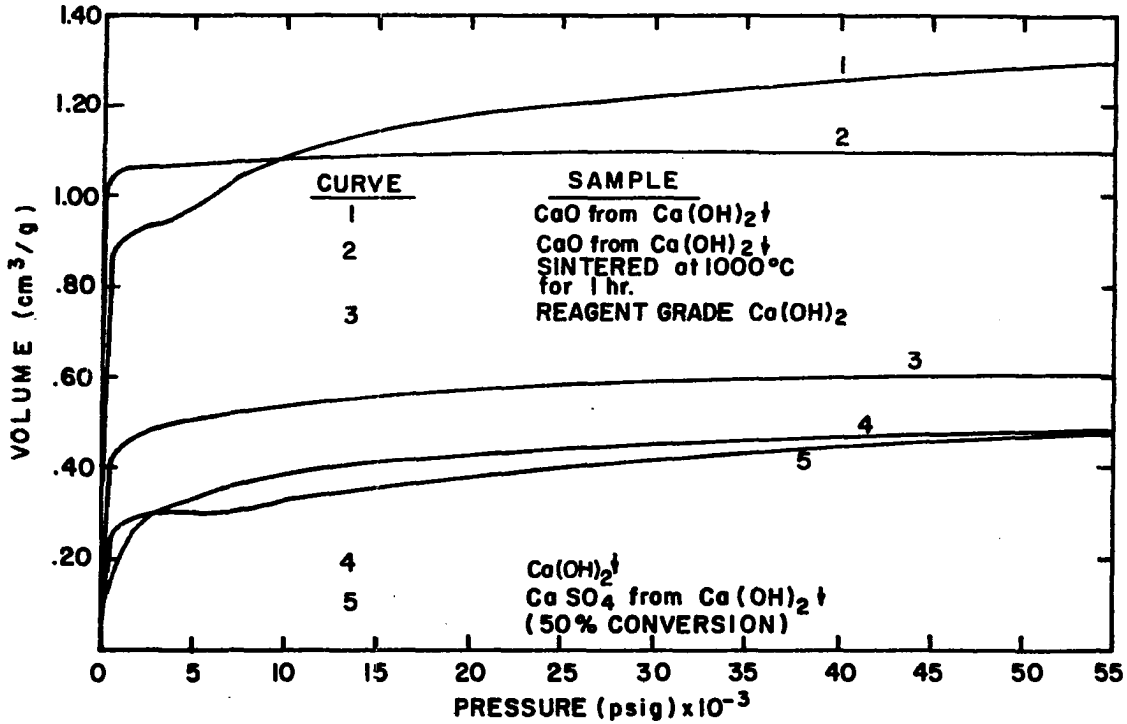

Figure 18. Cumulative pore volume vs pressure for various solids

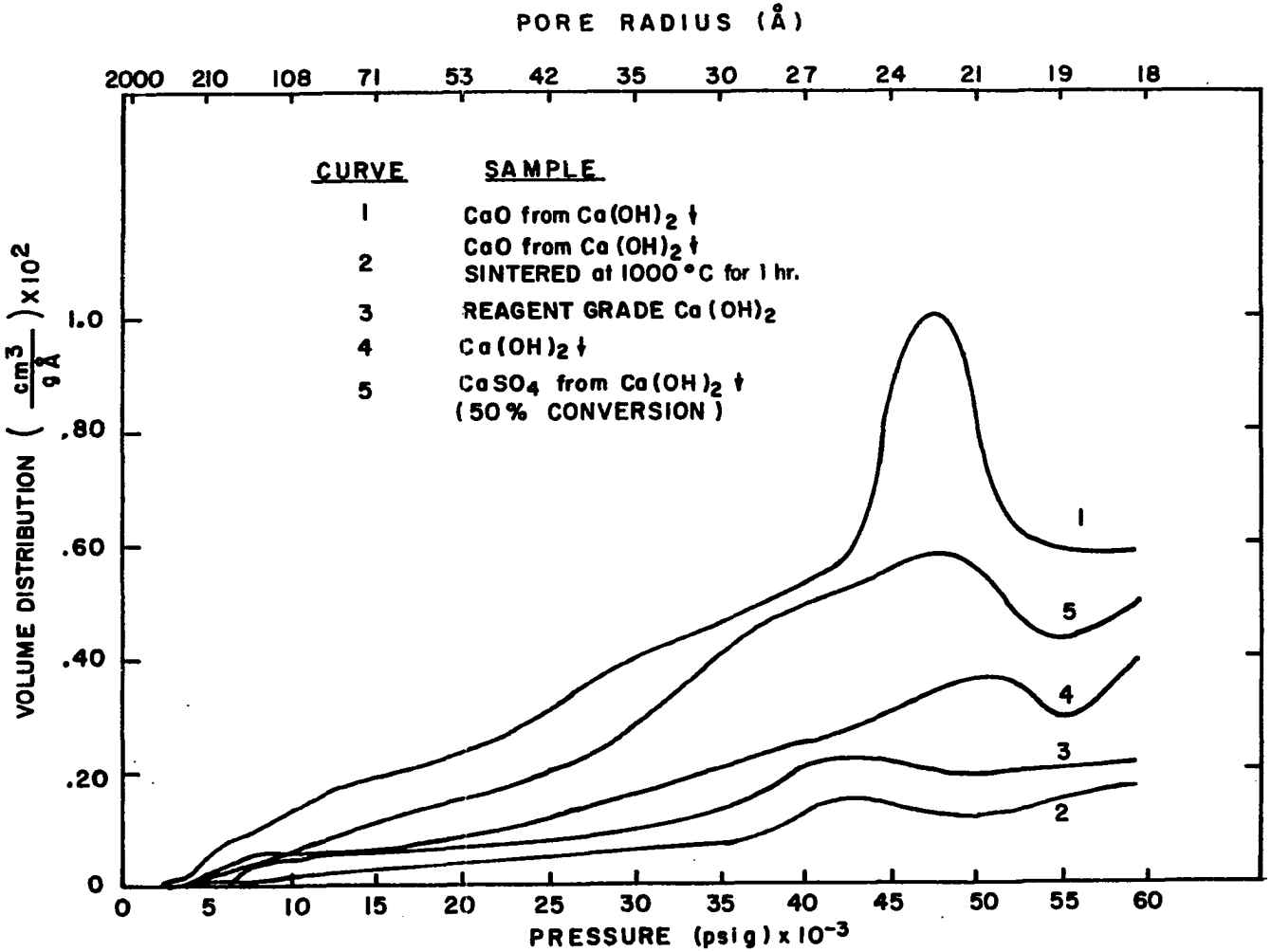

Figure 19. Pore volume distribution for various solids

The pore volume distributions calculated for these solids are shown in Figure 19. A very extensive micropore structure appears to exist within the grains of the solids, with pores as small as 18 Å in radius being indicated. The pore volume distribution is directly related to the slope of the cumulative pore volume versus pressure curve, divided by the differential in pore radius associated with the pressure range considered. The pores in this analysis are assumed to be cylindrical. In truth, the pores of the solid may be slit-like as reported by Beruto et al. [2]. However, for a rough comparison of the pore size distributions among the various solids, the assumption of cylindrical pores should be adequate.

The effect of calcination on the pore structure of $Ca(OH)_2$, deposited on a plate, can be seen by comparing curves 1 and 4 in Figure 19. The CaO has a greatly enhanced pore structure, with a large number of the pores having a radius of 22 Å. This was the only solid of those tested that displayed a relatively sharp peak in its pore size distribution. The others had fairly linear distributions with only small peaks at certain radii. Curve 5 shows the effect of sulfating the CaO to a conversion level of 50%. A relatively uniform decrease in the pore distribution is seen to occur, with the most significant decrease in pores occurring at a pore radius of 22 Å. Sintering the CaO for one hour at 1000°C greatly reduces the micropore structure of the grains, as shown by Curve 2.

When reagent grade $Ca(OH)_2$ is mixed with water to produce a slurry and then deposited on a glass plate, the microporosity of the resultant solid structure appears to be higher than the original material, as seen

from Curves 3 and 4. This could be caused by agglomeration of the grains to form small interstitial pores between the grains.

Using the Micromeritics Accusorb surface analyzer, a nitrogen desorption isotherm was obtained for solid 1, referred to in Figures 18 and 19. From the isotherm, a pore size distribution was calculated, assuming cylindrical pore geometry. A relatively sharp peak in pore size occurred at 19 Å, which corresponds very well with Curve 1 in Figure 19.

E. Conversion-Time Data for CaO Deposited on Quartz Plates

Figures 20 and 21 show the conversion-time data for the sulfation of presintered CaO at 930° and 835°C, respectively. These are the same data from which the initial rate information in Figure 15 was obtained. Each figure contains data obtained at the given temperature for several values of SO_2 mole fractions. The conversion curves at 930°C increase with increasing SO_2 mole fraction and the curves do not intersect. However, the curves at 835°C increase up to a SO_2 mole fraction of 0.01, at which point the curves begin to intersect at higher SO_2 levels. One could possibly explain the intersections of these curves by a pore plugging argument: At higher levels of SO_2 concentration, the mouths of the pores will begin to plug faster than the SO_2 can diffuse inside of the pores, thus resulting in lower conversion levels at higher SO_2 concentrations. However, this argument does not hold when comparing the curves at 835°C to those at 930°C. At SO_2 mole fractions of 0.005 and 0.01, the conversion curves at the two different temperatures are almost identical, while at higher SO_2 levels, the 930°C curves are all higher

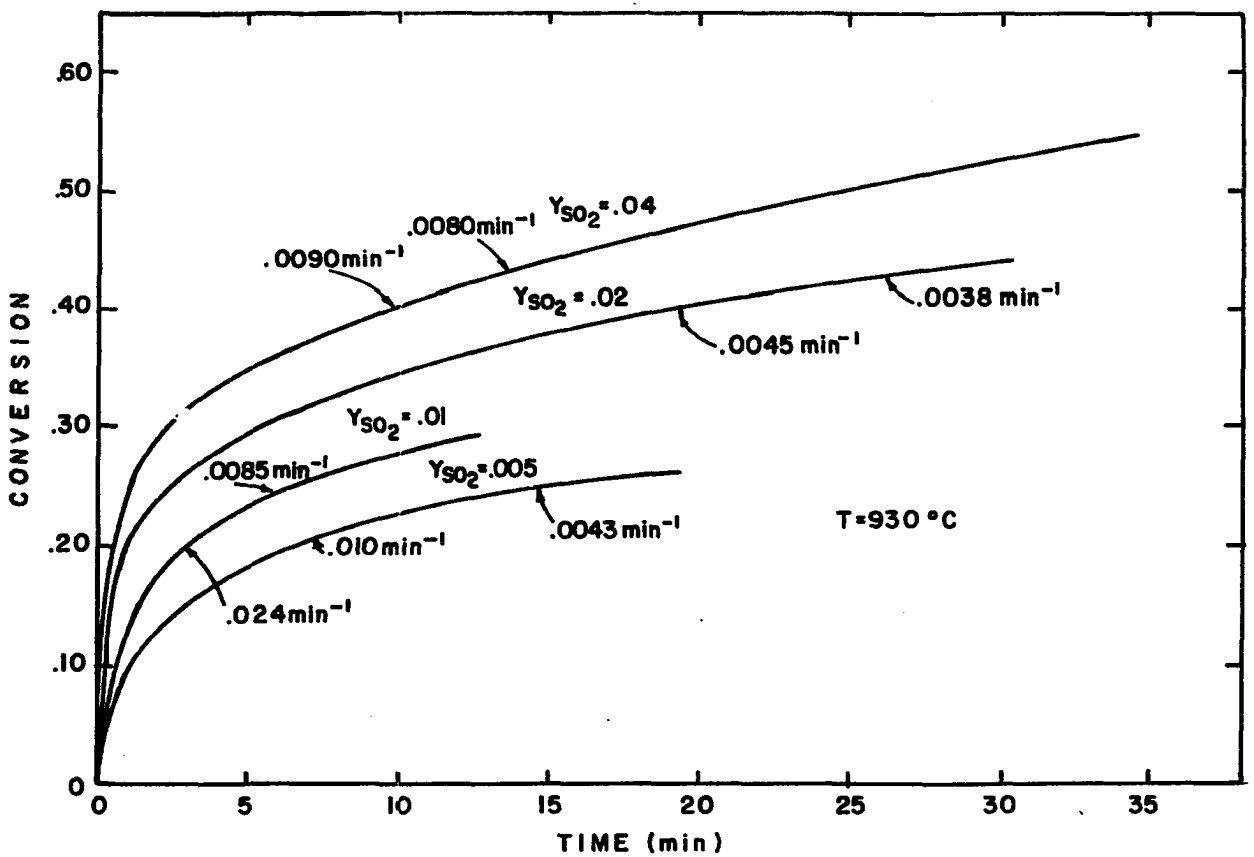

Figure 20. Conversion vs time for the sulfation of CaO on quartz plates, sintered at 1000°C for 30 minutes

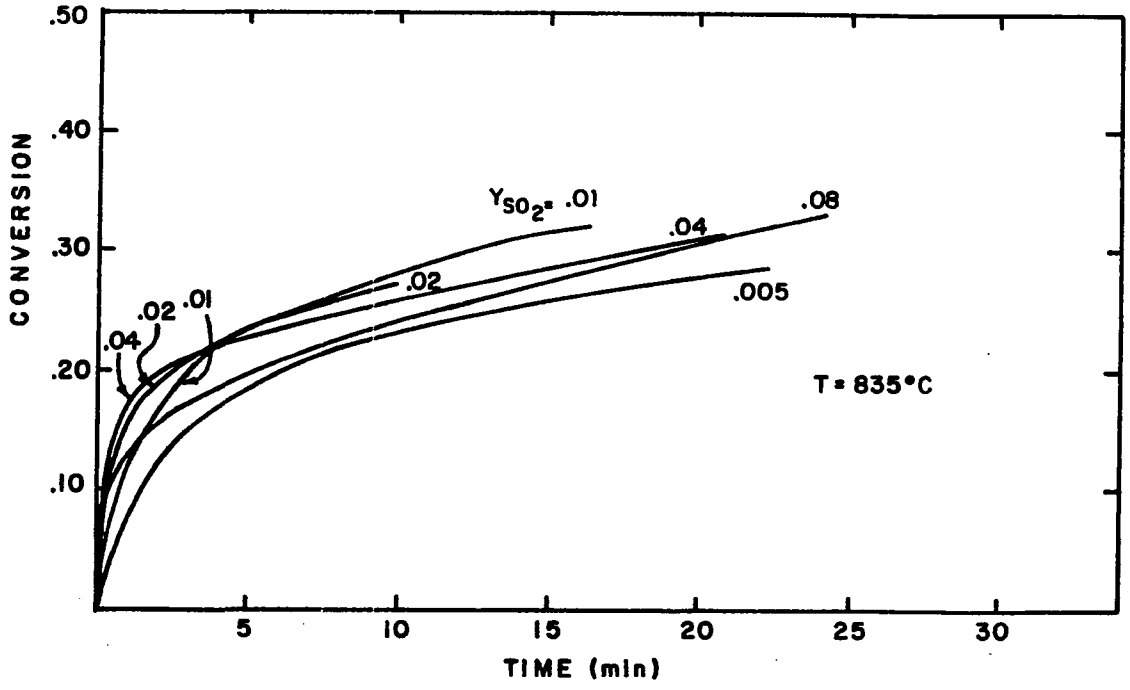

Figure 21. Conversion vs time for the sulfation of CaO on quartz plates, sintered at 1000°C for 30 minutes

than those at 835°C. If pore plugging within the grains was occurring, one would expect higher temperatures to result in lower conversion levels, but this is not observed.

In addition, none of the curves shown in Figures 20 and 21 contain a sharp break to a flat curve as would be predicted by a pore closure model. Even the 2 and 4% SO_2 curves at 835°C show a positive slope after a relatively sharp drop in reaction rate.

To explain the increase in conversion levels at higher temperatures, and at long time values where the reaction is no longer chemically controlled, one might argue the reaction is controlled by product layer diffusion. If product layer diffusion was controlling the reaction at high conversion levels, then an increase in temperature would increase the diffusion rate since solid-state diffusion is an activated process. This would give rise to higher reaction rates and higher overall conversion levels at higher temperatures, as observed in the data at 835° and 930°C.

At 930°C, in Figure 20, the reaction rates at selected levels of conversion for the various SO_2 concentrations are shown. Comparing the rates of the two upper curves at 40 and 43% conversion and then comparing the rates of the two lower curves at 20 and 25% conversion, the controlling mechanism for the reaction appears to be first order in SO_2 concentration. For example, at 40% conversion, the reaction rate for $y_{SO_2} = 0.02$ is 0.0045 min^{-1} and the reaction rate for $y_{SO_2} = 0.04$ is 0.0090 min^{-1}, so the rate is roughly proportional to SO_2 concentration. This is consistent with the notion of a product layer surrounding the

active surface area of CaO, so that at any given conversion level (or product layer thickness) doubling the bulk SO_2 concentration doubles the overall reaction rate.

One complication of this reaction that has been eliminated by sintering the CaO prior to reaction is the possibility of starting with different initial surface areas at different reaction temperatures, due to sintering of the CaO before reaction initiation. Since the samples were allowed five minutes to thermally equilibrate before the SO_2 flow was initiated, any unsintered CaO sample would tend to sinter during this five-minute period. This would lead to different initial surface areas at different reaction temperatures, since sintering is more rapid at higher temperatures. By presintering the CaO at 1000°C for 30 minutes, very little solid reactant sintering should occur during either the sample heat-up or reaction period.

Eliminating solid reactant sintering makes analysis of the data somewhat simpler; however, the effect of solid product sintering will still be present in the experimental data. Since sintering is defined as a porous media phenomenon, and the $CaSO_4$ product layer for this reaction is probably nonporous, "solid product sintering" is used to denote one of several mechanisms for solid movement, as listed on page 33. Perhaps the reason the curves at 835°C intersect and those at 930°C do not is an effect of this product layer sintering. Plug formation at a pore mouth may be hindered by product layer sintering since the product may begin to "flow" and not build up to form a plug. This would allow further reaction within the pore and may ultimately

lead to control by product layer diffusion.

No definite conclusions can be drawn from the kinetic data of Figures 20 and 21 alone. What is apparent is that pore closure, product layer diffusion, and product sintering are all important factors and that a combination of all three mechanisms makes the task of data analysis very difficult. In order to obtain a further understanding of how these mechanisms relate to each other and how they ultimately affect the conversion-time behavior, it is necessary to obtain more information on the structure of the solid and how it changes during reaction.

F. Solid-State Diffusivity

Using conversion-time data from the reaction of highly sintered CaO, estimates were made of the solid-state diffusivity, D_{As}, of SO_2 diffusing through a nonporous layer of $CaSO_4$. This was done by presintering CaO on quartz plates for 24 hours at 1000°C and then reacting the sintered material. This procedure greatly reduced the surface area of the CaO, which allowed product layer diffusion to become controlling at low conversion levels. The reactions were carried out at 841° and 932°C in 4% SO_2, 20% O_2, and the balance N_2. It was concluded the reaction was controlled by product layer diffusion at conversion levels as low as 4%, because of the high value of the activation energy obtained from the data. The value obtained (35.6 kcal/mole) was much higher than the chemical reaction activation energy found for these temperatures (19.1 kcal/mole). Table 6 shows the reaction rates measured for five separate experiments.

Table 6. Reaction rate measurements for the sulfation of CaO, presintered at 1000°C for 24 hours

T (°C)	X	$\bar{X}$	$\frac{dX}{dt}$ (min^{-1})	$\overline{\frac{dX}{dt}}$ (min^{-1})
841	.04	.07	.0031	.0033
	.10		.0035	
	.07		.0034	
932	.08	.08	.0087	.0090
	.08		.0093	

Two simple models were used to obtain D_{As} from the experimental data. One assumes the solid on a plate to be made up of uniform spherical grains, and the other pictures the solid as a thin slab of material. The solid in both models was assumed to be nonporous, which should be a good assumption since the samples were presintered for 24 hours. The interface between the product layer and solid reactant was assumed very sharp since the chemical reaction is much faster than solid-state diffusion. Negligible external mass transfer resistance was assumed which means the concentration of SO_2 at the outside surface of the product layer is equal to the bulk concentration. Pseudo-steady state was also assumed, or in other words, the transient term (dC_A/dt) was negligible.

The solid-state diffusion rate was written in the following form:

$$N_{As} = - D_{As} \frac{dC_A}{dz} \tag{79}$$

where N_{As} is the diffusive flux, D_{As} is the solid-state diffusivity of SO_2 through $CaSO_4$, and dC_A/dz represents the concentration gradient of SO_2 within the product layer. No bulk flow term was included in Equation (79) since the experimental concentrations of SO_2 were small.

Writing a mass balance on a spherical grain, as depicted in Figure 22a, gives the following differential equation:

$$r_g > r > r_c, \qquad \frac{d(r^2 N_{As})}{dr} = 0 \tag{80}$$

where r is the radial coordinate. Replacing z with r in Equation (79) and substituting into Equation (80) gives

$$\frac{d(D_{As} r^2 \frac{dC_A}{dr})}{dr} = 0 \tag{81}$$

with boundary conditions

$$\text{at } r = r_g, \; C_A = C_{Ab} \tag{82}$$

$$\text{and at } r = r_c, \; C_A = 0 \; . \tag{83}$$

The second boundary condition (Equation 83) comes from assuming that the reaction rate is much higher than the diffusion rate. Solution of Equations (81) to (83) gives the following concentration profile for SO_2 in the product layer:

$$r_g > r > r_c, \qquad C_A = C_{Ab} \left[\frac{\frac{1}{r_c} - \frac{1}{r}}{\frac{1}{r_c} - \frac{1}{r_g}} \right] \; . \tag{84}$$

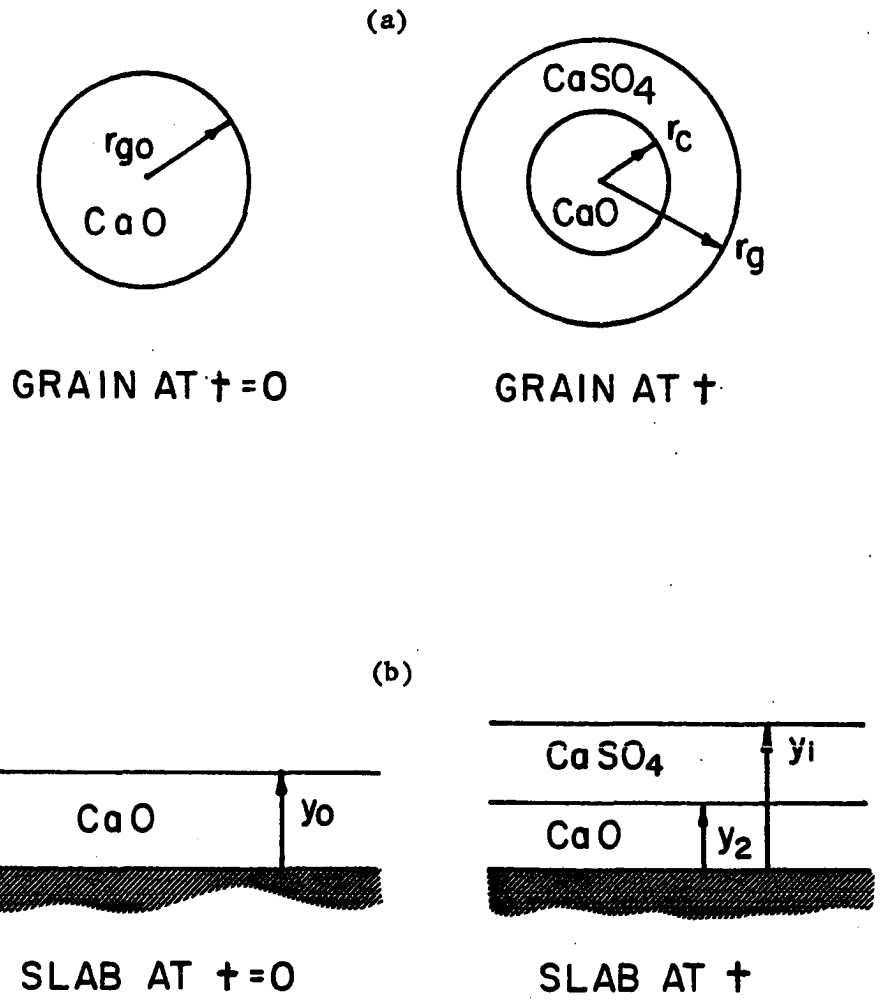

Figure 22. Depiction of spherical grain (a) and infinite slab (b) for solid-state diffusion model

If the reaction rate is controlled by product layer diffusion, the following rate equation can be written:

$$\text{Rate} = \left[4\pi r_g^{\,2}\right]\left[\frac{m_B}{\rho'_B \frac{4}{3}\pi r_{go}^{\,3}}\right]\left[D_{As}\left(\frac{dC_A}{dr}\right)_{r_g}\right] \tag{85}$$

where

Rate = overall reaction rate,

m_B = mass of CaO, and

ρ'_B = mass density of nonporous CaO.

In Equation (85), the first term in brackets represents the outside surface area of each grain, the second term is the total number of grains present, and the third term is the solid-state diffusion, per unit area, at the exterior surface of a grain. The gradient term in Equation (85) can be found from Equation (84):

$$\left(\frac{dC_A}{dr}\right)_{r_g} = \frac{\frac{C_{Ab}}{r_g^{\,2}}}{\frac{1}{r_c} - \frac{1}{r_g}} \; . \tag{86}$$

Then r_c and r_g can be expressed in terms of r_{go} and X using the following two identities:

$$r_c = r_{go}(1 - X)^{1/3} \; , \tag{87}$$

$$r_g = r_{go}\left[1 + (Z_E - 1)X\right]^{1/3} \; . \tag{88}$$

Substituting Equations (86-88) into Equation (85) and then solving for D_{As} gives

$$D_{As} = \frac{(\text{Rate})\ \rho'_B\ r_{go}^2}{3\ C_{Ab}\ m_B} \left[(1 - X)^{-1/3} - (1 + (Z_E - 1)X)^{-1/3}\right] . \tag{89}$$

Therefore, D_{As} can be found by experimentally measuring the overall reaction rate (Rate) at any given conversion level, X, where the reaction is known to be solid-state diffusion controlled. By measuring the initial surface area of the CaO, the value of r_{go} can be determined using

$$r_{go} = \frac{3}{\rho'_B\ A_s} \tag{90}$$

where A_s is specific surface area. Substituting r_{go} from Equation (90) into Equation (89) gives

$$D_{As} = \frac{3\ (\text{Rate})}{C_{Ab} m_B \rho'_B A_s^2} \left[(1 - X)^{-1/3} - (1 + (Z_E - 1)X)^{-1/3}\right] . \tag{91}$$

Using the same assumptions, a mass balance can be written on an infinite slab, as shown in Figure 22b, giving the following:

$$\frac{d(N_{As})}{dy} = 0 \tag{92}$$

where y is the length corrdinate. Replacing z with y in Equation (79) and substituting into Equation (92) gives

$$\frac{d(D_{As}\frac{dC_A}{dy})}{dy} = 0 \qquad (93)$$

with the boundary conditions

$$\text{at } y = y_1,\ C_A = C_{Ab} \qquad (94)$$

$$\text{and at } y = y_2,\ C_A = 0\ . \qquad (95)$$

Solution of Equations (93) to (95) gives the following concentration profile:

$$y_1 > y > y_2, \qquad C_A = C_{Ab}\left(\frac{y - y_2}{y_1 - y_2}\right)\ . \qquad (96)$$

For product layer diffusion control, the following rate expression can be written:

$$\text{Rate} = A_s m_B D_{As}\left(\frac{dC_A}{dy}\right)_{y_1}\ . \qquad (97)$$

In Equation (97), the quantity $A_s m_B$ represents the total surface area available for diffusion. The gradient term can be found from Equation (96) to be

$$\left(\frac{dC_A}{dy}\right)_{y_1} = \frac{C_{Ab}}{y_1 - y_2}\ . \qquad (98)$$

From geometric considerations

$$(y_1 - y_2) = Z_E X y_o\ . \qquad (99)$$

Combination of Equations (97) to (99) and solving for D_{As} leads to

$$D_{As} = \frac{(\text{Rate})Z_E X y_o}{C_{Ab} A_s m_B} \quad . \tag{100}$$

The original slab thickness, y_o, can be found from the initial surface area:

$$y_o = \frac{1}{\rho'_B A_s} \tag{101}$$

Substitution of y_o from Equation (101) into Equation (100) gives, finally

$$D_{As} = \frac{(\text{Rate})Z_E X}{C_{Ab} m_B \rho'_B A_s^2} \quad . \tag{102}$$

The specific surface area of the presintered CaO was experimentally determined by depositing $Ca(OH)_2$ on small (0.5 cm) fragments of quartz and then sintering the material for 24 hours at 1000°C. The fragments were then transferred to a BET flask and the surface area of the material was determined using krypton as the adsorbate gas. A blank run with clean quartz fragments was also performed to determine the maximum possible surface area contributed by the quartz. The specific surface area of the sintered material was found to be $0.111 \pm .001$ m^2/g, while that of the clean quartz fragments was $0.004 \pm .001$ m^2/g. By taking into account the ratio of CaO weight to quartz weight, the minimum value for the surface area of the CaO solid was calculated to be 0.088 m^2/g. This assumes none of the exterior surface of the quartz

was covered by the CaO and therefore, represents the minimum value of the specific surface area of the sintered CaO. The value of 0.111 m^2/g corresponds to the maximum possible surface area of the CaO.

Using the average conversion levels and reaction rates shown in Table 6, estimates of D_{As} were calculated using Equations (91) and (102). Table 7 shows the results of these calculations. The minimum and maximum estimates of the specific surface area of the presintered CaO were both used to show the effect of this parameter on the determination of D_{As}. The value of A_s used in the two models has an inverse, second order effect on the predicted value of D_{As}.

Table 7. Solid-state diffusivity estimates

Model	A_s (m^2/g)	T (^oC)	D_{As} (cm^2/sec)	Activation energy (kcal/mole)
Slab model	.088	841	19×10^{-8}	35.6
		932	63×10^{-8}	
	.111	841	12×10^{-8}	35.6
		932	40×10^{-8}	
Spherical grain model	.088	841	18×10^{-8}	35.5
		932	63×10^{-8}	
	.111	841	11×10^{-8}	35.5
		932	40×10^{-8}	

At any given value of temperature, the predictions of D_{As} by the two models are very close. This is expected since the reaction rates were measured at low conversion levels. The limit of the right-hand side of Equation (91) as X approaches zero gives the right-hand side of Equation (102). Therefore, at low conversion levels, the equation for D_{As} from the spherical grain model reduces to the D_{As} equation from the slab model. In other words, the value of D_{As} determined using this method is nearly independent of the assumed geometry. The only geometric parameter necessary for the determination is the value of the initial specific surface area of the solid.

Comparing the solid-state diffusivity estimates from this study (Table 7) to those in the literature (Table 2), one can see that most of the estimates have the same order of magnitude. The closest values to the present estimates are those given by Bhatia and Perlmutter [4]. An average activation energy of 35.6 kcal/mole was found in this study, which is somewhat higher than the values shown in Table 2. The values reported in Table 2 were all found by treating D_{As} as an adjustable parameter in a grain or pore model, and varying the value of D_{As} in the model to obtain the best fit of experimental data. Finding D_{As} in this manner implicitly assumes that the model does indeed describe the system accurately and that the set of parameters thus obtained is mutually exclusive. The large range of values reported in Table 2 is indicative of the uncertainty of this method.

By obtaining D_{As} without the use of the model it will later be incorporated into, the accuracy of the model can then truly be tested.

While the solid-state diffusivities calculated in this study are not independent of some simplifying assumptions, they are much less model dependent than those presented in Table 2. In addition, none of the models used in Table 2 accounted for the surface area reduction caused by sintering during the reaction period. Although sintering of the product occurred here as well, the presintered reactant should not have sintered during reaction. For these reasons, the solid-state diffusivity values presented here are expected to be closer to the real values of D_{As} for this reaction system.

G. Conversion-Time Data for CaO Pellets

1. Effect of porosity

Two pellets with different initial porosities were reacted at similar conditions to see the effect of this parameter on the conversion-time behavior. The different initial porosities were produced by pressing the powder at 2000 and 20,000 psi for the high and low porosity pellets, respectively. The mass of powder used in the high porosity pellet was lower than that in the low porosity pellet, in order to obtain the same overall dimensions for the pellets.

Figure 23 shows the conversion-time curves for these two pellets. The high porosity pellet (ε_o = .69) reacts much faster than the low porosity pellet (ε_o = .62) during the initial 10 minutes, but then the low porosity reaction rate exceeds that of the high porosity solid. The overall conversion level, after 40 minutes, is higher for the high porosity pellet as expected since the reaction is accompanied by product layer expansion.

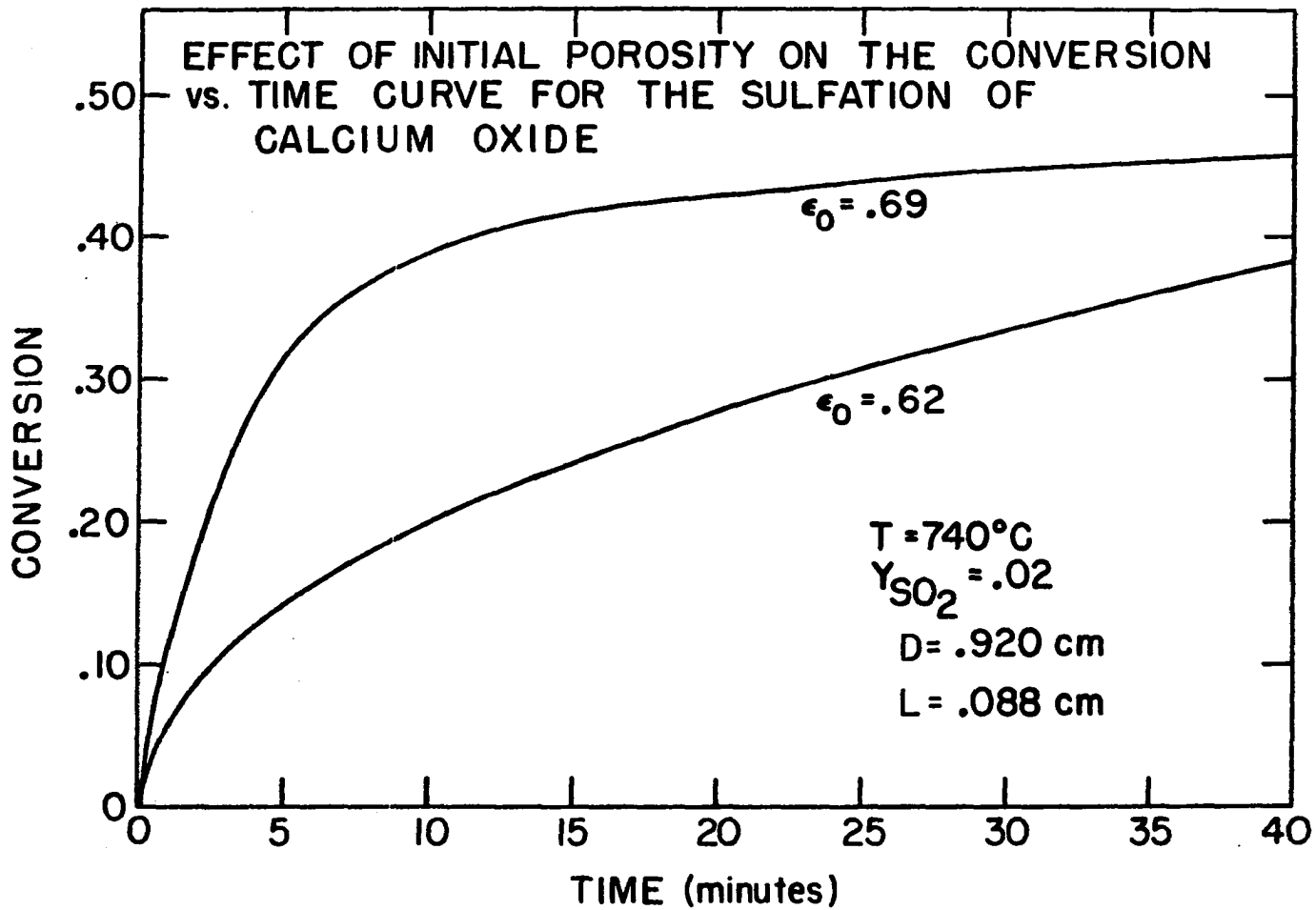

Figure 23. Effect of initial porosity on the conversion vs time curve for the sulfation of calcium oxide pellets

2. Effect of bulk SO_2 concentration

Figure 24 shows the conversion-time data for two similar pellets reacted in different bulk concentrations of SO_2. Each pellet had the same initial porosity and the reactions were carried out at 740°C. The reaction carried out in 5 mole % SO_2 achieved higher conversion levels than that at 2 mole % SO_2. This was expected since a high concentration of SO_2 favors intrapellet diffusion, product layer diffusion, and also the chemical reaction rate.

3. Effect of temperature

Figure 25 shows conversion-time data for CaO pellets reacted in 5% SO_2 at various temperatures. The curves appear to intersect each other in a very complex fashion. Even though the initial rates increase with increasing temperature up to 930°C, the conversion levels after 40 minutes are observed to increase only up to 745°C, at which point they decrease with increasing temperature. There are two possible explanations for this drop in conversion level with increasing temperature. One possibility is that sintering of the reactant solid and product begins to occur at significant rates above 745°C, thus lowering the surface area and porosity of the solid. This would reduce the reaction rate and ultimate conversion of the solid. This possibility is supported by the fact that pellet shrinkage was observed for reactions carried out at temperatures above 745°C.

Another explanation for reduced conversion levels at higher temperatures is the effect of pore plugging. As reaction temperature increases, the SO_2 molecules that diffuse into the pellet will tend to

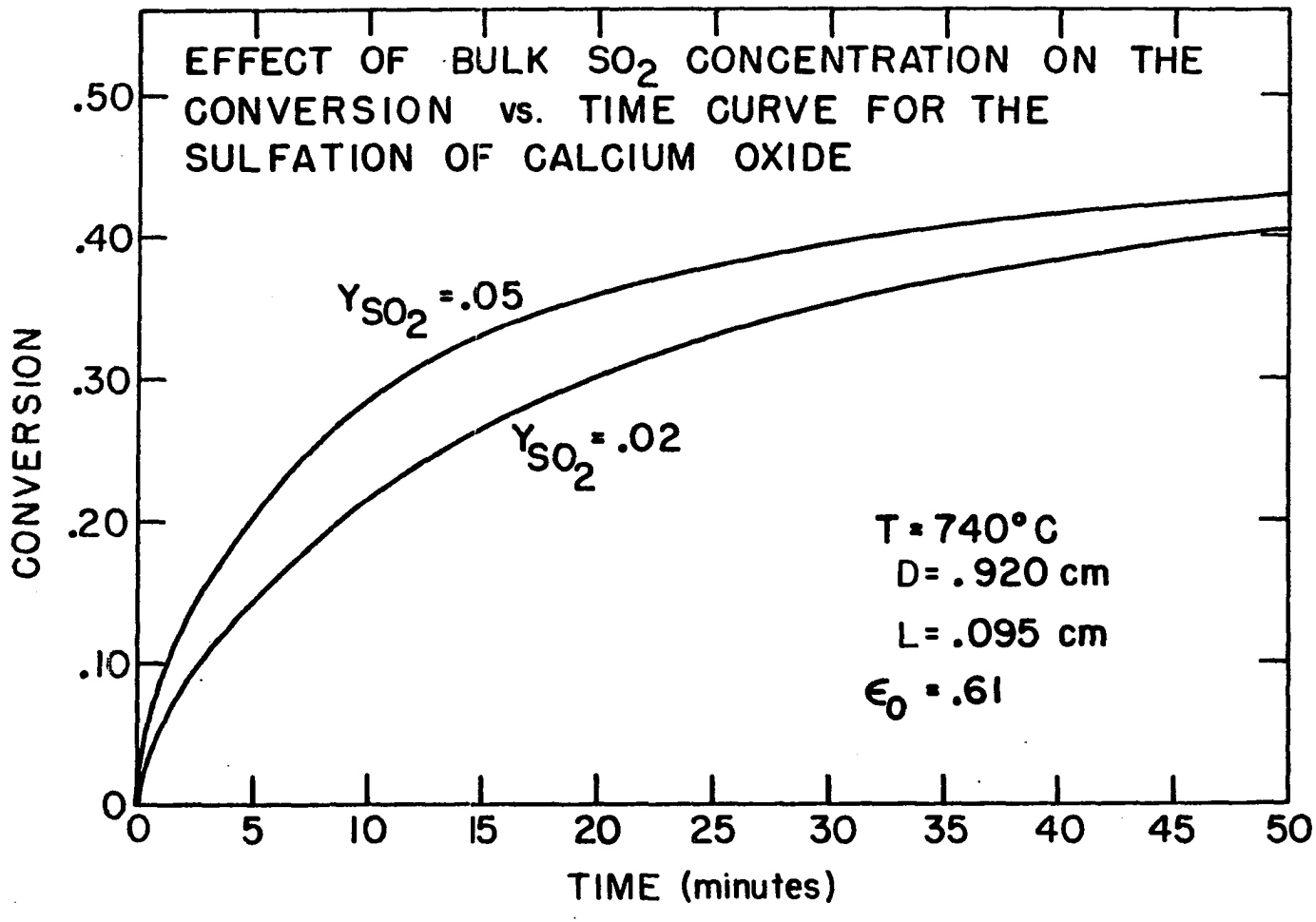

Figure 24. Effect of bulk SO_2 concentration on the conversion vs time curve for the sulfation of CaO pellets

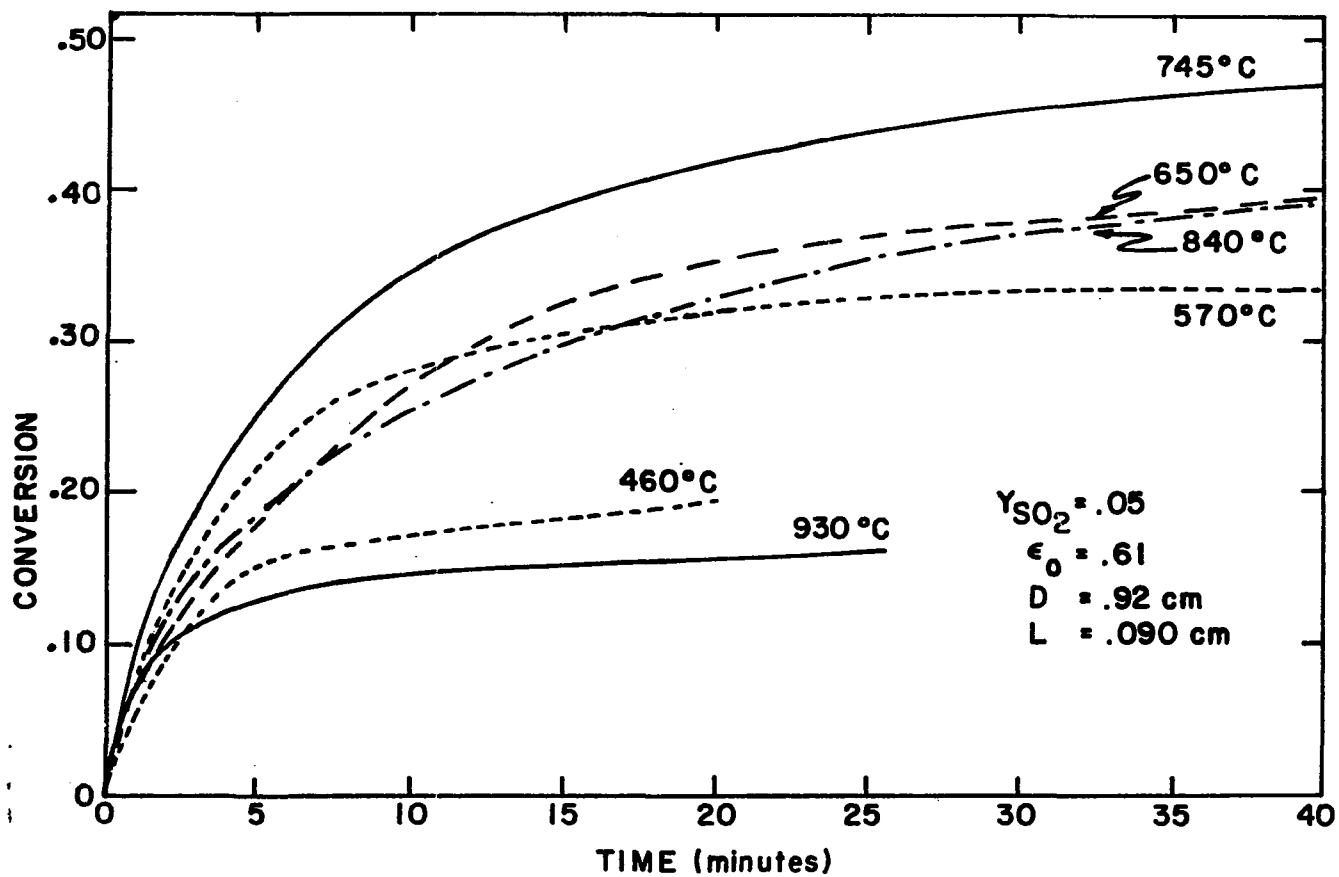

Figure 25. Effect of temperature on the conversion-time data for the sulfation of CaO pellets

react very rapidly rather than diffuse deeper into the pellet interior. The chemical reaction activation energy is higher than that for intrapellet diffusion and therefore, higher temperatures favor the chemical reaction rate. This could cause a build-up of product, and eventually plug off the mouths of the pores leading to the interior regions of the pellet, resulting in lower conversion levels.

For these reaction conditions, the optimum reaction temperature is observed to be 745°C. For this discussion, "optimum" refers to the set of parameters which gives the highest overall conversion level after 40 minutes of reaction.

Figure 26 shows conversion-time data for reaction in 2 mole % SO_2 at various temperatures. The curves appear to be in a tighter grouping than those in Figure 25 (5 mole % SO_2). However, the optimum temperature is still around 740°C.

Holding the bulk concentration at 2 mole % SO_2, but increasing the initial pellet porosity from 0.61 to 0.69 resulted in the data shown in Figure 27. The curves are more spread out than in the previous case (Figure 26). In addition, the optimum temperature has changed from 740°C to 835°C. Increasing the porosity also increased the final conversions over those in Figure 26 for every temperature except 460°C.

4. Effect of grain size

To determine the effect of grain size on the conversion-time behavior of this reaction, an attempt was made to classify reagent grade $Ca(OH)_2$ powder into different grain size fractions using sonic screening. Four screens were used which had nominal mesh sizes of 45, 20, 10 and 5

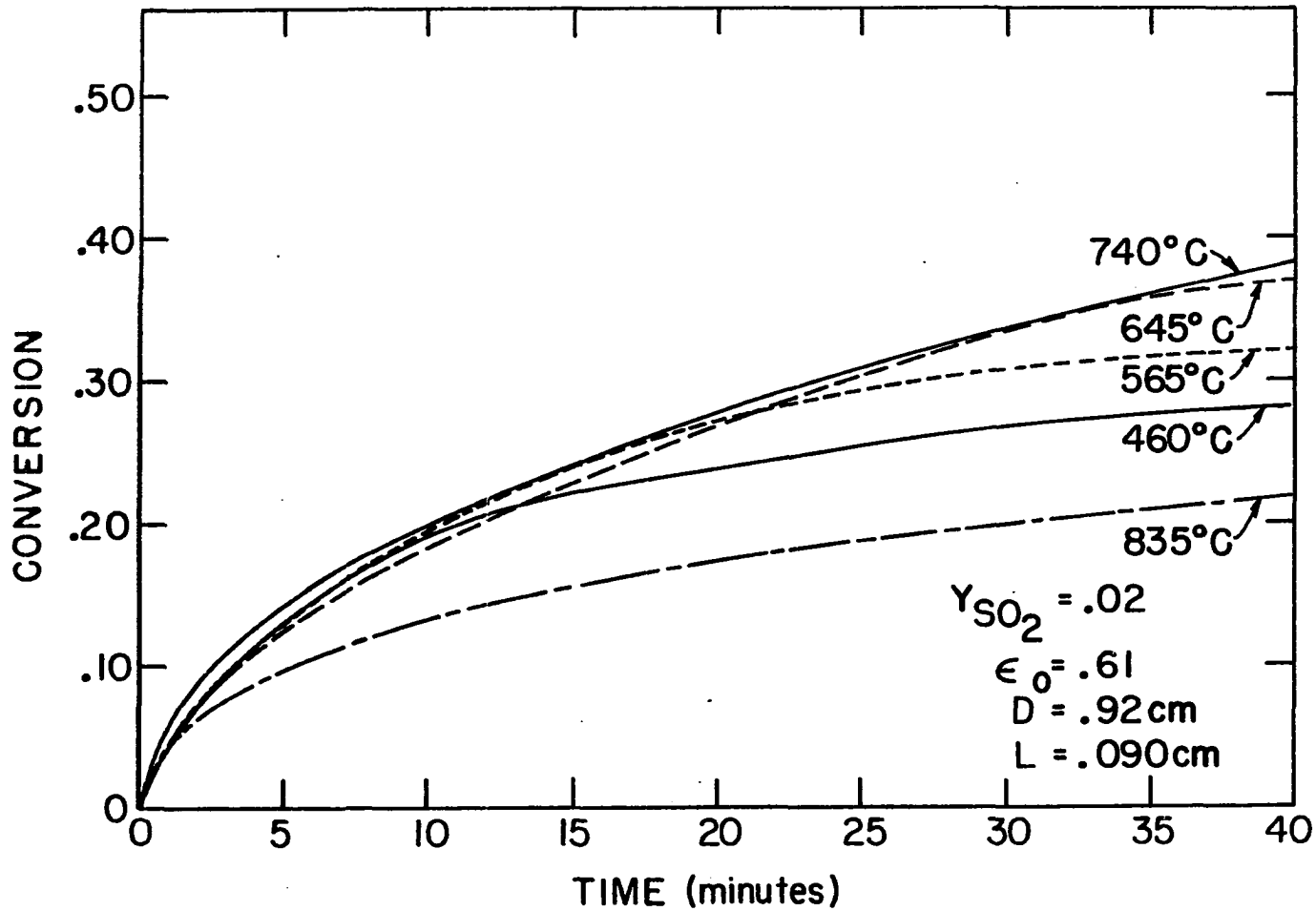

Figure 26. Effect of temperature on the conversion-time data for the sulfation of CaO pellets

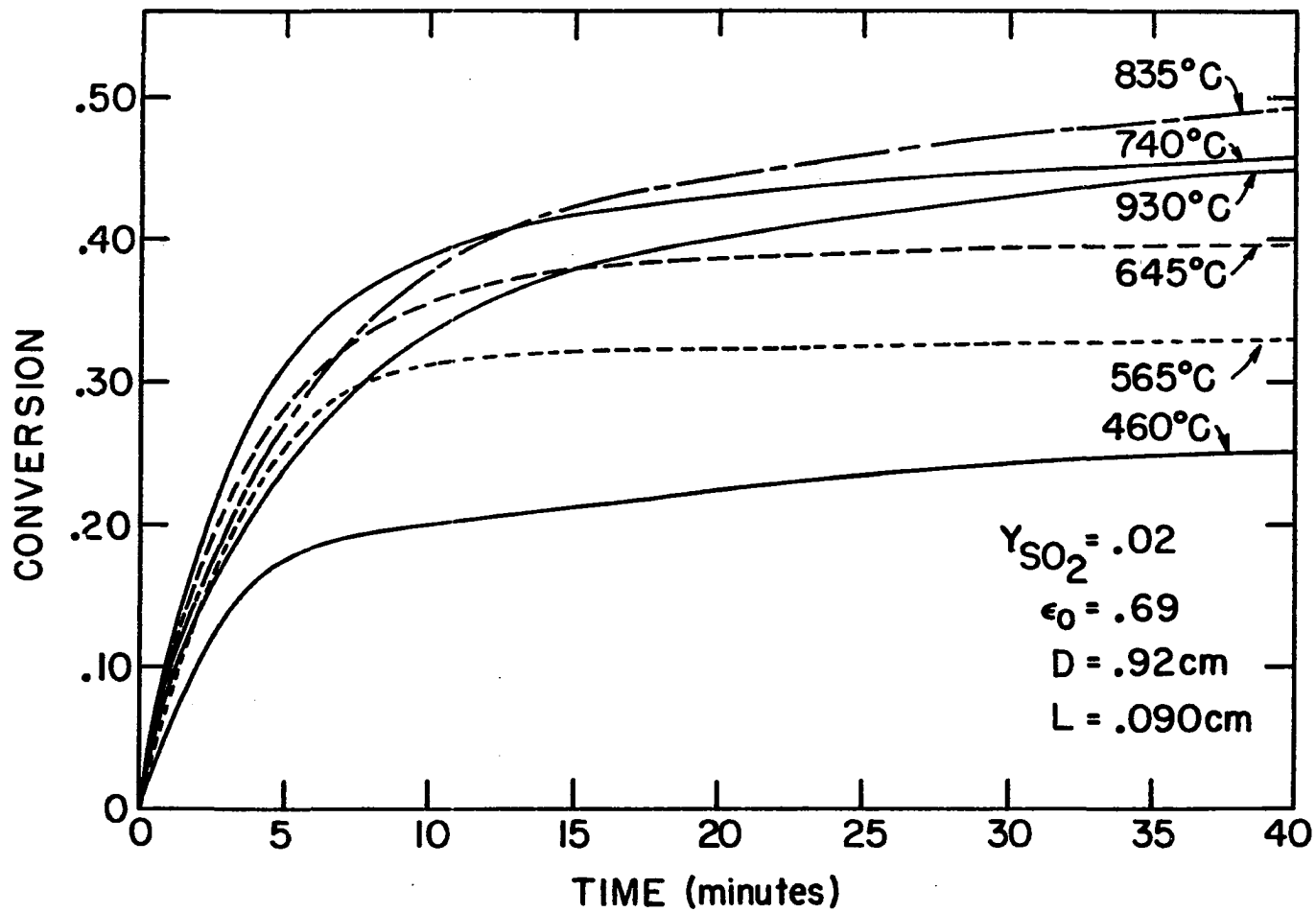

Figure 27. Effect of temperature on the conversion-time data for the sulfation of high porosity CaO pellets

microns. Approximately 1 gram of powder was placed on the top screen and was allowed to separate into different fractions using sonic vibration. After about one hour, most of the powder was found to be on the 20 and 10 micron screens. No detectable amount of powder went through either the 10 or 5 micron screens.

Using the powder from the 20 and 10 micron screens, pellets were pressed at 20,000 psi and then reacted with 5 mole % SO_2 at 640°, 740°, and 790°C. The conversion-time curves for the two fractions were not greatly different from each other at any of the reaction temperatures. In addition, grain size distribution measurements from a Coulter counter showed the two powders were similar in average grain size and grain size distribution. Therefore, this method of producing different grain sizes was apparently inadequate.

Another attempt to produce different grain sizes within pellets was made by presintering pellets prior to reaction. Sintering causes grain growth, so by presintering pellets for varying periods of time, it was possible to form different average grain sizes within the pellets. Four sets of pellets were presintered at 1000°C for 30 minutes, 2 hours, 5 hours, and 24 hours, respectively. The surface areas and porosities of the pellets were measured after the presintering treatments, and the results are shown in Table 8. Both the surface area and porosity values tend to drop with increasing sintering time and approach asymptotic values. Figure 28 shows a plot of pellet surface area versus sintering time, which illustrates this asymptotic behavior. The drop in pellet porosity was due to shrinkage of the pellet diameter, while the pellet

Table 8. Data on the sulfation of CaO pellets

Presintering time (hr)	Initial porosity	Initial surface area (m^2/g)	Conversion after 40 minutes of reaction in 5% SO_2			
			646°C	742°C	836°C	929°C
0	.61	33.0	.396	.472	.392	.180
0.5	.57	5.9	.216	.303	.451	.335
2	.56	3.9	.200	.283	.436	.420
5	.54	3.5	.151	.212	.368	.442
24	.51	1.4	.016	.031	.080	.192

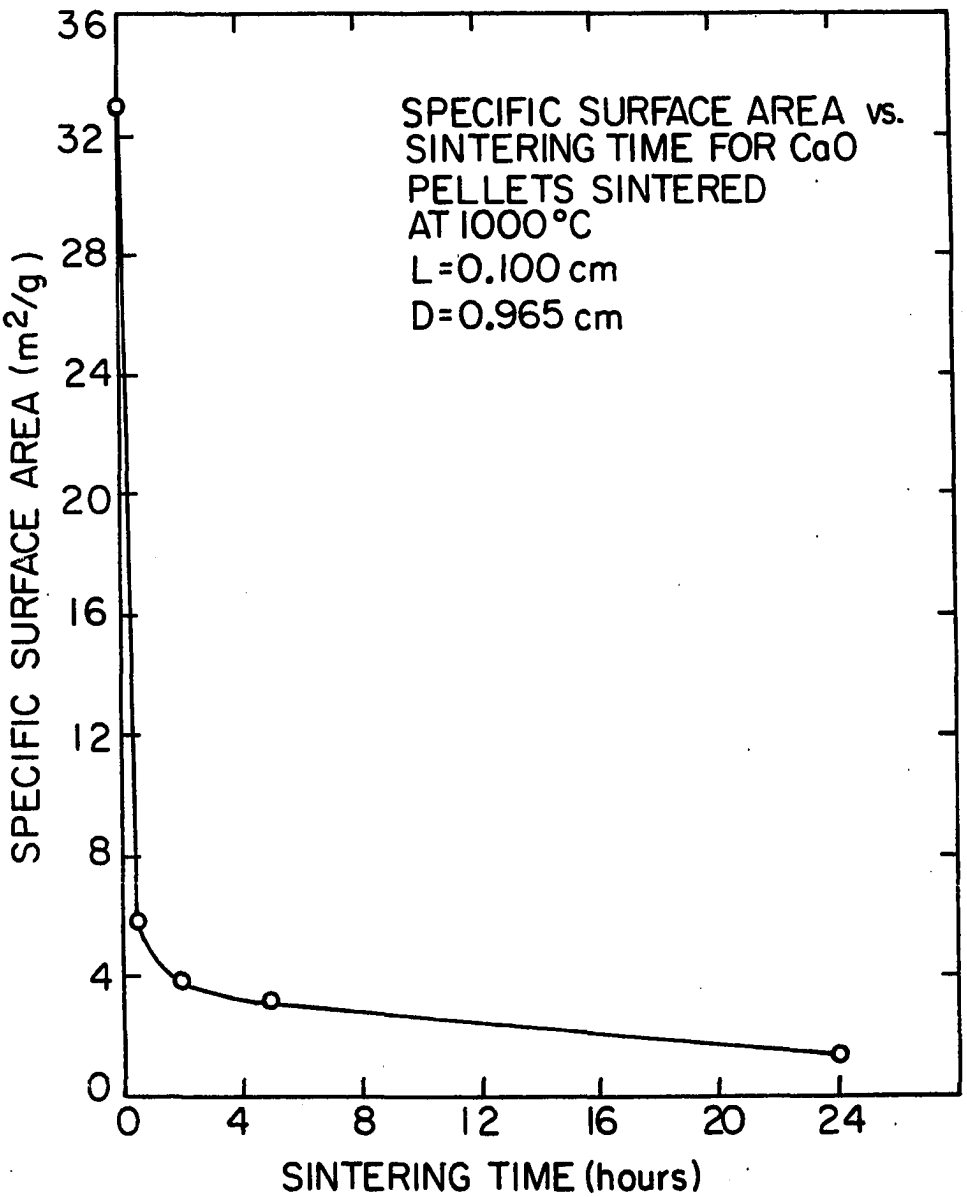

Figure 28. Specific surface area vs sintering time for CaO pellets sintered at 1000°C

length remained fairly constant during sintering.

The pellets from each presintering group were reacted in 5% SO_2 over a range of temperature between 646° and 929°C to see the effect of presintering on the conversion-time behavior. Figures 29-32 show plots of conversion versus time for the different pellet groups and Table 8 summarizes the conversion levels after 40 minutes of reaction for each group of pellets. By comparing the data obtained for the unsintered pellets with those of the pellets presintered for increasing amounts of time, it can be seen that the optimum temperature does not remain constant. The optimum temperature changes from 742°C for the unsintered pellets, to 836°C for those sintered for 30 minutes. Somewhere after 2 hours of presintering at 1000°C, the optimum temperature becomes 929°C and the relative difference between the 929° and 836°C conversion curves becomes greater as presintering time increases from 2 to 24 hours.

As was observed in Figures 26 and 27, decreasing the initial porosity causes a decrease in the optimum temperature. Therefore, for these experiments where initial porosity is decreasing and initial grain size is increasing, with increasing presintering time, the upward shift in optimum temperature must be caused by the increasing grain size. As presintering time increases, the downward effect of decreasing initial porosity on the optimum temperature is overshadowed by the upward effect of increasing grain size on this temperature.

From Table 8, it is observed that the final conversion levels (after 40 minutes) for the pellets reacted at 646° and 742°C, drop continuously with presintering time. For those reacted at 836°C, the

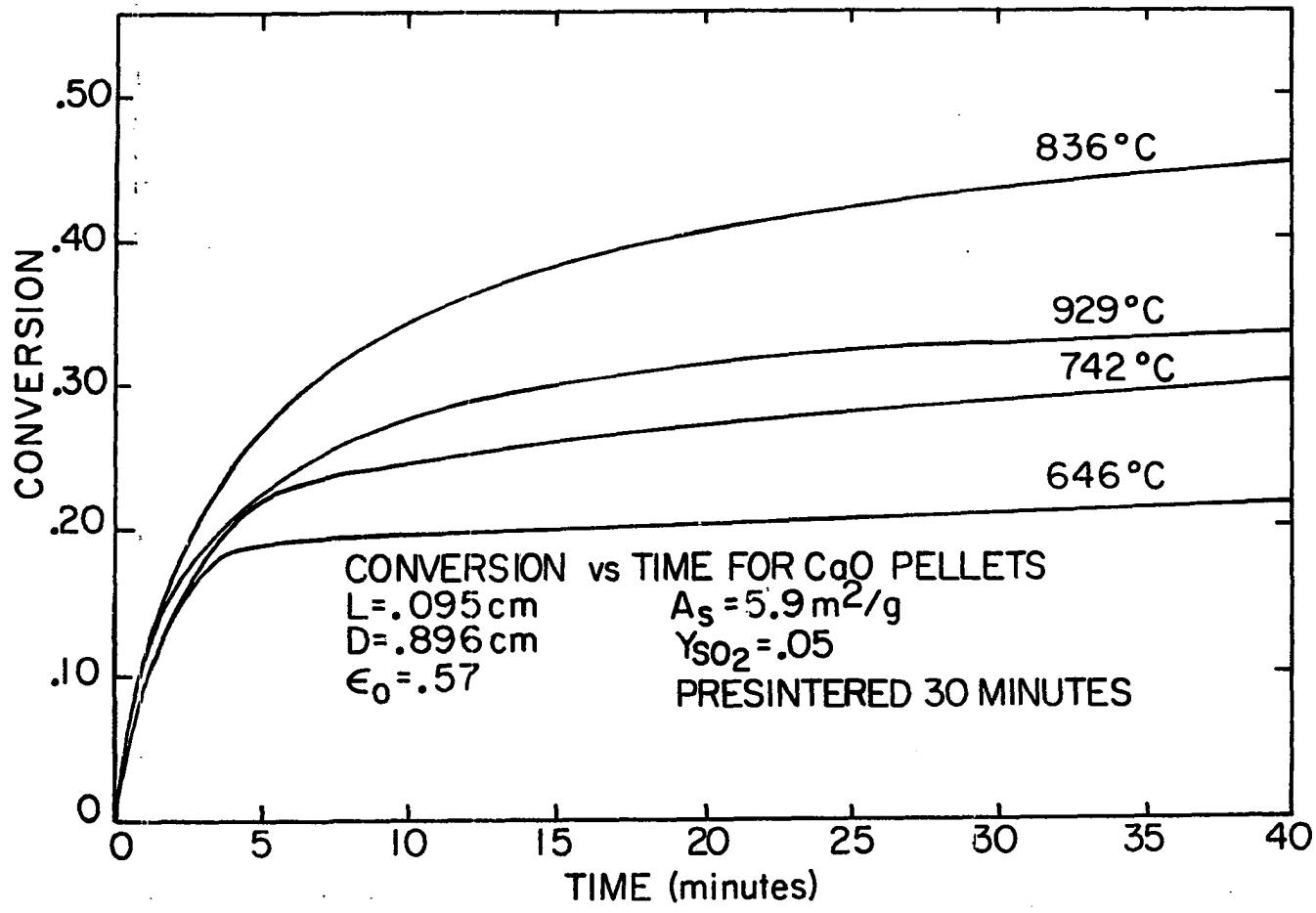

Figure 29. Conversion-time data for the sulfation of CaO pellets, presintered at 1000°C for 30 minutes

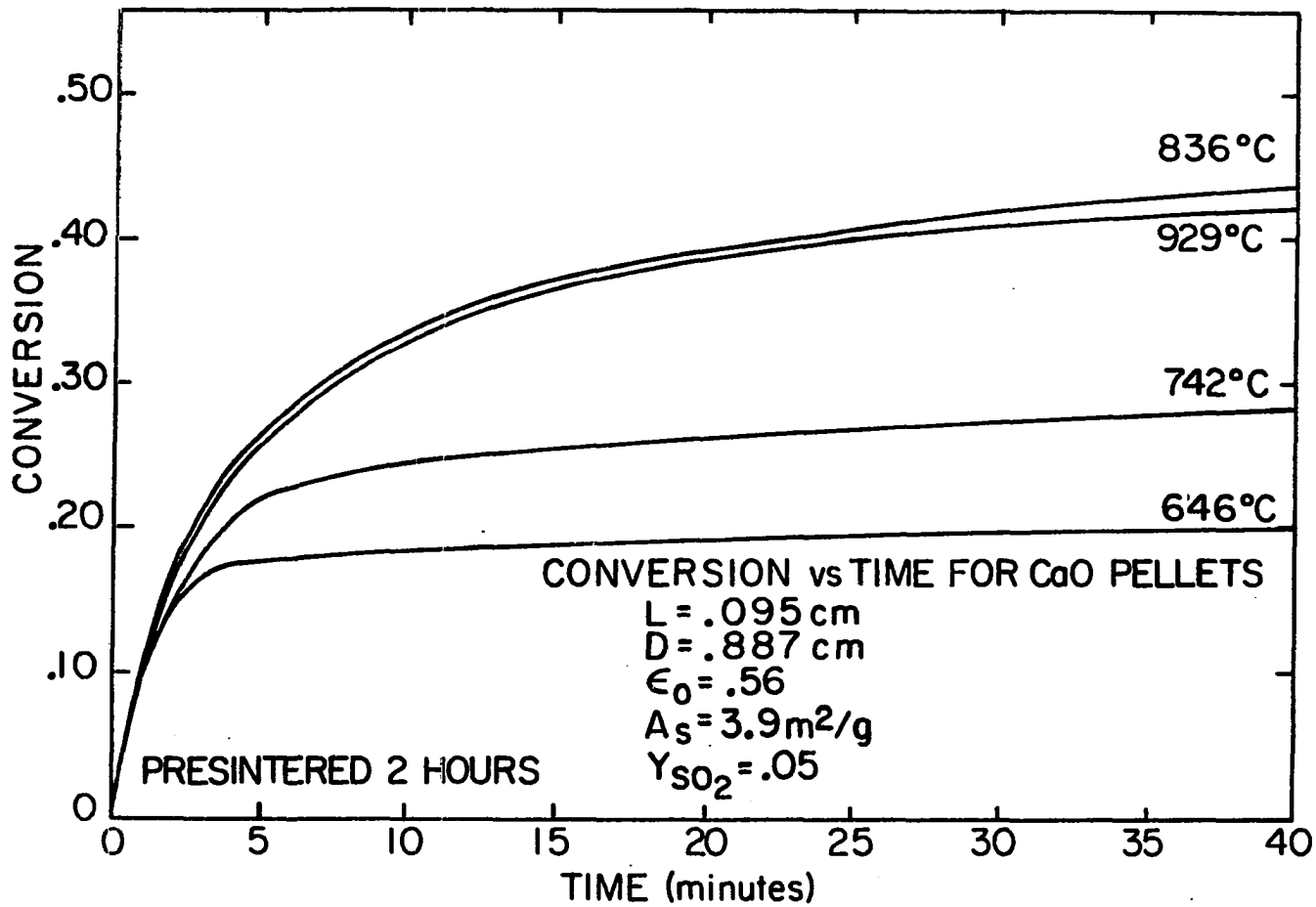

Figure 30. Conversion-time data for the sulfation of CaO pellets, presintered at 1000°C for 2 hours

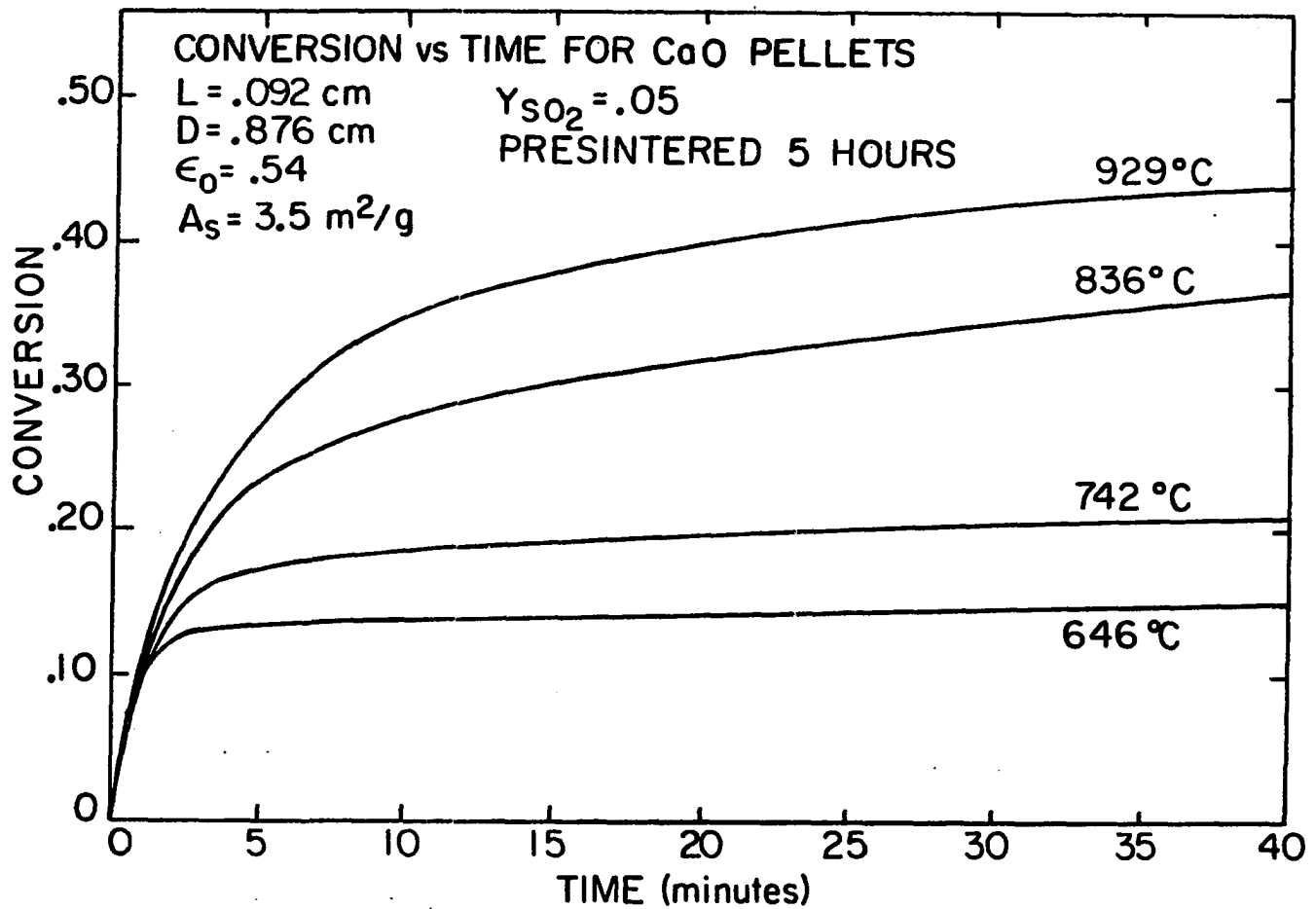

Figure 31. Conversion-time data for the sulfation of CaO pellets, presintered at 1000°C for 5 hours

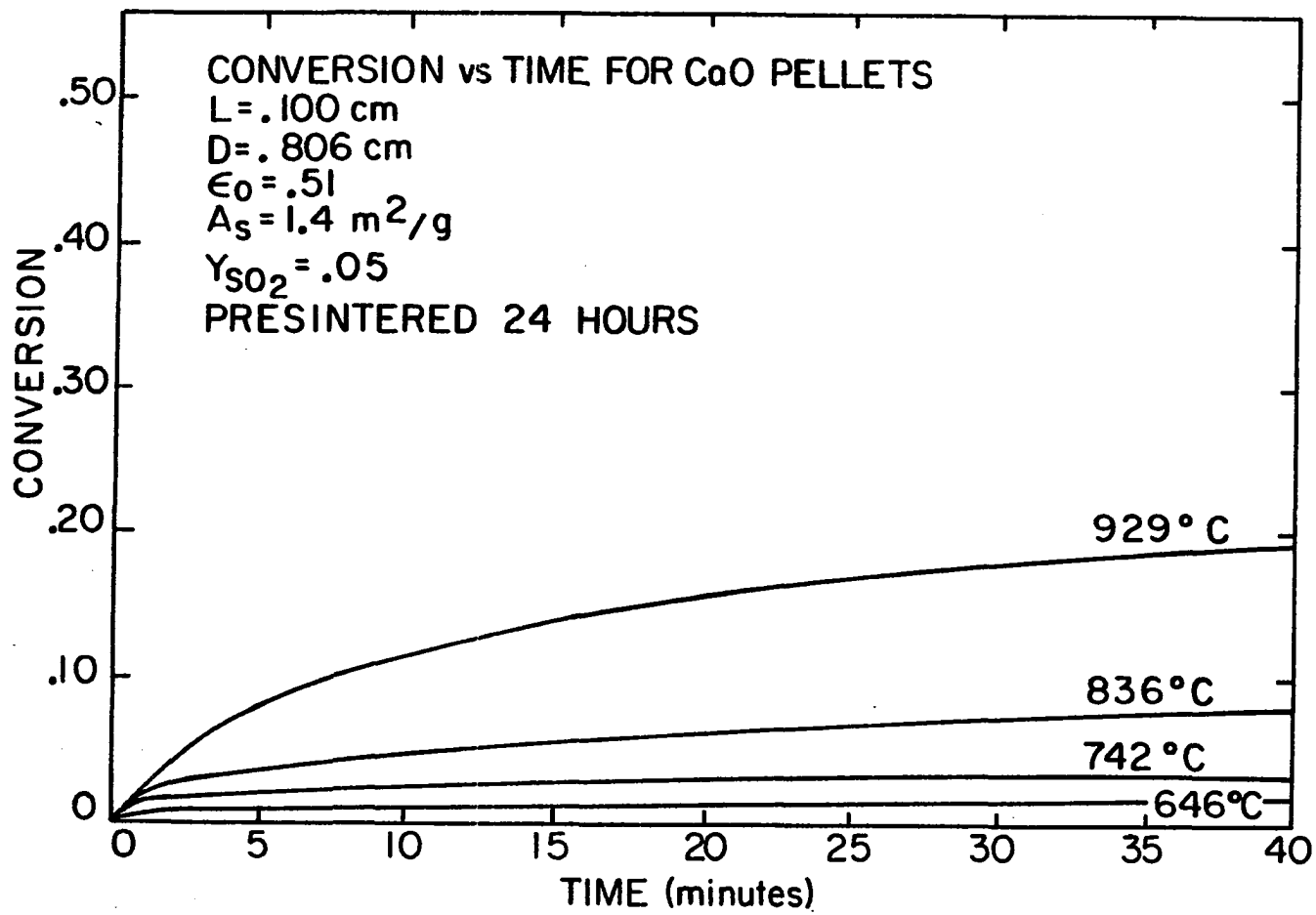

Figure 32. Conversion-time data for the sulfation of CaO pellets, presintered at 1000°C for 24 hours

final conversion levels increase up to 30 minutes of presintering and then begin to drop at longer presintering times. In the case of 929°C, the final conversion levels increase all the way up to 5 hours of presintering, at which point they begin to fall.

H. Pellet Center Temperature During Reaction

One of the assumptions commonly made in gas-solid reaction models is isothermality. To test the validity of this assumption for this particular reaction system, temperature measurements were taken for reacting pellets. Thermocouples (chromel-alumel) were implanted in the centers of cylindrical pellets by pressing $Ca(OH)_2$ powder directly around the thermocouple beads. This was performed using a two-holed plug within the cylindrical die that allowed the thermocouple wires to extend outside of the die while the pellet was being pressed. The finished pellet had the thermocouple bead lying directly in the center, with the two wires emerging from one of the flat surfaces. An ice bath was used as the reference junction.

Pellets of three different sizes were reacted to note the effect of pellet dimensions on the temperature versus time behavior. Figure 33 shows a plot of pellet center temperature versus time for the three pellets reacted at 560°C in 2 mole % SO_2. In each case, the pellet temperature rises sharply during the first few seconds of reaction, and then slowly decreases until it asymptotically reaches the gas temperature (initial pellet temperature). Table 9 summarizes the maximum center temperature inside the pellet for the three different sized pellets. As expected, the highest maximum center temperature occurred for the largest

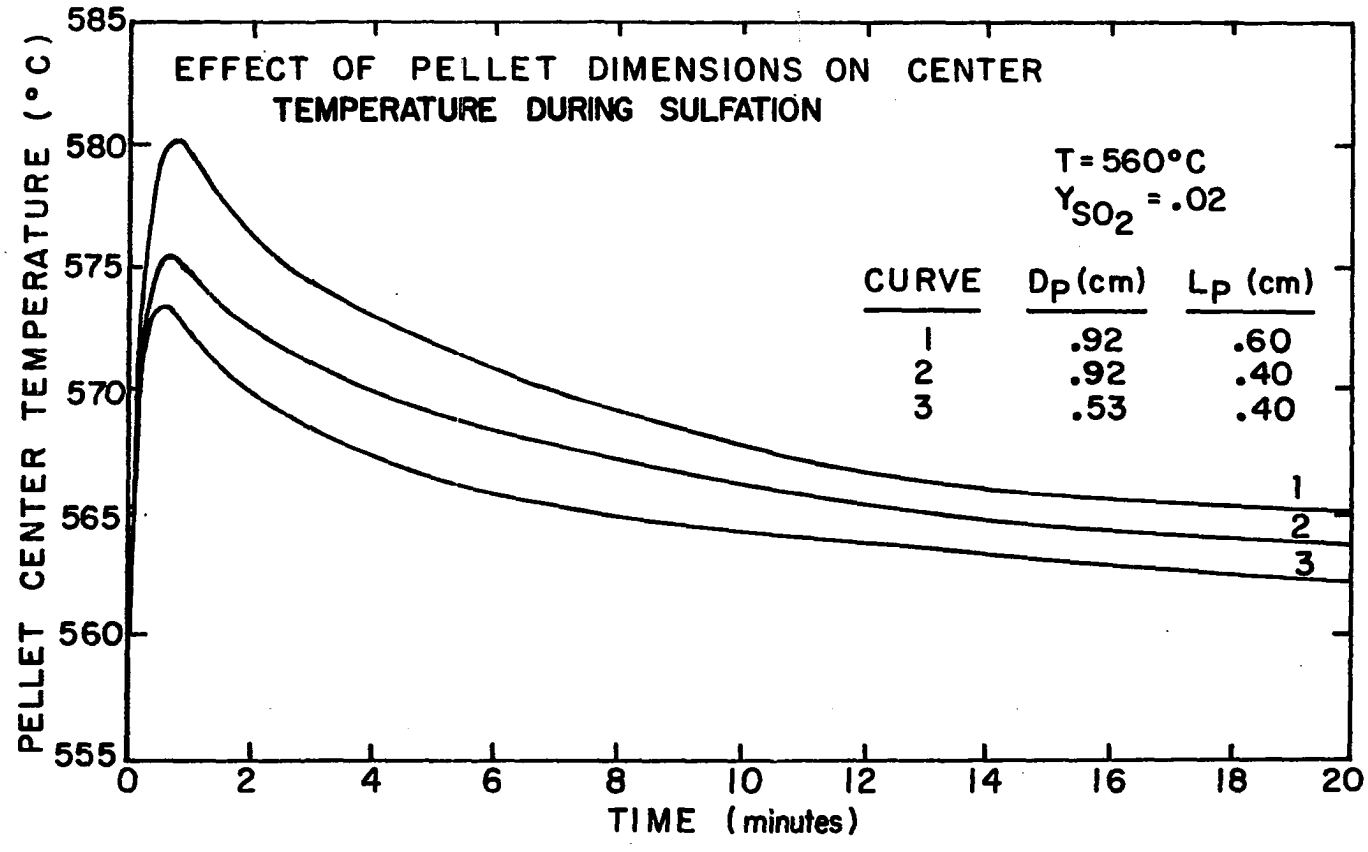

Figure 33. Effect of pellet size on center temperature, during reaction

Table 9. Pellet temperature measurements

Diameter (cm)	Length (cm)	Gas temperature (initial pellet temperature) (^{o}C)	Maximum temperature at pellet center (^{o}C)	ΔT_{max} (^{o}C)	$t_{T_{max}}$ (min)
.92	.60	560	580.2	20.2	.80
.92	.40	560	576.8	16.8	.60
.53	.40	560	574.4	14.4	.52

pellet, and the maximum difference in temperature between the gas and the pellet, ΔT_{max}, decreased for a decreasing radius or a decreasing length. Also shown in Table 9 is the time at which the maximum center temperature, $t_{T_{max}}$, occurred for each pellet. This quantity also decreased for a decreasing radius or a decreasing length.

The pellets used in most of this work were all 0.92 cm in diameter and 0.09 cm in length, which is much shorter than those listed in Table 9. For this reason, the difference in temperature between the pellet center and the outside gas is probably quite small. The isothermal assumption seems justified for pellets of these dimensions. As a check of this conclusion, Young [59] included an energy balance in the development of a two-dimensional expanding grain model to account for the effects of a nonuniform temperature distribution. Young [59] found that for the pellets used in this study, the predictions of conversion versus time, at 740^{o}C, by the isothermal and nonisothermal models, were

nearly identical. Thus, the pellets used in this work may be considered isothermal during reaction.

I. Effect of Reaction on Pellet Surface Area

Surface area measurements were made for pellets reacted at various temperatures and varying periods of time. After a selected period of reaction time, the reaction was terminated and the pellet was transferred to a BET flask. The adsorbate gas used for these surface area measurements was krypton, which made it possible to obtain accurate estimates using only one pellet.

All of the pellets were presintered at 1000°C for five hours, prior to reaction. This was done in an attempt to eliminate the reduction in solid surface area caused by solid reactant sintering. By presintering the solid reactant, the changes in surface area during reaction could be attributed primarily to product layer build-up and product layer sintering.

Table 10 summarizes the results of these experiments for pellets reacted at three different temperatures. Each value reported in Table 10 is from the analysis of a separate pellet. The pellets reacted at a given temperature were all presintered together in the same ceramic boat. This was done in order to obtain pellets with nearly the same initial surface area, prior to reaction at that temperature. As seen from Table 10, the initial specific surface areas of the unreacted pellets ($X = 0$) at each reaction temperature are different. This is probably due to the fact that each group of pellets was presintered individually, and since the electric furnace used for the presintering

Table 10. Pellet surface area measurements

Reaction temperature (°C)	X	Reaction time (min)	A_s (m^2/g)	Normalized A_s (m^2/g)
742	0	0	3.46	3.00
	.030	.4	3.31	2.87
	.054	.8	3.33	2.89
	.098	10	2.83	2.45
	.136	49	2.49	2.16
836	0	0	2.43	3.00
	.109	1.4	2.35	2.90
	.202	6.4	2.10	2.59
	.304	60	1.33	1.64
	.377	86	1.27	1.57
929	0	0	2.96	3.00
	.104	1.0	2.87	2.91
	.202	2.0	2.24	2.27
	.307	10	1.39	1.41
	.444	62	1.06	1.07

did not have a very accurate temperature controller, each group of pellets was probably presintered at slightly different temperatures. Therefore, the unreacted pellets in any given group should have had similar surface areas to other pellets in that group, while pellets from different groups had different initial surface areas.

For any given reaction temperature, the specific surface area of the pellets decreased with increasing reaction time. In order to compare the decreases in surface area among the different reaction temperatures, the surface area values shown in Table 10 were all normalized to correspond to an unreacted pellet surface area of 3.0 m^2/g. This was done by multiplying each surface area value by the ratio of 3.0 m^2/g to the actual unreacted pellet surface area for that group. The results of this mathematical treatment are listed in Table 10. Figure 34 shows a plot of these normalized specific surface areas versus reaction time, for all three reaction temperatures.

All of the curves in Figure 34 have negative slopes because of one or both of the following reasons. Since the reaction is characterized by product layer expansion, the internal void regions inside a pellet will fill up with product, giving rise to a lower internal surface area. In addition, as reaction proceeds, the $CaSO_4$ product, and perhaps the CaO reactant, will undergo sintering, thus reducing the internal surface area. Since the pellets were presintered five hours prior to reaction, sintering of the CaO during reaction was probably not as significant as sintering of the $CaSO_4$.

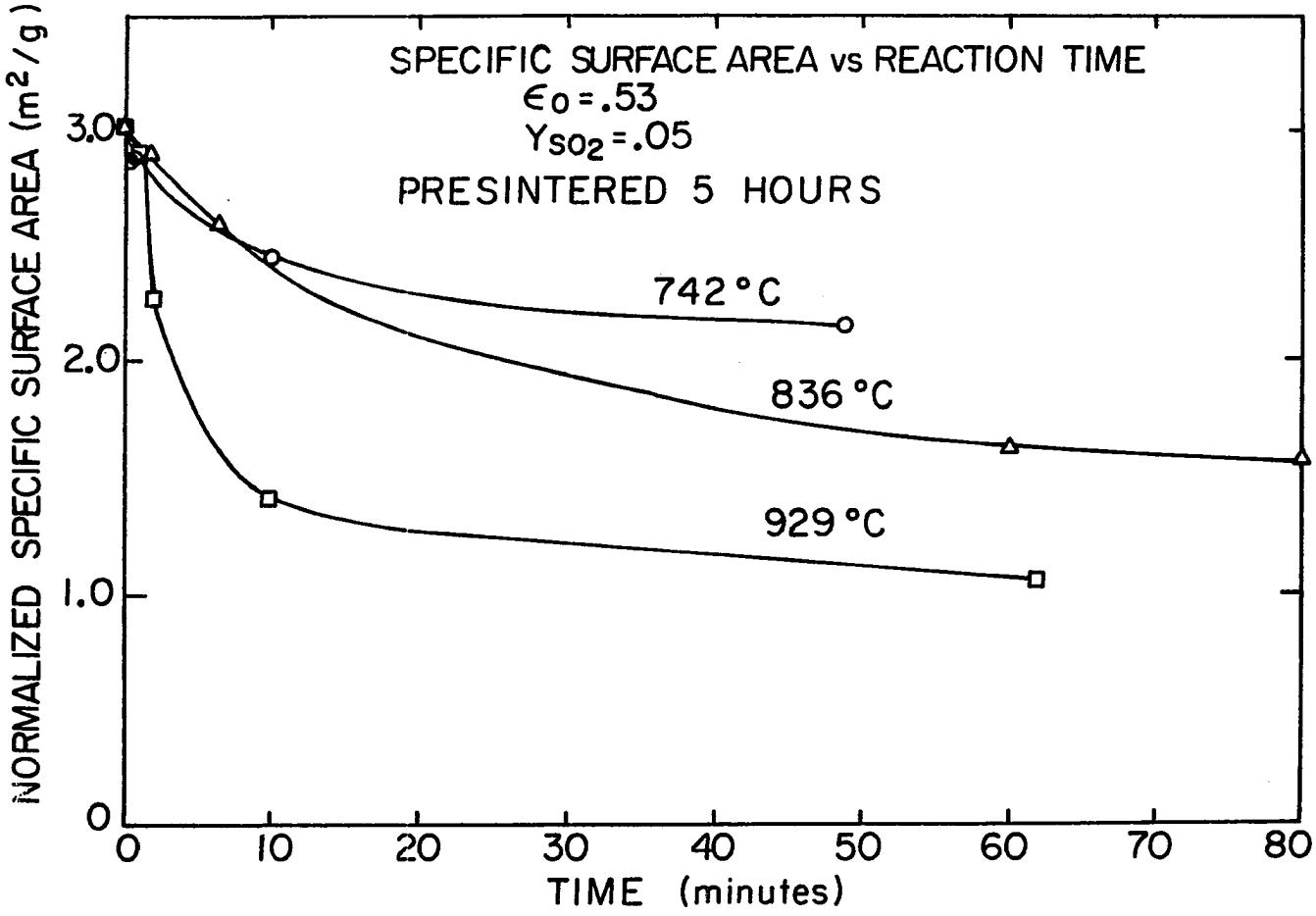

Figure 34. Normalized specific surface area vs reaction time for the sulfation of CaO pellets, presintered at 1000°C for 5 hours

The decreases in specific surface area with reaction time, shown in Figure 34, become larger as reaction temperature increases. One reason for this behavior is that at any fixed reaction time, the conversion level is higher for higher temperatures. Also, the pellets reacted at higher temperatures will be more subject to solid sintering. The combined effects of higher conversion levels and higher rates of sintering, due to temperature increases, result in reductions of surface area, for any given reaction time. The 742°C curve lies below the 836°C curve at early reaction times, but this is not considered a significant effect since it is probably the result of experimental error.

VI. APPLICATION OF EXPANDING GRAIN MODEL

An expanding grain model was applied to the lime sulfation data obtained during this study. It was applied to the conversion-time data from the sulfation of CaO pellets, presintered for varying amounts of time. Since the pellets used in this study were relatively short in length, it seemed appropriate to model them as infinite slabs rather than finite cylinders. This reduced the mathematical treatment from a two-dimensional problem to a one-dimensional problem, and therefore, greatly reduced the complexity of the differential equations describing the system.

Ulrichson and Yake [52] found that under certain conditions, a pellet whose diameter to length ratio is greater than 4 can be described by an infinite slab, if the diffusional resistance is not large. The diameter to length ratio (aspect ratio) of the pellets used in the present study is greater than 8 for all cases. Therefore, the infinite slab assumption was considered appropriate for the present analysis.

A. Development of One-Dimensional Expanding Grain Model

The expanding grain model describes gas-solid reaction systems that are characterized by product layer expansion. A pellet is modeled as a random grouping of dense grains that react according to the shrinking unreacted-core model [33]. The reactant gas diffuses from the bulk gas to the pellet surface, then diffuses between the grains, through the solid product layer around a grain, and finally reacts at the reaction surface.

The general reaction considered is given by Equation (1), with a = 1:

$$A(g) + bB(s) \rightarrow cC(g) + dD(s) \ . \tag{103}$$

The following assumptions are applied to the system:

1. Reacting solid is an infinite slab of thickness, L, with both top and bottom exposed to reactant gas.
2. Pellet retains its initial shape throughout the reaction.
3. Reaction is irreversible and first order in A.
4. Grains and pellet are all isothermal.
5. Grains are spherical.
6. Grain growth is unrestricted (spherical geometry remains the same).
7. Intrapellet effective diffusivity varies with porosity.
8. Pressure is uniform and constant.
9. External mass transfer resistance is negligible.
10. Effect of sintering is negligible.

The molar flux of species A in a binary mixture is given by [48]

$$N_A = -D_{Ae} C_T \nabla Y_A + Y_A \delta_A (N_A + N_C) \tag{104}$$

where

$$\delta_A = \frac{D_{Ae}}{D_{AC}\, \epsilon^2} \ , \tag{105}$$

$$N_C = - cN_A \text{ (from stoichiometry)} \ . \tag{106}$$

The viscous flow term in Equation (104) has been neglected since the pressure was assumed uniform and constant.

Writing a mass balance around a small element within the slab leads to the following:

$$-\frac{\partial N_A}{\partial z} - \bar{R}_A = \frac{\partial C_A}{\partial t}\,\epsilon \tag{107}$$

where

z = length coordinate, and

$\bar{R}_A$ = reaction rate per unit pellet volume.

Solving for N_A from Equation (104), using Equation (106), and substitution of the result into Equation (107) yields

$$\frac{\partial}{\partial z}\left(\frac{D_{Ae} C_T \nabla Y_A}{1 - (1 - c)\, Y_A \delta_A}\right) - \bar{R}_A = \frac{\partial C_A}{\partial t}\,\epsilon\ . \tag{108}$$

Applying the chain rate to Equation (108) and then rearranging leads to

$$\frac{\partial^2 Y_A}{\partial z^2} + \frac{\partial Y_A}{\partial z}\left[\frac{1}{D_{Ae}}\frac{\partial D_{Ae}}{\partial z} + \frac{M\delta_A}{1 - MY_A\delta_A}\frac{\partial Y_A}{\partial z} + \frac{MY_A}{1 - MY_A\delta_A}\frac{\partial \delta_A}{\partial z}\right]$$

$$-\frac{1 - MY_A\delta_A}{C_T D_{Ae}}\bar{R}_A = \frac{1 - MY_A\delta_A}{D_{Ae}}\frac{\partial Y_A}{\partial t}\,\epsilon \tag{109}$$

where $M = 1 - c$. Equation (109) represents the intrapellet (intergrain), continuity equation for gaseous reactant A, and has the following boundary and initial conditions:

$$\text{at } z = 0, \frac{\partial Y_A}{\partial z} = \frac{\partial D_{Ae}}{\partial z} = \frac{\partial \delta_A}{\partial z} = 0 \ , \tag{110}$$

$$\text{at } z = L/2, \ Y_A = Y_{Ab} \ , \tag{111}$$

$$\text{and at } t = 0, \ Y_A = 0 \ . \tag{112}$$

The three boundary conditions listed in Equation (110) arise from the symmetry of the slab (Figure 35). Boundary condition 111 comes from the assumption of negligible external mass transfer resistance. Initial condition 112 states that, initially, there is no A present in the pellet.

The chemical reaction rate per unit pellet volume, $\bar{R}_A$, is related to the rate per grain unit area, R_{A_c}, by Equation (21):

$$\bar{R}_A = \frac{3(1 - \epsilon_o) r_c^{\,2}}{r_{go}^{\,3}} R_{Ac} \tag{21}$$

$$= \frac{3(1 - \epsilon_o) r_c^{\,2}}{r_{go}^{\,3}} k \, C_T \, Y_{Ac} \ . \tag{113}$$

In analogy to Equation (104), the following flux relationship was applied to A moving through the product layer around the grains:

$$N_A = - D_{As} C_T \nabla Y_{Ag} + Y_{Ag} \, \delta_{SA} \, (N_A + N_c) \tag{114}$$

where

Y_{Ag} = intragrain mole fraction of A,

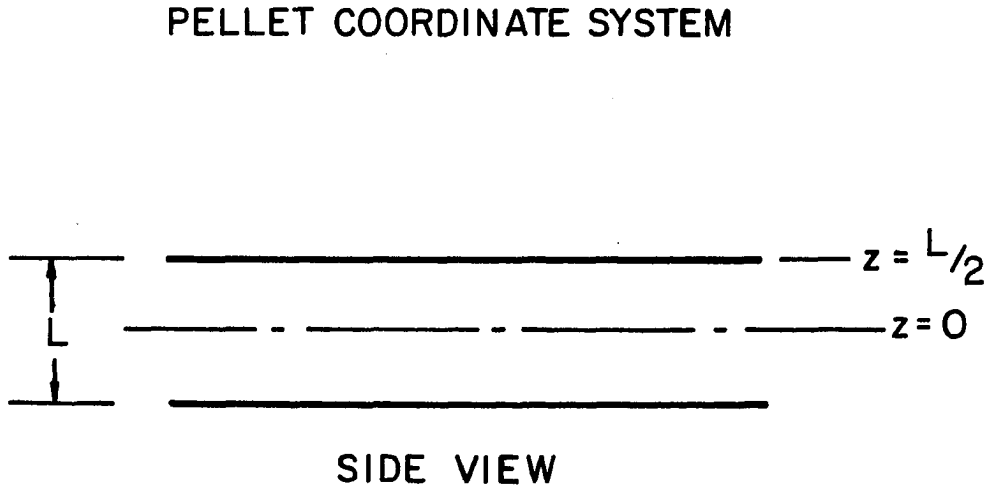

Figure 35. Infinite slab coordinate system

δ_{SA} = intragrain factor = D_{As}/D_{ACe} , and

D_{ACe} = effective binary diffusivity in product layer.

A mass balance written on a small element within the product layer around a grain gives

$$\frac{d}{dr}\,(r^2 N_A) = 0 \ . \tag{115}$$

Solving for N_A from Equation (114) and substitution into Equation (115) gives the following intragrain continuity equation:

$$\frac{d}{dr}\left(\frac{r^2 D_{As}}{1 - MY_{Ag}\delta_{SA}}\,\frac{dY_{Ag}}{dr}\right) = 0 \tag{116}$$

with the boundary conditions

$$\text{at } r = r_g,\ Y_{Ag} = Y_A \tag{117}$$

$$\text{and at } r = r_c,\ \left[\frac{D_{As}C_T}{1 - MY_{Ag}\delta_{SA}}\,\frac{dY_{Ag}}{dr}\right]_{r_c} = kC_T Y_{Ac} \ . \tag{118}$$

Boundary condition 117 says the mole fraction of A at the surface of the grain is equal to that in the void region surrounding the grain. Boundary condition 118 equates the flux of A at the reaction interface to the consumption rate. The analytical solution is

$$\frac{1 - MY_{Ac}\delta_{SA}}{1 - MY_A\delta_{SA}} = \exp\left[\frac{M\delta_{SA}kY_{Ac}}{D_{As}}\left(r_c - \frac{r_c^2}{r_g}\right)\right] \ . \tag{119}$$

In order to complete the set of equations presented thus far, it is necessary to account for the parameters that will vary during reaction. These parameters have been discussed previously in the text, but will be repeated here for continuity. As reaction proceeds, the grains will expand according to

$$r_g = r_{go} [1 + (Z_E - 1)X] \tag{25}$$

where

$$X = \text{Local conversion} = 1 - \left(\frac{r_c}{r_{go}}\right)^3 . \tag{120}$$

Expansion of the grains will cause the local porosity to decrease by the following:

$$\epsilon = \epsilon_o - (1 - \epsilon_o)(Z_E - 1)X . \tag{49}$$

This decrease in local porosity will then cause a decrease in the local intrapellet effective diffusivity, D_{Ae}:

$$D_{Ae} = \frac{1}{\frac{1}{D_{KA}} + \frac{1}{D_{AC}\epsilon^2}} . \tag{26}$$

A mass balance for solid reactant, B, written around a grain, gives

$$\rho_B \frac{dr_c}{dt} = kC_T Y_{Ac} . \tag{121}$$

By integrating Equation (121) over a small time step, Δt, where the value of Y_{Ac} remains relatively constant, one can obtain an estimate of

the new reaction interface position, as follows:

$$r_c\Big|_{t+\Delta t} = r_c\Big|_t - \Delta t \frac{kC_T Y_{Ac}}{\rho_B} \quad . \tag{122}$$

B. Method of Solution

The equations written for the one-dimensional expanding grain model were solved numerically using a digital computer. The intrapellet concentration profile was found by solving Equations (109) to (112) using an implicit finite difference technique. Even though pseudo-steady state is usually assumed in most gas-solid reactions, the unsteady state form of Equation (109) was used to prevent instability and convergence problems [52, 58]. Small pseudo-time steps were taken using Equation (109) until pseudo-steady state was reached. It should be noted that the pseudo-time step used in finding Y_A was much smaller than the time step used to increment t.

Once the values of Y_A were known throughout the pellet, the corresponding reaction interface concentrations, Y_{Ac}, were calculated by solving Equation (119) using the Regula-Falsi method [11]. New values were then found for r_c using Equation (122), X using Equation (120), r_g using Equation (25), ϵ using Equation (49), D_{Ae} using Equation (26), and δ_A using Equation (105). The overall pellet conversion, X_p, was then calculated by numerically integrating X over the pellet volume:

$$X_p = \frac{2}{L} \int_o^{L/2} X dz \quad . \tag{123}$$

This calculation cycle was then repeated when the next time step was taken. A listing of the computer program used to solve these equations is given in Appendix A.

For Reaction 60, c = -0.5 since one-half mole of oxygen reacts for every mole of SO_2 and there is no product gas. However, since the concentrations of SO_2 used in the model were quite small, c had a negligible effect on the model predictions. For this reason, c was assigned a value of 1.0 to simplify the calculations. This is equivalent to assuming equimolar counterdiffusion.

C. Comparison of One-Dimensional and Two-Dimensional Models

To determine whether or not the assumption of slab-like geometry was good, the predictions of the one-dimensional expanding grain model were compared to the predictions of a two-dimensional model, where the pellet is assumed cylindrical. Young [59] developed an expanding grain model for a cylindrical pellet using the same basic assumptions as those used in the present model. The only major difference between the two models is the incorporation of radial diffusion in Young's model.

The dimensions of a typical pellet (0.880 cm diameter, 0.095 cm length) were used to test the accuracy of the one-dimensional model. Using typical parameters, the conversion-time predictions from both models were found virtually identical. The maximum difference in predicted conversion was only 1.2%, which occurred at a reaction time of 0.5 minutes.

From the comparison of these two models, it was concluded that the infinite slab assumption was accurate for the pellets used in this study.

Apparently, the effect of radial diffusion on the conversion-time behavior is negligible for pellets of these dimensions (0.880 cm diameter, 0.095 cm length).

D. Application of Model to Lime Sulfation Data

In order to test the ability of the model to describe the lime sulfation reaction system, model predictions were compared to the experimental conversion-time data obtained in this study. Since values for the molar volume of $CaSO_3$ could not be found, the model was only compared to reaction data at 742°C or above, where it was shown little or no $CaSO_3$ is produced. Overall, it was found that the model predicts the conversion data very well for highly presintered CaO pellets. However, the accuracy of the model becomes worse as the pellet presintering time decreases. These observations may illustrate the importance of two features the model does not consider. First, the model does not consider solid sintering, which reduces the surface area available for reaction and therefore, reduces the reaction rate. Second, grains of CaO produced by calcining $Ca(OH)_2$ contain a micropore structure, which violates the model assumption of dense, nonporous grains. Presintering the pellets prior to reaction will tend to minimize the effect of these two phenomena on the reaction, and therefore, improve the model accuracy.

Figure 36 shows the conversion-time data for the sulfation of a CaO pellet, presintered at 1000°C for 5 hours. The reaction was performed at 836°C in 5% SO_2, 20% O_2, and the balance N_2. Table 11 lists some of the model parameters used to produce the conversion-time curve shown in

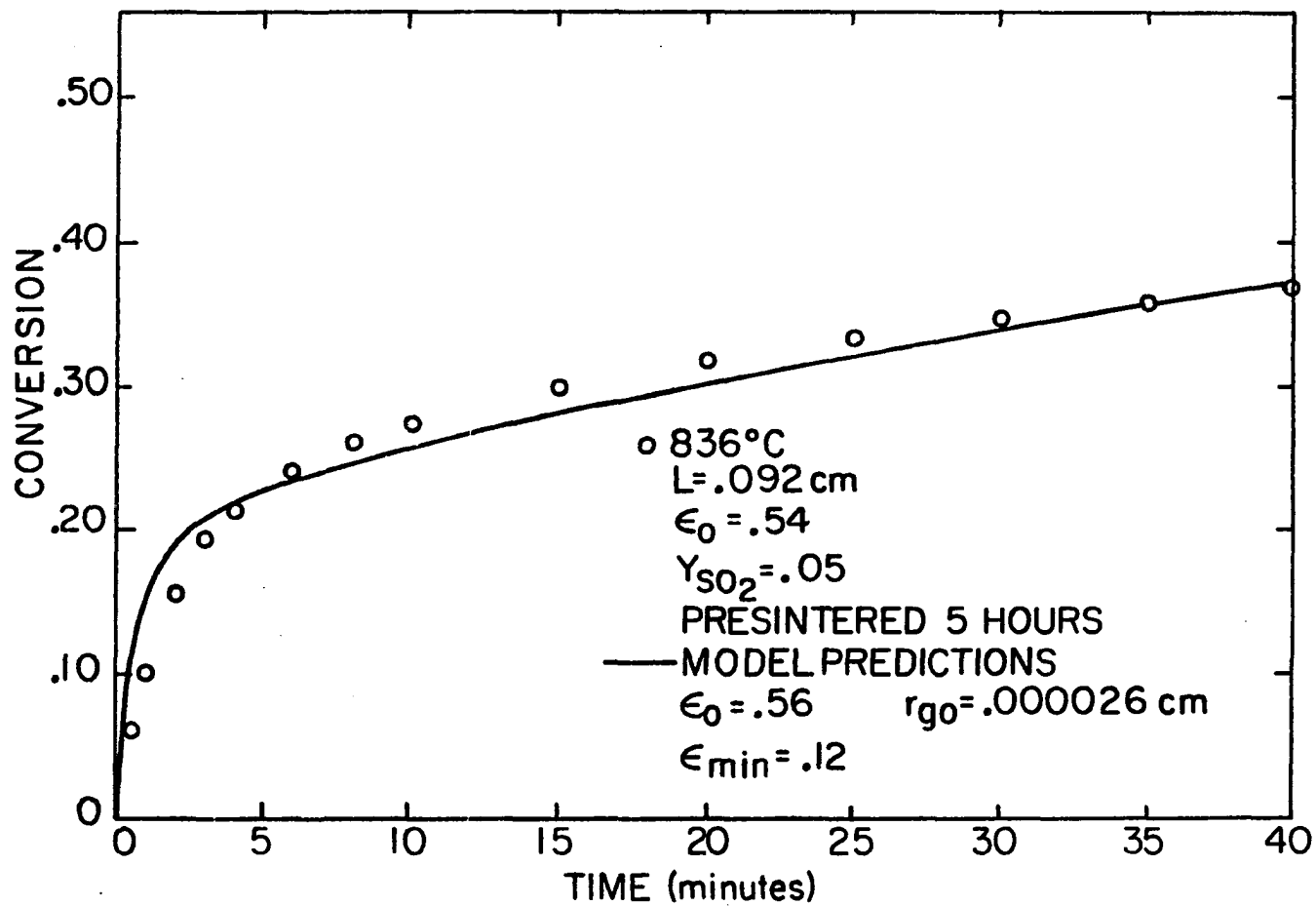

Figure 36. Comparison of model predictions to experimental data from the sulfation of CaO pellets, presintered at 1000°C for 5 hours

Table 11. Experimental data and model parameters used in Figure 36

Experimental data:

$T = 836^{o}C$	$k = 0.077$ cm/sec
$L = 0.092$ cm	$D_{As} = 10.7 \times 10^{-8}$ cm^2/sec
$\epsilon_o = 0.54$	$Z_E = 3.05$
$Y_{SO_2} = 0.05$	
$Y_{O_2} = 0.20$	
$Y_{N_2} = 0.75$	

Model parameters:

$\epsilon_o = 0.56$

$\epsilon_{min} = 0.12$

$r_{go} = 0.26 \times 10^{-4}$ cm

$D_{AC} = 1.22$ cm^2/sec

$D_{KA} = 8.11$ cm^2/sec

$\delta_{SA} = 1.0$

$Y_{Ab} = 0.05$

Figure 36. In general, the model fit is good, with the model slightly overestimating conversion at early reaction time and underestimating conversion at later times. The value for the initial grain radius used in the model was determined using Equation (90) and the experimentally measured value of initial specific surface area, from Table 8. The initial porosity used in the model ($\epsilon_o = 0.56$) is slightly higher than that measured experimentally ($\epsilon_o = 0.54$), but well within the range of experimental error. Experimental initial porosity estimates were made by simply measuring the exterior dimensions of the pellet using a micrometer, and then using

$$\epsilon_o = 1 - \frac{\rho'_{pellet}}{\rho'_{CaO}}$$

$$= 1 - .384 \frac{\text{pellet mass}}{D^2 L} \qquad (124)$$

where the pellet mass is in units of grams and the pellet diameter, D, and length, L, are in units of centimeters.

In order to improve the fit of the model, it was necessary to introduce a minimum porosity parameter, ϵ_{min}. Without this parameter, the model tended to greatly overestimate the conversion levels at late reaction times. Theoretically, minimum porosity accounts for the fact that most of the pellets do not react to their maximum possible conversion level. This may be due to local blockages of passageways within the pellet, which prevent SO_2 from reaching certain unreacted areas within the pellet. A minimum porosity value of 0.12 was found to best fit the data shown in Figure 36. In the model, once a given pellet location

has reached the minimum porosity, the reaction at that location ceases, while the reaction deeper inside the pellet continues.

Figure 37 shows conversion-time data for a pellet presintered at 1000°C for only 30 minutes. The reaction was carried out at 836°C, in 5% SO_2. Some of the parameters used for the model curve in Figure 37 are listed in Table 12. In this case, both the minimum porosity and initial grain radius were adjusted to obtain the best fit. Using the value of initial grain radius derived from the initial specific surface area and Equation (90) (0.000015 cm), the model seriously underestimated conversion at all reaction times. However, using the adjusted value listed in Table 12 (0.000030 cm), the model fit was greatly improved, as shown in Figure 37.

1. Effect of temperature

The reaction temperature is an important model parameter as it affects the values of the reaction rate constant, solid-state diffusivity, effective diffusivity, and total gas concentration. Figure 38 shows the effect of reaction temperature on the model predictions of conversion versus time for pellets presintered at 1000°C for 24 hours. The experimental data are those from Figure 32. The initial grain radius was adjusted to provide a good fit of the 836°C data, and was then held at that value for the 929° and 742°C curves. Good agreement between the model and experimental data is observed at 836° and 742°C. However, the model underestimates the conversion levels at 929°C.

It was unnecessary to introduce a minimum porosity into the model in order to obtain a good fit of the data in Figure 38. This is because the

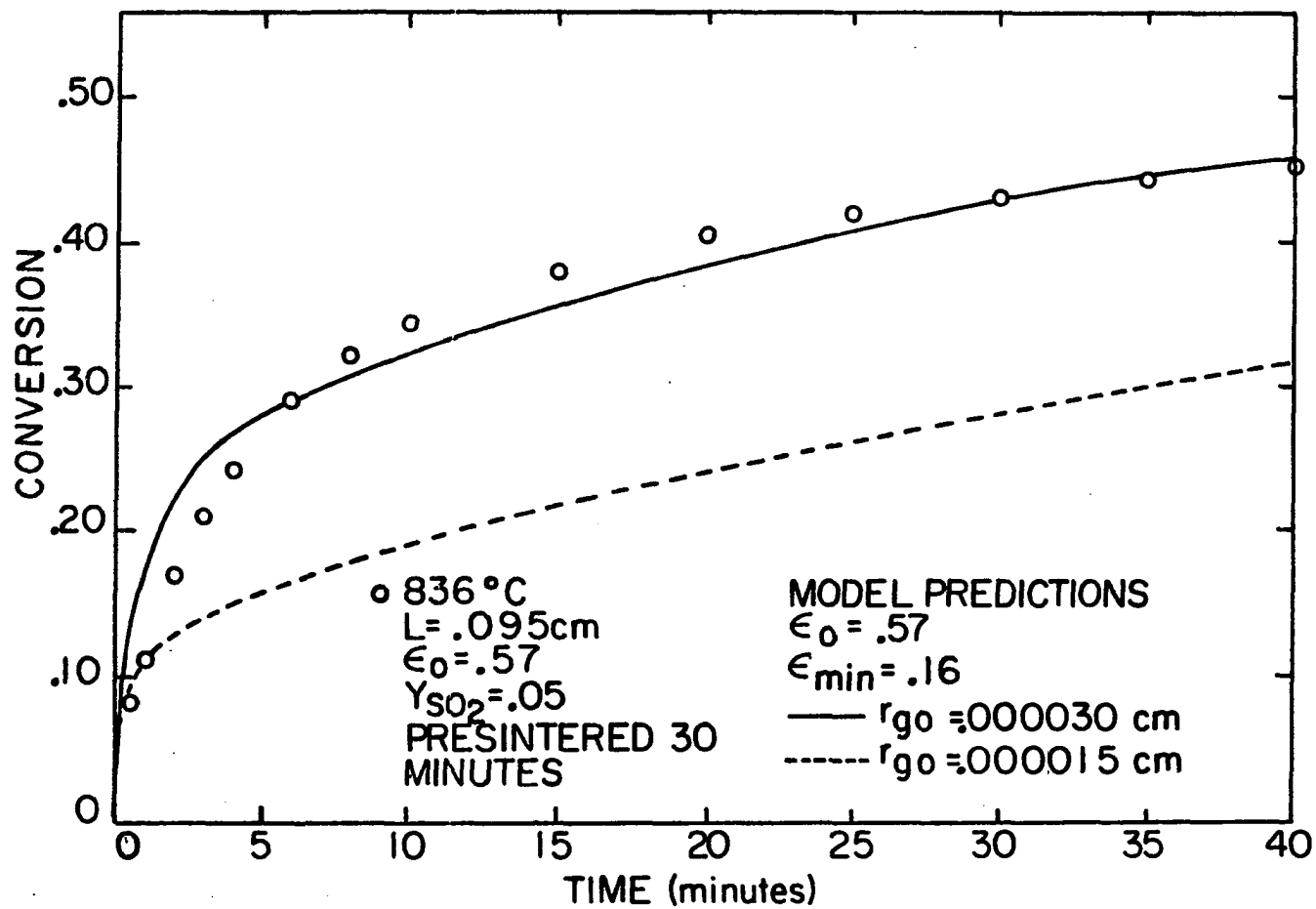

Figure 37. Comparison of model predictions to experimental data from the sulfation of CaO pellets, presintered at 1000°C for 30 minutes

Table 12. Experimental data and model parameters used in Figure 37

Experimental data:

$T = 836^{o}C$	$k = 0.077$ cm/sec
$L = 0.095$ cm	$D_{As} = 10.7 \times 10^{-8}$ cm^2/sec
$\epsilon_o = 0.57$	$Z_E = 3.05$
$Y_{SO_2} = 0.05$	
$Y_{O_2} = 0.20$	
$Y_{N_2} = 0.75$	

Model parameters:

$\epsilon_o = 0.57$

$\epsilon_{min} = 0.16$

$r_{go} = 0.30 \times 10^{-4}$, or 0.15×10^{-4} cm

$D_{AC} = 1.22$ cm^2/sec

$D_{KA} = 8.11$ cm^2/sec

$\delta_{SA} = 1.0$

$Y_{Ab} = 0.05$

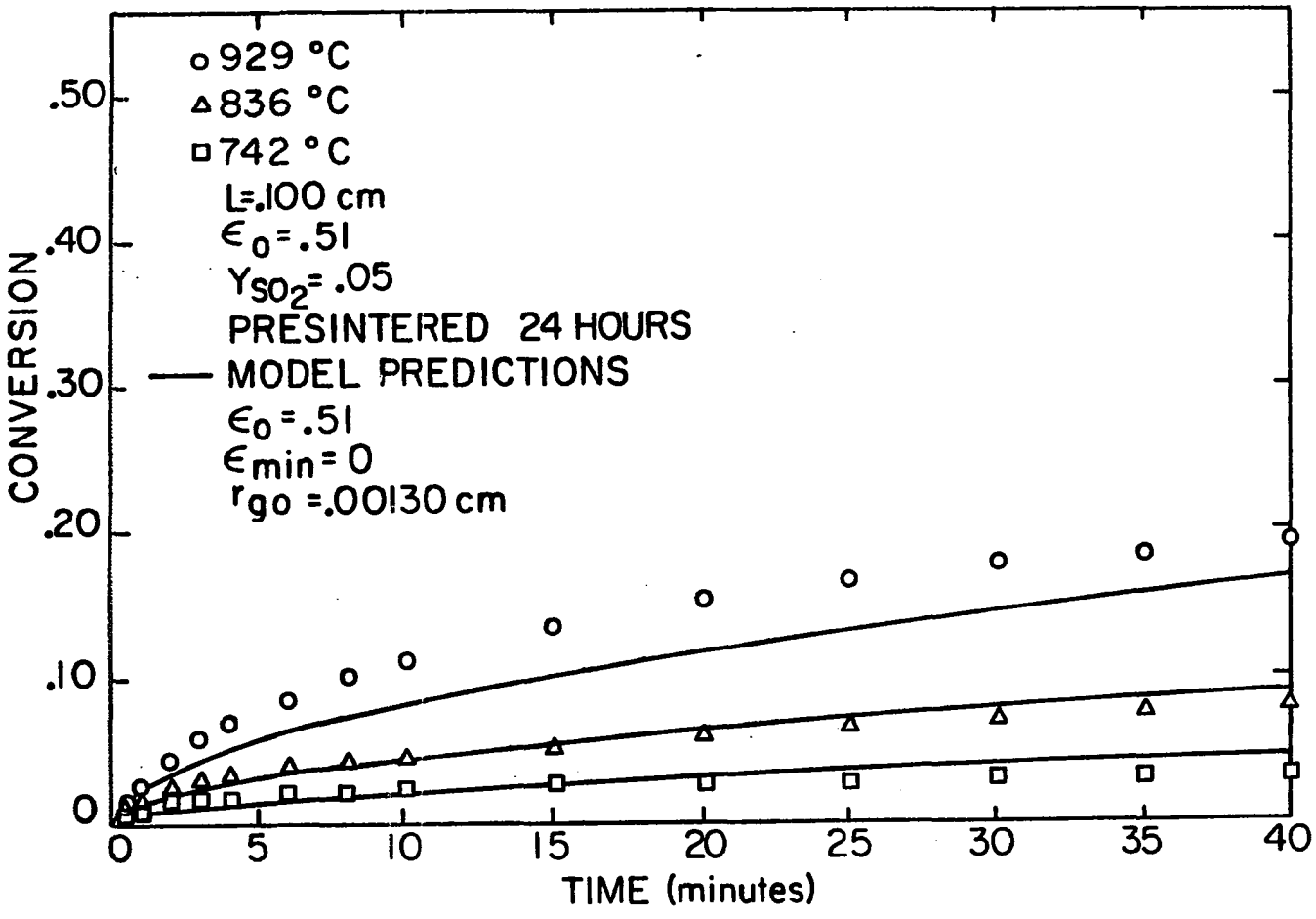

Figure 38. The effect of temperature on the conversion-time behavior of the sulfation of CaO pellets, presintered at 1000°C for 24 hours

initial grain radius used was quite large, which caused the simulated reaction to become product layer diffusion controlled at low conversion levels, as evidenced by a fairly uniform intrapellet SO_2 concentration. Therefore, the reaction was relatively homogeneous and occurred at a slow rate, making it unnecessary to introduce a minimum porosity to shut down the reaction. Table 13 shows a list of parameters used to model the data in Figure 38. The initial grain radius used in the model (0.00130 cm) is much larger than that found from the initial specific surface area measurement (0.00007 cm). However, scanning electron micrographs have shown grains as large as 9 microns (0.0009 cm) in pellets that have been sintered for 24 hours at 1000°C.

Figure 39 shows the effect of temperature on pellets that were presintered at 1000°C for only 30 minutes. The model curve at 836°C represents the best fit curve from Figure 37, and the 929°C curve was computed using the same structural parameters, changing only those parameters dependent on temperature. The model predictions at 929°C match the experimental data fairly well, except at late reaction times where the model significantly overestimates the conversion-time data. An explanation for this overestimation is that a significant amount of solid sintering may be occurring at 929°C, which the model does not account for.

Even though the model does not fit the experimental data as well as one might desire, it is important to note how it does predict general trends in the data at different temperatures. Figure 38 shows the conversion data at 929°C lying above the 836°C data, while Figure 39 shows

Table 13. Experimental data and model parameters used in Figure 38

Experimental data:

$L = 0.100$ cm

$\epsilon_o = 0.51$

$Y_{SO_2} = 0.05$

$Y_{O_2} = 0.20$

$Y_{N_2} = 0.75$

$Z_E = 3.05$

	742°C	836°C	929°C
k =	0.034 cm/sec	0.077 cm/sec	0.150 cm/sec
D_{As} =	2.4×10^{-8} cm^2/sec	10.7×10^{-8} cm^2/sec	38.5×10^{-8} cm^2/sec

Model parameters:

$\epsilon_o = 0.51$

$\epsilon_{min} = 0$

$r_{go} = 13 \times 10^{-4}$ cm

$\delta_{SA} = 1.0$

$Y_{Ab} = 0.05$

	742°C	836°C	929°C
D_{AC} =	1.07 cm^2/sec	1.22 cm^2/sec	1.38 cm^2/sec
D_{KA} =	7.76 cm^2/sec	8.11 cm^2/sec	8.96 cm^2/sec

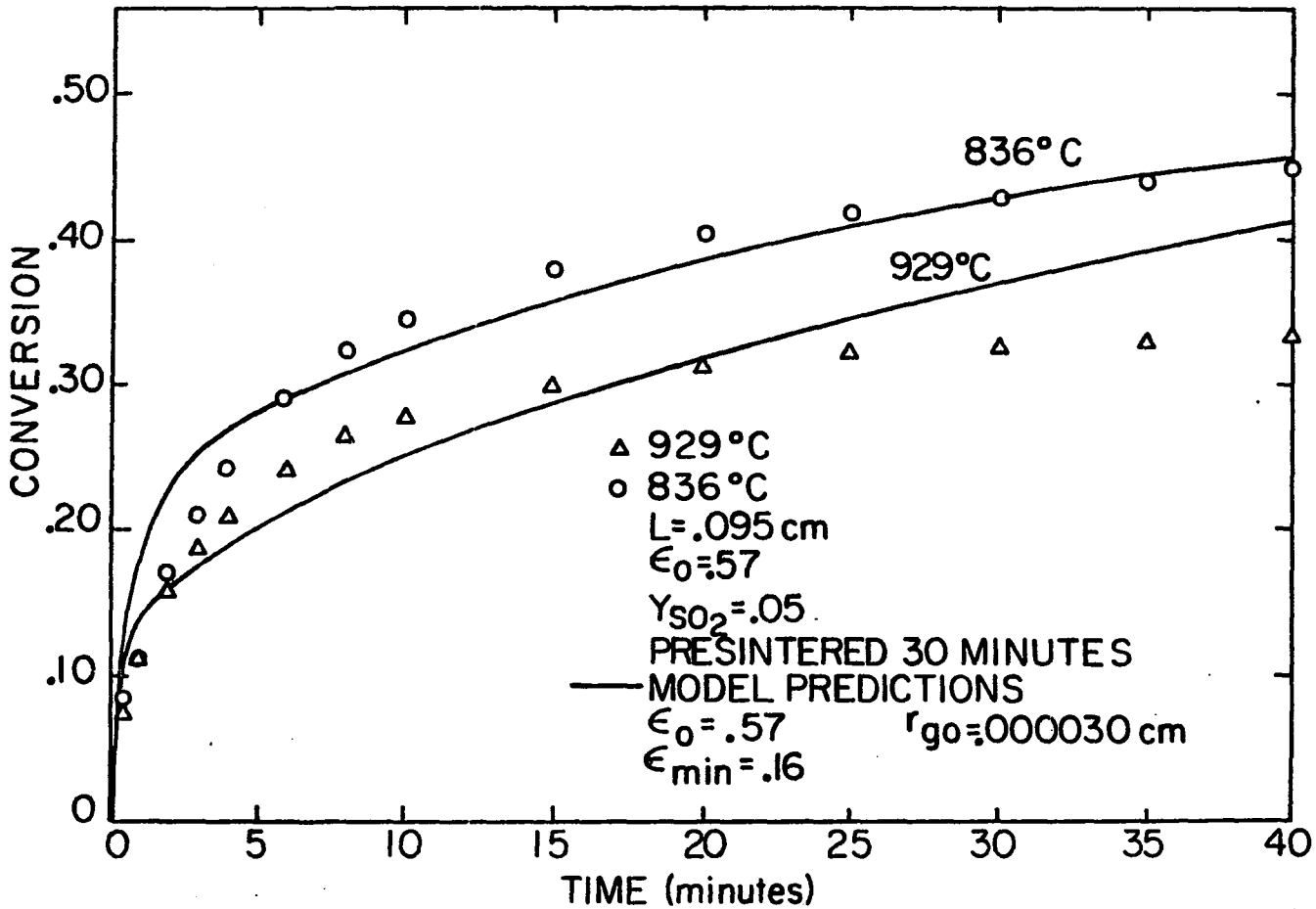

Figure 39. The effect of temperature on the conversion-time behavior of the sulfation of CaO pellets, presintered at 1000°C for 30 minutes

the 929°C data lying below the 836°C data. In both cases, the model correctly predicts these trends, which may help us to explain the shift in the relative position of the data. The largest difference in model parameters used to simulate these two sets of data was the value of initial grain radius. For the data on pellets presintered 30 minutes, r_{go} was assumed to be 0.3 μm, while the data on pellets presintered 24 hours were fit with a value of r_{go} equal to 13.0 μm. This large deviation in grain sizes supports the conclusion that the optimum reaction temperature is largely dependent on the initial grain size of the solid.

2. Effect of initial grain size

Figures 40 and 41 show model predictions at 929° and 836°C for a variety of initial grain radii. The other parameters used in the model were assigned typical values. Some of the curves exhibit a relatively sharp break in their slope at late reaction time due to the use of a minimum porosity of 0.16, which was used in order to be consistent with the previous modeling efforts.

In Figure 40, as r_{go} increases from 0.2 μm to 0.6 μm, the model curves at both temperatures tend to increase at all reaction times. However, Figure 41 shows that increasing r_{go} from 2 μm to 4 μm causes the conversion curves to decrease. This suggests that a maximum conversion curve exists and occurs at some optimum value of r_{go}. Local conversion optimums are also observed in the experimental data shown in Table 8, where the conversion levels attained after 40 minutes of reaction, at either 836° or 929°C, go through a maximum with varying presintering time, and thus, r_{go}.

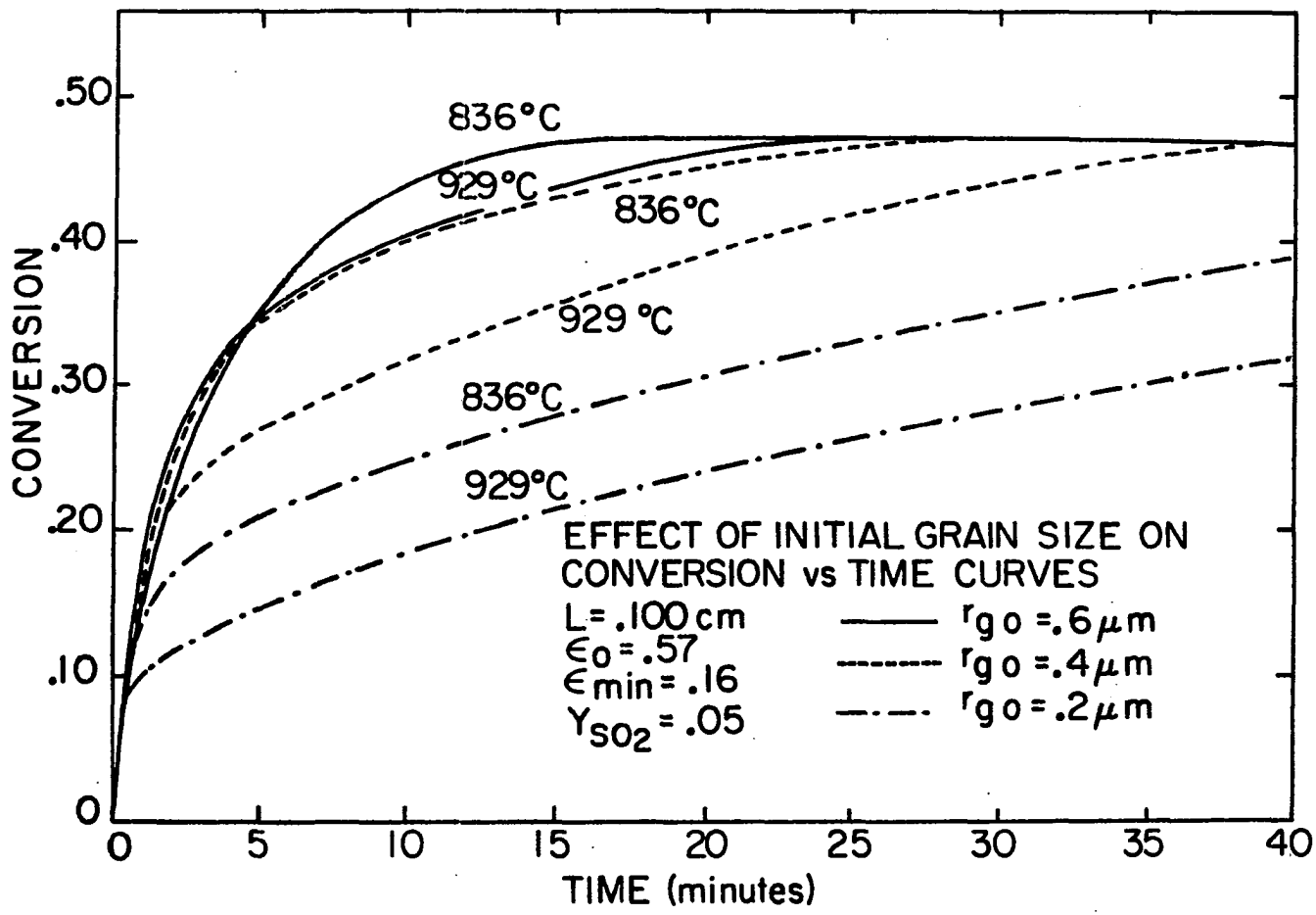

Figure 40. The effect of initial grain size on the model predictions

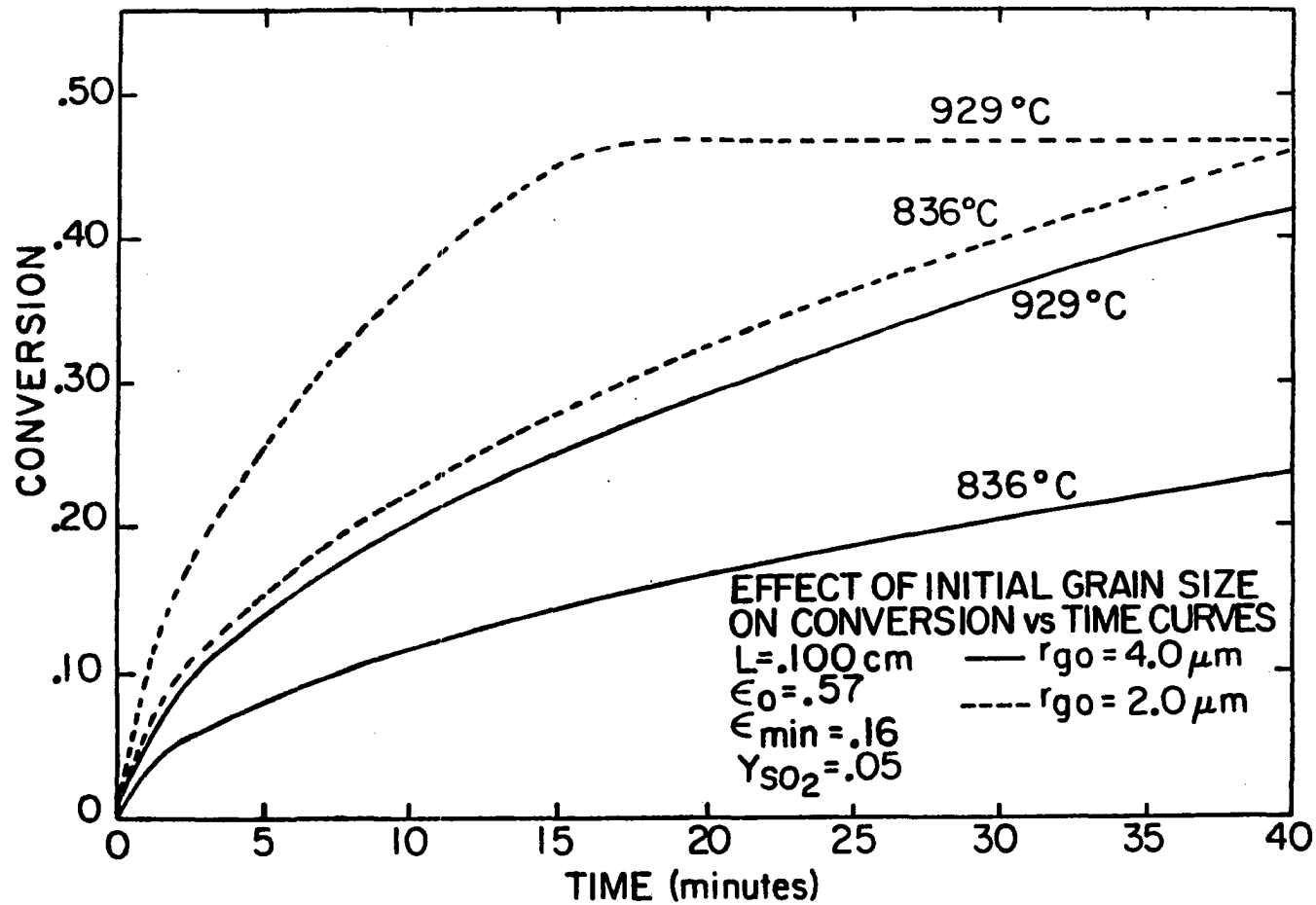

Figure 41. The effect of initial grain size on the model predictions

In the model, the value of r_{go} for which the conversion behavior is optimum is different for each reaction temperature. Figure 40 and 41 demonstrate that, with increasing r_{go}, the 929°C curve approaches the 836°C curve and eventually lies above it at large values of r_{go}. Therefore, the optimum r_{go} for the 929°C reaction is higher than that of the 836°C reaction. Table 8 shows that the experimental data at 929° and 836°C exhibit the same behavior. The optimum presintering time is higher for the 929°C data (5 hours) than it is for the 836°C data (30 minutes).

This similarity in behavior between the model predictions and experimental data can also be seen by comparing the model curves for r_{go} = 0.4, 0.6, and 2.0 μm, shown in Figures 40 and 41, to the experimental curves for 929° and 836°C, shown in Figures 29, 30, and 31, respectively. The 836°C curve starts out on top, the curves then become close to each other, and then the 929°C curve becomes higher than the 836°C curve, as r_{go} increases. By this comparison, it is not suggested that the values of r_{go} used in the model correspond exactly to the average initial grain radii of the different pellets. Rather, it shows that the model correctly predicts the effect of initial grain radius on the reaction.

It might be argued that some of the effects of presintering time on the conversion-time behavior of the pellets are not solely due to changes in the initial grain radius. Table 8 shows that initial porosity decreases with increasing presintering time, and it is known that the reaction is influenced by this parameter. Figures 26 and 27 show that decreasing the initial porosity, holding all other parameters constant,

results in a decrease in the experimental optimum temperature. However, the conversion data in Table 8 show that as initial porosity decreases, the optimum temperature increases, suggesting that the increase in grain radius that accompanies the decrease in initial porosity in Table 8, has an overwhelming effect on the conversion behavior. Therefore, it is probably safe to conclude that the major influence on the conversion data at any given temperature, shown in Figures 29-32 and summarized in Table 8, is that of the changing initial grain radius.

3. Effect of grain size distribution

From scanning electron micrographs of cross-sectioned pellets, it is apparent that the CaO grains have a significant size distribution. For this reason, it was considered important to determine the effects of a grain size distribution on the model predictions. Up to now, the model estimates were made using a uniform initial grain radius, r_{go}, so the possibility of improving the model fit, by accounting for the distribution of grain sizes, was considered.

A grain size distribution was incorporated into the one-dimensional expanding grain model, developed previously, by specifying several initial grain radii with a given mass fraction associated with each initial grain radius. The reaction interface mole fraction, Y_{Ac}, was calculated individually for each grain size and the reaction front movement, and thus conversion, was also found for each grain size. At any given pellet location, the conversion levels for all of the grain sizes were summed to determine an average local conversion level, which was then averaged throughout the pellet to determine the overall pellet conversion. The

average local conversion was used to calculate a new value of local porosity, which was then used to determine a new value of the local effective diffusivity, D_{Ae}. A new intrapellet concentration profile was then calculated using a mass average grain radius at any given pellet location. Appendix B contains the computer program for this model.

To evaluate the magnitude of the effect of a grain size distribution on the model predictions, several size distributions were introduced into the model. Each distribution had a mass average initial grain radius of 0.3 μm. The reaction was simulated at 836°C, using typical model parameters. A summary of the model predictions is shown in Figure 42.

Curve 1 in Figure 42 represents a pellet consisting of uniform grains, all having an initial radius of 0.3 μm. Curves 2-5 are the model predictions for pellets made up of grains with broadening size distributions. As the grain size distribution widens, the model predicts smaller conversion levels at any given reaction time. Similar behavior was noted by Szekely and Propster [50], who studied the effects of three distribution functions (Gates-Gaudin-Schuhman, log-normal, and normal) on the predictions of the simplified grain model.

From Figure 42, we can conclude that a grain size distribution does have a significant effect on the model predictions. However, by comparing the 836°C curves for r_{go} = 0.2 and 0.4 μm in Figure 40 to the group of curves shown in Figure 42, it appears that the conversion predictions may be more sensitive to average initial grain size than to the grain size distribution. For this reason, and because of the uncertainty involved in experimentally determining an average initial grain size, it was

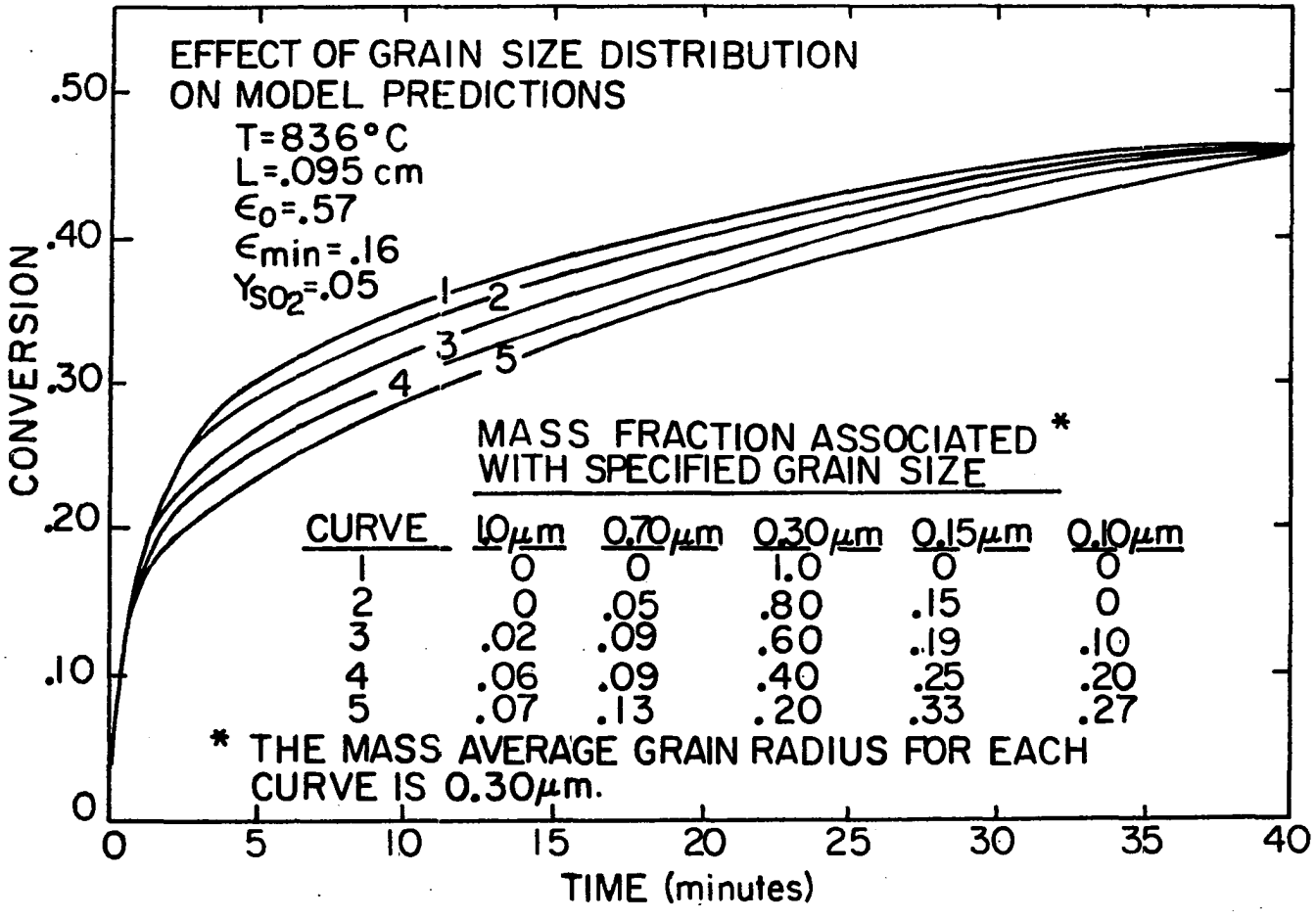

Figure 42. The effect of a grain size distribution on the model predictions

considered inappropriate to try to improve the model predictions by including a grain size distribution at this time. If the size distribution effects were greater, or if accurate and reproducible estimates of the average initial grain size could be obtained for CaO produced from $Ca(OH)_2$, it would then be important to try to include an experimentally determined grain size distribution into the model.

4. Effect of solid-state diffusivity

The grain model assumes the grains are nonporous and react according to the shrinking unreacted-core model. In reality, grains of CaO, produced by calcining $Ca(OH)_2$, have been found to contain micropores of radii as small as 18 Å. These micropores probably allow the SO_2 to diffuse into the interior regions of the grain at faster rates than solid-state diffusion alone. However, for pellets that have been presintered for long periods of time, the micropore structure within the grains probably disappears, making the assumption of nonporous grains more accurate.

Since the experimental values of solid-state diffusivity were determined using highly sintered CaO, which should have had no significant micropore structure, these values are most likely inadequate for modelling the reaction within porous grains. An effective product layer diffusivity could perhaps be defined for porous grains, which would account for the combined effects of solid-state diffusion and intragrain diffusion via the micropores. The magnitude of this diffusivity would be larger than that of the solid-state diffusivity. As the amount of sintering increased, the effective product layer diffusivity would

approach the true value of the solid-state diffusivity, due to micropore disappearance.

Porous grains were also encountered by Caillet [9], who studied the reaction of manganese oxide with hydrogen sulfide, using a variable property grain model. Caillet [9] found that the value of the grain diffusion coefficient needed for a good fit of the experimental data was different for sintered and unsintered pellets. The grain diffusion coefficient determined for unsintered pellets was about 6 times greater than that found for presintered pellets. He explained that cracks and fissures in the grains of unsintered pellets provide an easier diffusion path and caused the diffusion coefficient obtained from experimental data to be higher than the true solid-state diffusion coefficient.

The solid-state diffusivity was varied in the present model to see the effect of this parameter on the model predictions. Figure 43 shows the data and model estimates for the reaction of a highly sintered pellet at 836°C. As expected, varying D_{As} by a factor of 10 above or below the experimental value of 10.7×10^{-8} cm^2/sec significantly increases or decreases the model predictions, respectively. The reaction for this particular case is controlled by product layer diffusion and therefore, the reaction rate is very sensitive to the choice of solid-state diffusivity.

Conversion data and model predictions for a pellet presintered only 30 minutes are shown in Figure 44. Again, the solid-state diffusion coefficient was varied above and below the experimental value to note its effect on the model. In this case, increasing D_{As} by a factor of 10

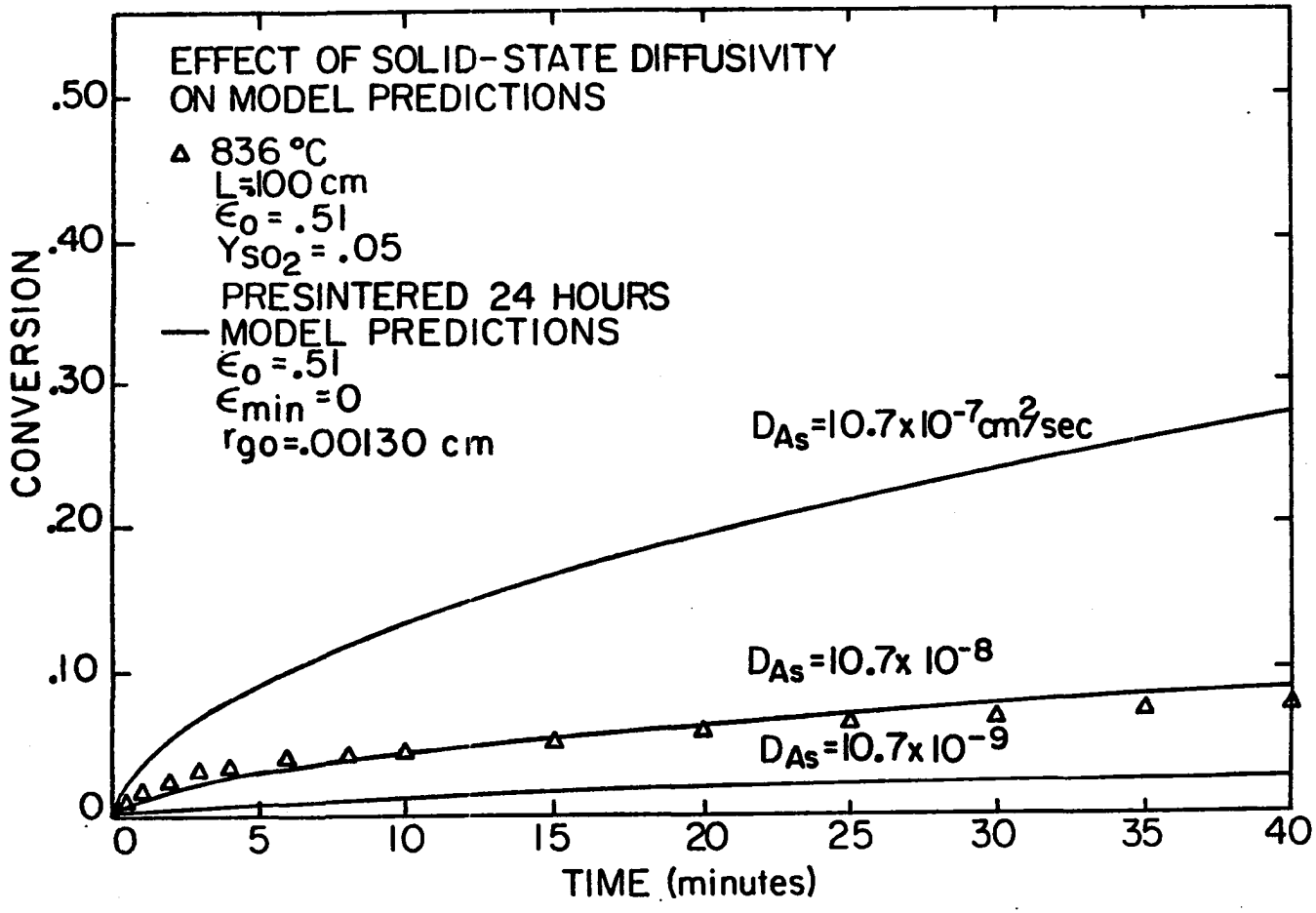

Figure 43. The effect of solid-state diffusivity on the model predictions of conversion vs time for CaO pellets presintered at 1000°C for 24 hours

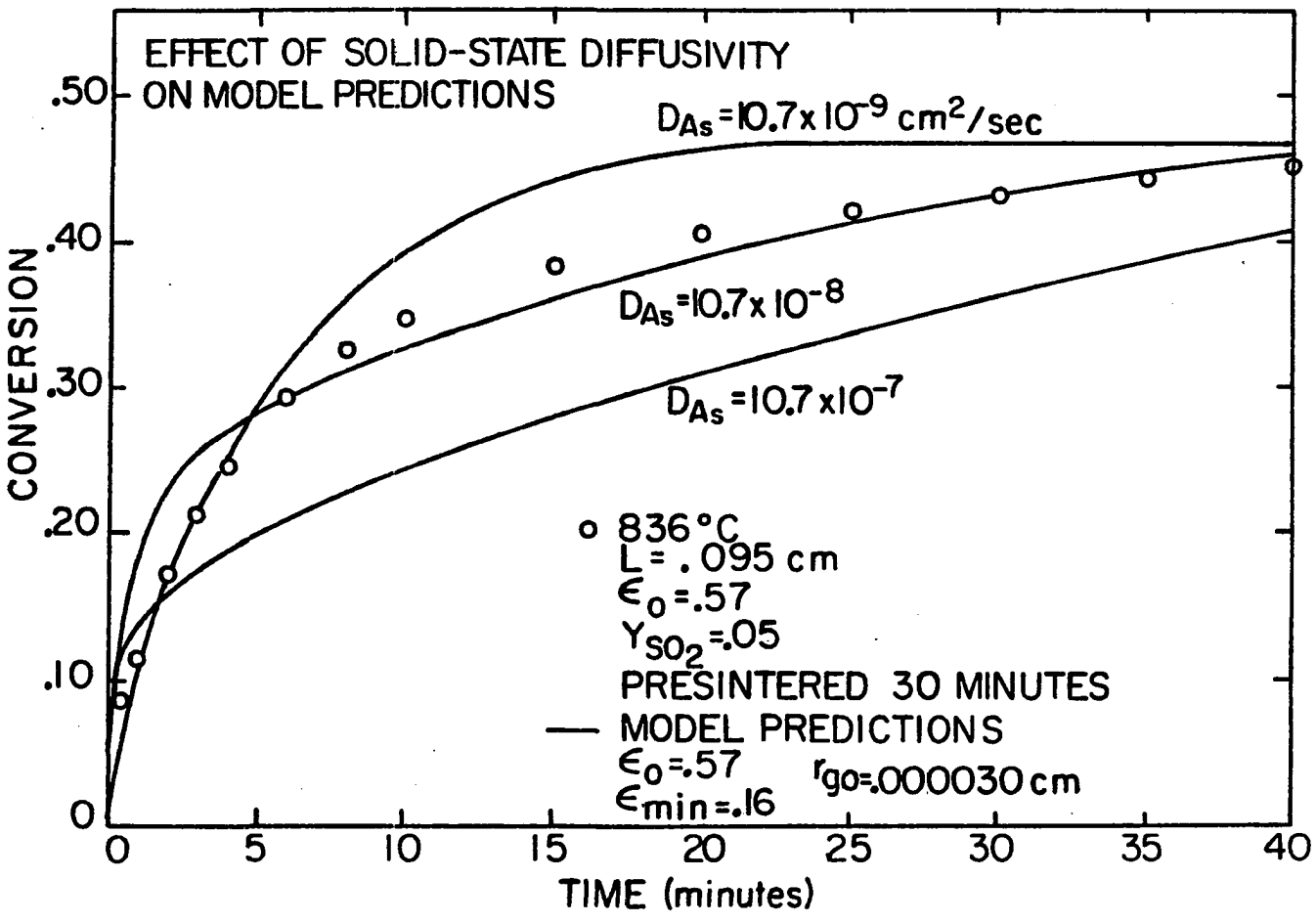

Figure 44. The effect of solid-state diffusivity on the model predictions of conversion vs time for CaO pellets presintered at 1000°C for 30 minutes

decreases the predicted conversion levels at late reaction times. Apparently, the reaction becomes pore diffusion limited and increasing D_{As} causes a more rapid product layer growth around the grains near the surface of the pellet, reducing the surface porosity and net flux of SO_2 into the pellet. The result is a faster reaction initially, but then an earlier slow down of the rate due to surface pore closure. Lowering D_{As} has the opposite effect, as it allows for a more uniform reaction throughout the pellet, reducing the effects of pore closure.

In both Figures 43 and 44, the effect of D_{As} on the model predictions appears to be quite significant. This underscores the importance of obtaining a reliable experimental estimate of D_{As} in order to test the applicability of this model to this particular reaction system. From Figure 44, it appears that a value of D_{As} slightly lower than the experimental value of 10.7×10^{-8} cm^2/sec would provide a better fit of the data. However, it is unclear whether the actual value of D_{As} should be lower than 10.7×10^{-8} cm^2/sec, or whether the model is incorrect for these conditions.

5. Effect of changing temperature

Experiments were performed to examine the effect of an increasing temperature on the conversion-time behavior of CaO pellets reacting with SO_2. After 4 minutes of reaction, at a certain temperature, the tube furnace was allowed to heat up to a specified new temperature. The reaction rate was monitored before and during the temperature increase.

Figure 45 shows experimental data for the sulfation of CaO pellets at 836^o, 742^o, and at a variable temperature ranging from 742^o to 836^oC.

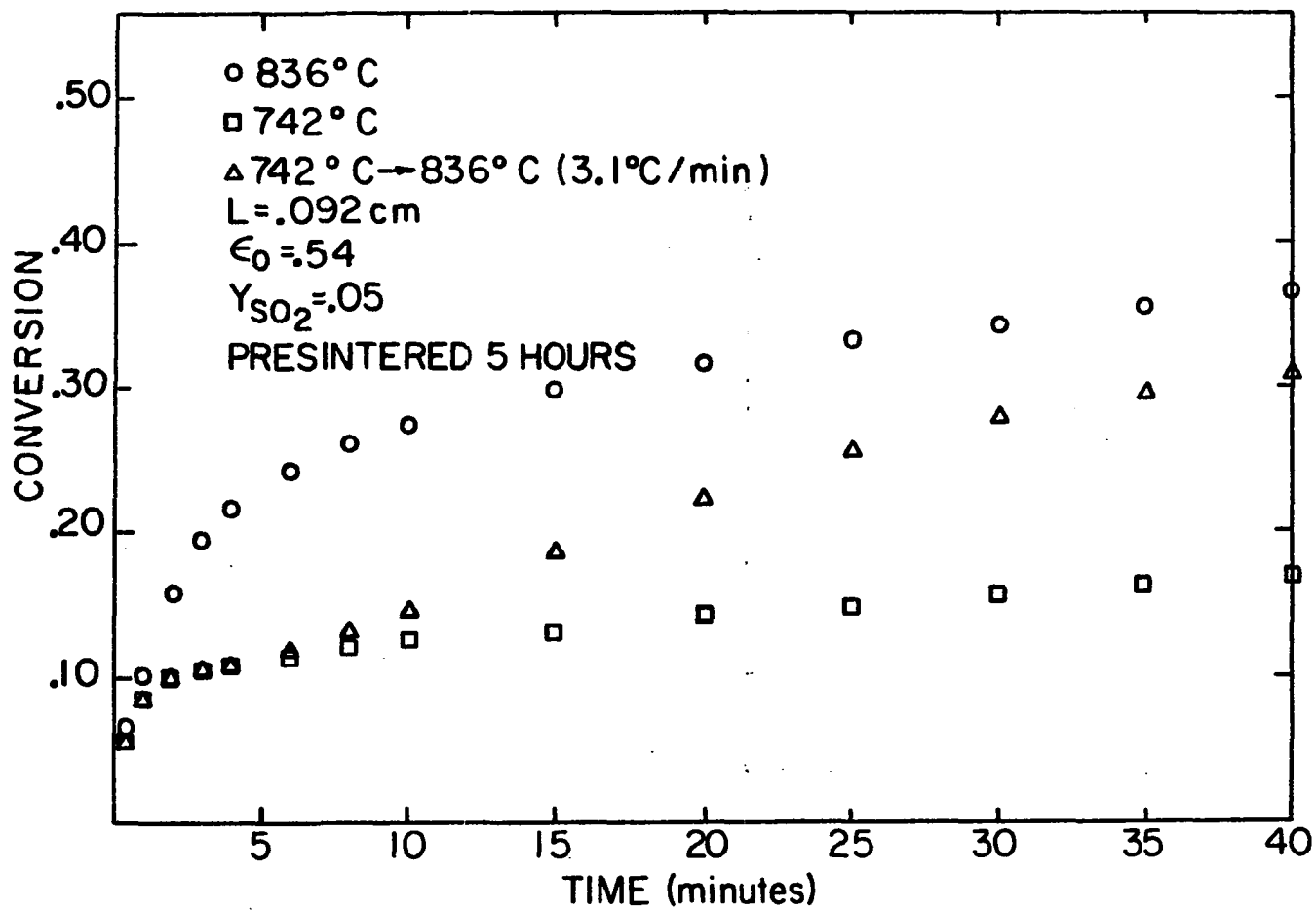

Figure 45. The effect of increasing temperature, during reaction, on the conversion-time behavior of the sulfation of CaO pellets

The temperature increase for the variable temperature run was initiated after 4 minutes of reaction by setting the furnace controller at 836°C. Assuming the rate of temperature increase was linear, and knowing that 836°C was obtained after 30 minutes of heating, the temperature increased at a rate of 3.1°C/min. The variable temperature data rises above the 742°C data shortly after 4 minutes of reaction, and then approaches the 836°C data in an asymptotic fashion. This suggests that solid-state diffusion is controlling the reaction at these conditions and that the increasing temperature causes an increase in reaction rate due to the increasing value of the solid-state diffusivity.

Figure 46 shows similar data for highly presintered pellets reacted at 929°, 836°, and at a temperature rising from 836° to 929°C. The rate of temperature increase from 836° to 929°C was 1.4°C/min. This rate is much slower than the rate between 742° and 836°C, and in fact, after 40 minutes of reaction, the final temperature for the variable temperature run was only 886°C. Thus, the reaction rate did not increase as much as that shown previously in Figure 45. However, an increase was noted and can probably also be attributed to the effect of increasing temperature on the solid-state diffusivity.

The one-dimensional expanding grain model was modified to account for an increasing temperature and was then applied to the data. The model parameters that are temperature dependent were allowed to vary with the changing temperature. These include the reaction rate constant, effective diffusivity, solid-state diffusivity, and total gas concentration. A linear temperature increase was assumed in the model,

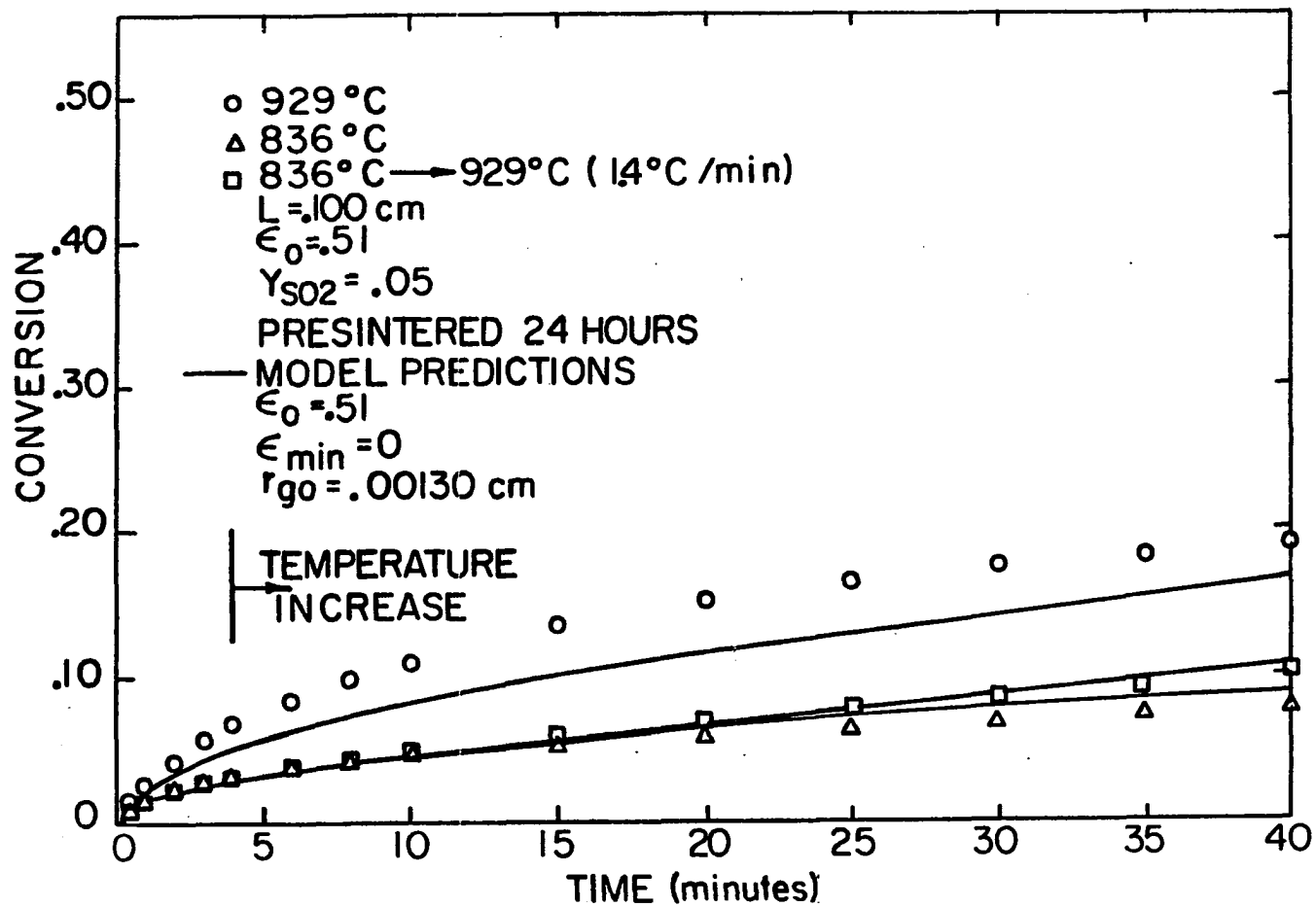

Figure 46. The effect of increasing temperature, during reaction, on the conversion-time behavior of the sulfation of CaO pellets

but other temperature functions could easily be incorporated.

Figure 46 shows a comparison between the variable temperature model predictions and experimental data from the reaction of pellets presintered for 24 hours. The top and bottom curves are the same model predictions as shown in Figure 38 for a constant temperature, whereas the middle curve is from the variable temperature model. A very good fit of the variable temperature data is observed, indicating the model correctly predicts increasing overall reaction rates with increasing temperatures, for these reaction conditions. The model parameters used in the variable temperature model predictions in Figure 46 are the same as those listed in Table 13 for the 836°C reaction. The only additional parameters required were the linear temperature increase of 1.4°C/min, which was initiated after 4 minutes of reaction, the chemical reaction activation energy (19.1 kcal/mole), and the solid-state diffusivity activation energy (35.6 kcal/mole).

Using the value of initial grain radius (0.26 μm) used to model the 836°C data in Figure 36, and applying it to the 742°C data in Figure 45 resulted in a conversion curve that was higher than the 836°C curve at all except early reaction times. For this reason, the variable temperature model did not adequately model the increasing temperature data shown in Figure 45. However, from Figure 46, it was shown that if the constant temperature model correctly predicts the relative positions of conversion curves at two different temperatures, the variable temperature model then correctly predicts the trend in the reaction data for an increasing temperature run.

A further test of the variable temperature model was made using the lime sulfation data of Christman and Edgar [13], shown in Figure 47. For the particular reaction conditions studied, they found that the reaction curve at 650°C lay above the 950°C curve, while the curve for a sample reacted at 950°C, and then cooled to 650°C, asymptotically approached the 650°C curve.

To see if the variable temperature model would predict this type of behavior, structural parameters were chosen such that the constant temperature model would predict a 650°C conversion curve to be above an 850°C curve. Using an initial grain radius of 0.20 μm achieved this, as shown in Figure 48. Instability was encountered in the model at 950°C, thus 850°C was used as the upper temperature. The solid lines in Figure 48 represent the model predictions for reactions carried out at constant temperature, while the dashed lines are predictions from the variable temperature model for a reaction temperature decreasing from 850° to 650°C. Each dashed line was computed using the same model parameters, except the temperature decrease for one curve was initiated after 5 minutes of reaction, while the second was initiated after 15 minutes. In each case, the variable temperature curve initially drops below the 850°C curve, begins to increase in slope, and eventually intersects and goes above the 850°C curve. Overall, therefore, the variable temperature model does predict an increase in reaction rate with decreasing temperature, for these particular conditions.

The rate of temperature decrease chosen for Figure 48 (-50°C/min) was used to simulate a rapid cool down, such as that used by Christman

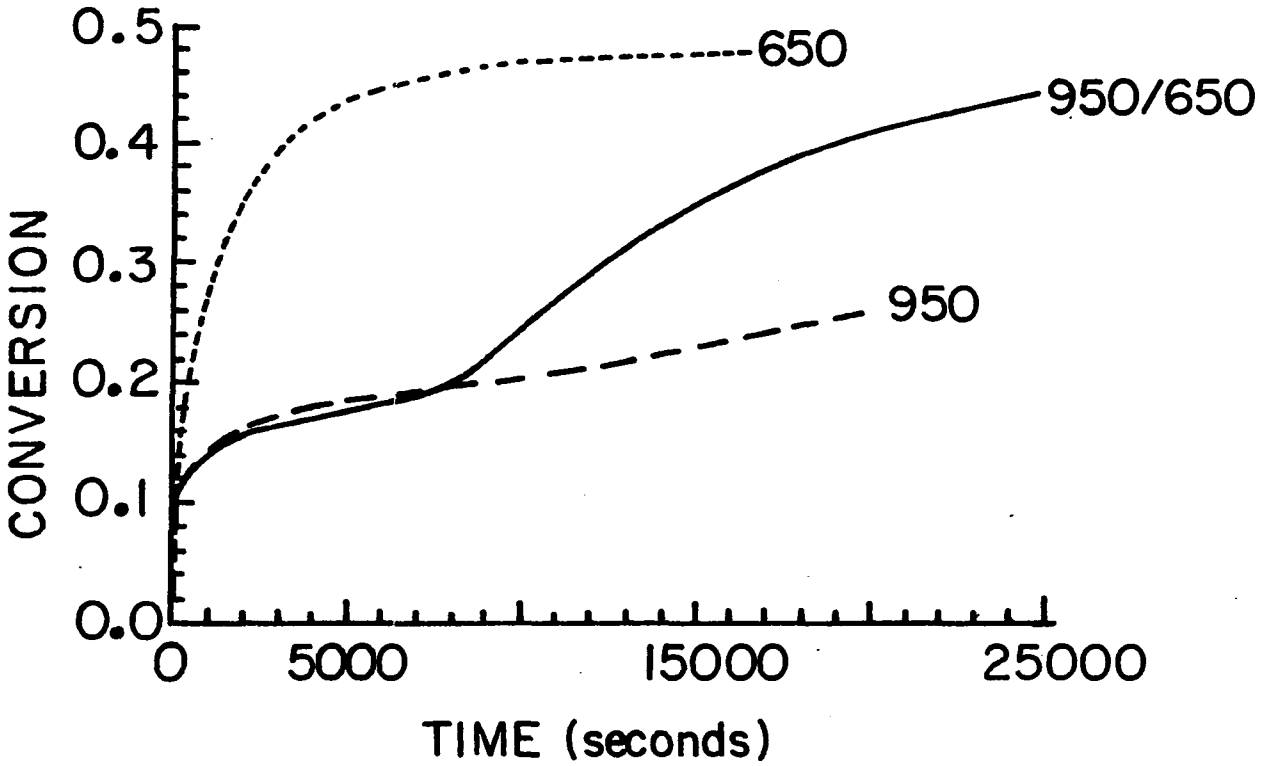

Figure 47. The effect of decreasing temperature, during reaction, on the conversion-time behavior of the sulfation of precalcined Lowellville limestone [13]

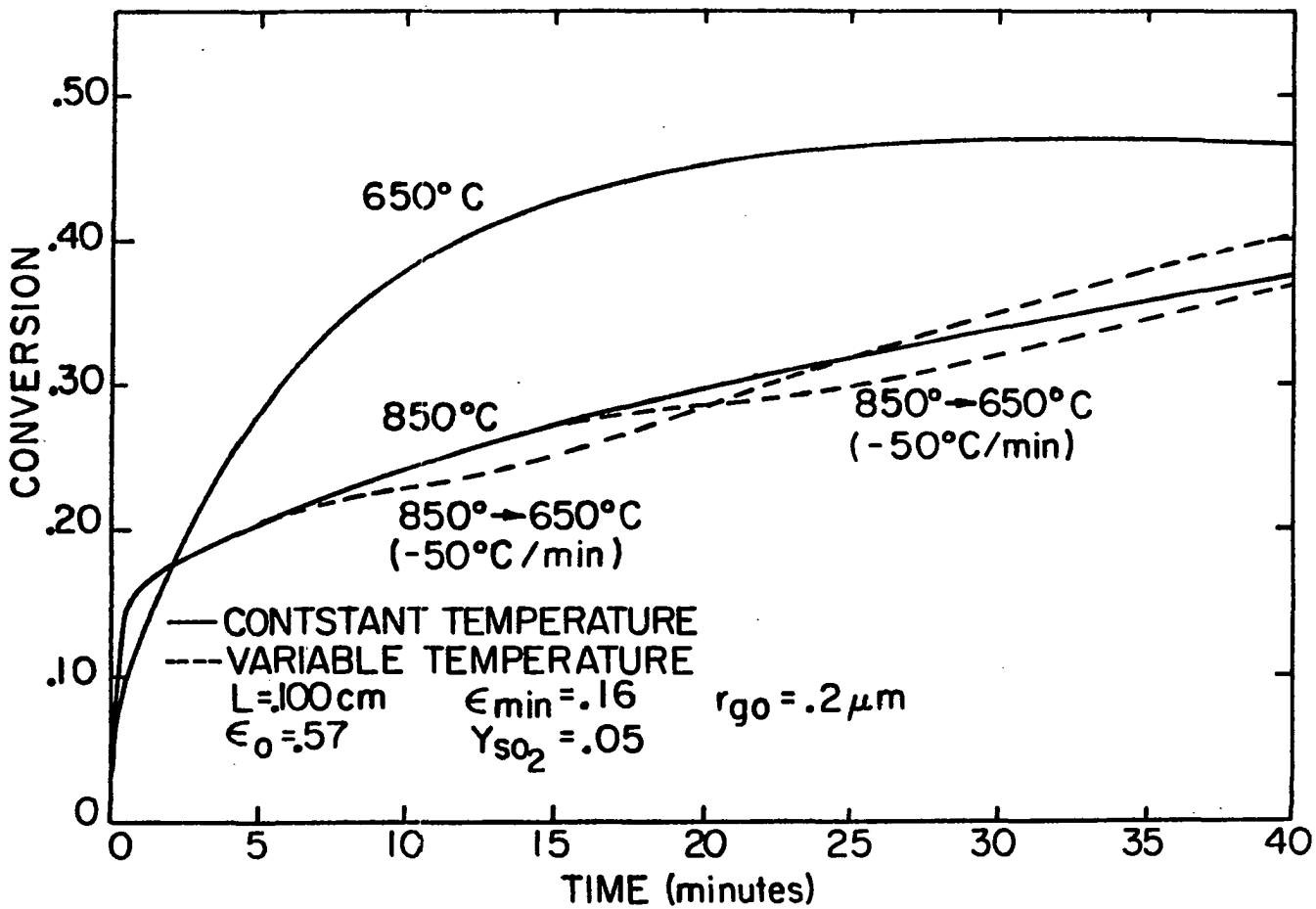

Figure 48. The effect of decreasing temperature, during reaction, on the variable temperature model predictions

and Edgar [13] in obtaining the data in Figure 47. However, no actual numerical value of the cooling rate was reported by Christman and Edgar.

It was determined that increasing the rate of temperature decrease from -50°C/min to -400°C/min only slightly affected the model predictions. The resultant curve dropped a little more initially, but then increased at a slightly higher rate. Apparently, the variable temperature curves initially drop off due to the effect of decreasing temperature on the reaction rate constant, and the several diffusivities. However, the solid-state diffusivity decreases more than the effective diffusivity, reducing the tendency of the SO_2 to react mostly near the outside surface of the pellet. Surface pore closure effects decline and the SO_2 diffuses deeper into the pellet before reacting. Ultimately, the overall reaction rate increases due to a more homogeneous reaction throughout the pellet.

Christman and Edgar [13] explained the results of Figure 47 using an adsorption argument. They suggested that the increased rate observed for a decreasing temperature may be caused by an exothermic adsorption step. As the product layer thickens, the rate controlling mechanism becomes adsorption of SO_2 onto the surface of the product layer, and since adsorption is exothermic, decreasing the temperature from 950°C to 650°C (Figure 47) increases the adsorption rate and thus, the overall reaction rate.

Adsorption may play a role in this conversion behavior, but not necessarily. Figure 48 shows that the variable temperature model predicts higher conversion rates with decreasing temperature, and it has no adsorption step incorporated into its development. The increase in

conversion is predicted on the basis of intrapellet and intragrain diffusion effects. If the activation energy for intragrain diffusion was lower than that for intrapellet diffusion, an increase in conversion with a decrease in temperature would not be predicted for the conditions shown in Figure 48. However, since in reality the solid-state diffusivity is much more temperature sensitive than the effective diffusivity, when the reaction is pore limited a decrease in temperature can result in an increase in overall reaction rate.

VII. CONCLUSIONS

The kinetics of the reaction between SO_2 and calcium oxide, produced from calcining reagent grade calcium hydroxide, were studied using thermogravimetric analysis. It was found that depositing a thin layer of $Ca(OH)_2$ on a quartz plate was an excellent method of supporting the solid, since no detectable amounts of solid flaked off during either the calcination or sulfation reactions. Chemical reaction control was obtained with these samples, making it possible to directly determine reaction rate constants. Pellets pressed from $Ca(OH)_2$ powder were calcined and sulfated to study the effects of diffusional resistances on the overall reaction.

Results from the thermogravimetric analyzer (TGA) confirmed that sulfation of CaO produces different products at different reaction conditions. In the presence of oxygen, at temperatures above 740°C the primary product is $CaSO_4$ and the reaction is first order in SO_2 concentration. At temperatures below 450°C, the major product is $CaSO_3$ and the reaction is zero order. In between these temperatures the solid product is a mixture of $CaSO_3$ and $CaSO_4$ which varies in proportion depending on reaction temperature, reaction time, and reactant gas composition.

The reaction rate constant for the formation of $CaSO_4$ was expressed in Arrhenius form and is given by Equation (77). An activation energy of 19.1 kcal/mole was determined. Similarly, the reaction rate constant for the formation of $CaSO_3$ is given by Equation (78). The activation energy was found to be 15.4 kcal/mole.

The samples reacted in an oxygen-free atmosphere gave higher conversions than those reacted with oxygen present. This was true for all temperatures except 830°C.

From mercury porosimetry, it was determined that CaO produced by calcining reagent grade $Ca(OH)_2$ possesses an extensive micropore structure, with a great number of pores having a radius of 22 Å. Both sintering and sulfation causes a decrease in the total volume of pores without greatly affecting the pore size distribution.

From conversion-time data on the sulfation of sintered CaO on quartz plates, it appears that pore closure, product layer diffusion, and product sintering all become important factors at high conversion levels. The interaction of these mechanisms appears to be a function of temperature and SO_2 concentration. At 930°C, and at later reaction times, the overall reaction appears to be under product layer diffusion control and is first order in SO_2 concentration. More information on the structure of the deposited solid during reaction is required for a better understanding of the reaction at high conversion levels.

The solid-state diffusivity, D_{As}, of SO_2 through $CaSO_4$ was estimated using two simple diffusion models and rate data from the reaction of highly sintered CaO. The estimates from these models are very close to each other, primarily because the estimates were made at low conversion levels, which corresponds to a small product layer thickness relative to the original solid dimensions. Values of D_{As} reported in the literature are of the same order of magnitude as those determined in this study. However, the values here are much less model

dependent than those determined in previous studies and therefore, are considered an improvement over past results. The activation energy for solid-state diffusion was determined to be 35.6 kcal/mole.

Reaction measurements made on CaO pellets, presintered for varying amounts of time, showed that the optimum reaction temperature increases with increased presintering time. Conversion data from unsintered pellets showed that the optimum reaction temperature also increases with increased initial porosity. In both cases, the increases in optimum temperature are caused by increases in the relative pore size, which is indicative of pore closure effects.

A one-dimensional expanding grain model was developed and applied to the lime pellet sulfation data. The pellets in the model were assumed to be infinite slabs, which resulted in a one-dimensional model. For the pellet dimensions experimentally used, the one-dimensional model predictions were identical to that of a two-dimensional model, where cylindrical geometry was assumed. The pellets were also assumed isothermal, which was supported by experimental measurements of pellet center temperatures, for various sized pellets. Making the model one-dimensional and isothermal greatly reduced the complexity of the resulting equations. The equations were solved numerically using a digital computer.

The one-dimensional expanding grain model fit the data from highly sintered pellets quite good, but generally did worse as the pellet presintering time decreased. One explanation for this is that the model does not account for sintering during reaction, and while solid reactant

sintering should not have been significant for highly presintered pellets, it probably was for unsintered or slightly presintered pellets. Another explanation is that grains of CaO produced from $Ca(OH)_2$ contain micropores, while the model assumes dense, nonporous grains. For highly presintered pellets, this micropore structure will be greatly reduced or disappear entirely, making the model more conceptually correct.

In order to prevent the model from overestimating conversion levels at late reaction times, it was necessary to introduce a minimum porosity, ϵ_{min}, parameter into the model. This parameter accounts for the fact that the solids rarely react to their theoretical maximum conversion level. Because of the irregular shapes and packing of the CaO grains, it is possible that local blockages occur within the pellet which prevent the SO_2 from reaching certain zones of unreacted solid.

Even though the model does not fit all of the data as well as desired, it does predict general trends in the data very well. The model accurately predicts an optimum initial grain size at any given reaction temperature. It also correctly predicts the upward effect of increased initial grain size on the optimum reaction temperature. Both of these predictions are supported by experimental information obtained in this study.

The effect of an initial grain size distribution on the conversion-time predictions of the model were considered. The size distribution effects were not as important as the effect of the average initial grain size. Therefore, because of the uncertainties involved in measuring an average initial grain size, and since the grains are not actually

spherical in shape, it would seem inappropriate to try to improve the model fit by introducing a grain size distribution into the model.

For a reaction that is controlled by product layer diffusion, the model correctly predicts an increase in reaction rate from an increase in temperature. The model also predicts that for a reaction controlled by pore diffusion, a decrease in temperature is accompanied by an initial decrease and eventual increase in reaction rate. This last result offers an alternative explanation to the experimental results of Christman and Edgar [13] shown in Figure 47. An increase in reaction rate with decreasing temperature may simply be due to pore closure effects, rather than SO_2 adsorption effects as suggested by Christman and Edgar [13].

VIII. RECOMMENDATIONS

1. The effect of grain micropores on the reaction behavior needs to be further investigated. Pellets of CaO, presintered for varying amounts of time, could be partially reacted with SO_2 and then cleaved to expose a cross-section of the pellet. Using ion sputtering, the grains on the exposed pellet surface could then be cross-sectioned to reveal the inside structure of the grains. Using the scanning Auger microscope, the sulfur distribution within the grains could be analyzed. Similarly, the sulfur distribution could be obtained using x-ray analysis in conjunction with the scanning electron microscope. If micropores within the grains influence the reaction, one might expect "fingers" of $CaSO_4$ reaching into the interior regions of the grains. As the presintering time increased, these "fingers" would tend to disappear due to micropore closure.

2. It was observed that product layer expansion and the resultant decrease in porosity are not entirely responsible for the early shut down in reaction rate, as final conversion levels were usually less than the theoretical maximum conversion levels. The effect of reaction and sintering on the internal pore structure should be examined to help determine the mechanism that limits the ultimate conversion. Both mercury porosimetry and nitrogen adsorption/desorption should be used for this study. Also, measurements of diffusion rates using the diffusion cell would be helpful in determining the limiting mechanism.

3. On the basis of the information obtained in the proposed study, it will be important to investigate whether it is necessary to include

the effects of micropores in a gas-solid reaction model. Methods of incorporating grain porosity into the grain model may need to be developed and the results compared to experimental data. In addition, a bimodal pore model should be tested using the same data to note the advantages or disadvantages of this type of model over the grain model.

4. Electron microprobe analyses of partially and completely reacted pellets would provide useful information on the local conversion levels within the pellets. This information would be useful for testing the local conversion predictions of the gas-solid reaction models.

IX. REFERENCES

1. Bartlett, R. W., Krishnan, N. G., and VanHecke, M. C. 1973. Micrograin Models of Reacting Porous Solids with Approximations to Logarithmic Solid Conversion. Chem Eng. Sci. 28: 2179-2186.

2. Beruto, D., Barco, L., Searcy, A. W., and Spinolo, G. 1980. Characterization of the Porous CaO Particles Formed by Decomposition of $CaCO_3$ and $Ca(OH)_2$ in Vacuum. J. Am. Ceram. Soc. 63(7-8): 439-443.

3. Bhatia, S. K., and Perlmutter, D. D. 1981. A Random Pore Model for Fluid-Solid Reactions: II. Diffusion and Transport Effects. AIChE J. 27(2): 247-254.

4. Bhatia, S. K., and Perlmutter, D. D. 1981. The Effect of Pore Structure on Fluid-Solid Reactions: Application to the SO_2-Lime Reaction. AIChE J. 27(2): 226-234.

5. Bird, R. B., Stewart, W. E., and Lightfoot, E. N. 1960. Transport Phenomena. John Wiley and Sons, Inc., New York, N.Y.

6. Borgwardt, R. H. 1970. Kinetics of the Reaction of SO_2 With Calcined Limestone. Environ. Sci. Technol. 4(1): 59-63.

7. Borgwardt, R. H., and Harvey, R. D. 1972. Properties of Carbonate Rocks Related to SO_2 Reactivity. Environ. Sci. Technol. 6(4): 350-360.

8. Bowen, J. H., and Cheng, C. K. 1969. A Diffuse Interface Model for Fluid-Solid Reactions. Chem. Eng. Sci. 24: 1829-1831.

9. Caillet, D. A. 1980. The Conversion of Manganese (II) Oxide to Manganese (II) Sulfide: Effect of Variable Solid Properties. Ph.D. Thesis. Louisiana State University.

10. Calvelo, A., and Smith, J. M. 1970. Intrapellet Transport in Gas-Solid Noncatalytic Reactions. Chemeca 1970: 1-24.

11. Carnahan, B., Luther, H. A., and Wilkes, J. A. 1969. Applied Numerical Methods. John Wiley and Sons, Inc., New York, N.Y.

12. Christman, P. G., and Edgar, T. F. 1980. Distributed Pore Size Model for the Sulfation of Limestone. Paper presented at the 73rd Annual AIChE Meeting, Chicago, IL.

13. Christman, P. G., and Edgar, T. F. 1980. The Effect of Temperature on the Sulfation of Limestones. Paper presented at the 73rd Annual AIChE Meeting, Chicago, IL.

14. Christman, P. G., and Edgar, T. F. 1981. The Kinetics and Product Distribution of the CaO/SO_2 Reaction. Paper presented at the 74th Annual AIChE Meeting, New Orleans, LA.

15. Chrostowski, J. W., and Georgakis, C. 1978. A Pore Plugging Model for Gas-Solid Reactions. Paper presented at the 5th International Symposium, Chemical Reaction Engineering, Houston, TX.

16. Coutant, R. W., Barrett, R. E., and Lougher, E. H. 1970. SO_2 Pickup by Limestone and Dolomite Particles in Flue Gas. J. Engineering for Power 92: 113-122.

17. Denbigh, K. G., and Beveridge, G. S. G. 1962. The Oxidation of Zinc Sulphide Spheres in an Air Stream. Trans. Inst. Chem. Engr. 40: 23-34.

18. Evans, R. B., Watson, G. M., and Mason, E. A. 1961. Gaseous Diffusion in Porous Media at Uniform Pressure. J. Chem. Phys. 35(6): 2076-2083.

19. Fieldes, R. B., Burdett, N. A., and Davidson, J. F. 1979. Reaction of Sulfur Dioxide with Limestone Particles: The Influence of Sulfur Trioxide. Trans. Inst. Chem. Eng. 57: 276-279.

20. Fischer, H. C. 1955. Calcination of Calcite: I. Effect of Heating Rate and Temperature on Bulk Density of Calcium Oxide. J. Am. Ceram. Soc. 38(7): 245-251.

21. Georgakis, C., Szekely, J., Chang, C. W., Chrostowski, J. W., and Trinh, T. 1977. Modelling Desulfurization Reactions in Fluidized Bed Combustors. Report to 5th International Conference on Fluidized Bed Combustion, Washington, D.C.

22. Hartman, M., and Coughlin, R. W. 1974. Reaction of Sulfur Dioxide with Limestone and the Influence of Pore Structure. Ind. Eng. Chem. Proc. Des. Dev. 13(3): 248-253.

23. Hartman, M., and Coughlin, R. W. 1976. Reaction of Sulfur Dioxide with Limestone and the Grain Model. AIChE J. 22(3): 490-498.

24. Hartman, M., and Trnka, O. 1980. Influence of Temperature on the Reactivity of Limestone Particles with Sulfur Dioxide. Chem. Eng. Sci. 35: 1189-1194.

25. Hatfield, J. D., Kim, Y. K., Mullins, R. C., and McClellan, G. H. 1970. Investigation of the Reactivities of Limestone to Remove Sulfur Dioxide from Flue Gas. NTIS Publication No. PB 202 407.

26. Hills, A. W. D. 1968. The Mechanism of the Thermal Decomposition of Calcium Carbonate. Chem. Eng. Sci. 23: 297-320.

27. Instruction Manual, Accusorb 2100E, Physical Adsorption Analyzer. 1980. Micromeritics Instrument Corp., Norcross, GA.

28. Ishida, M., and Wen, C. Y. 1968. Comparison of Kinetic and Diffusional Models for Solid-Gas Reactions. AIChE J. 14(2): 311-317.

29. Ishida, M., and Wen, C. Y. 1971. Comparison of Zone-Reaction Model and Unreacted-Core Shrinking Model in Gas-Solid Reactions-I. Isothermal Analysis. Chem. Eng. Sci. 26: 1031-1041.

30. Kawasaki, E., Sanscrainte, J., and Walsh, J. 1962. Kinetics of Reduction of Iron Oxide with Carbon Monoxide and Hydrogen. AIChE J. 8(1): 48-52.

31. Kim, K. K., and Smith, J. M. 1974. Diffusion in Nickel Oxide Pellets, Effects of Sintering and Reduction. AIChE J. 20(4): 670-678.

32. Kito, M., and Wen, C. Y. 1975. Analysis of SO_2-Limestone Reaction Systems: Part II. Simulation. AIChE Symposium Series No. 147 71: 119-125.

33. Levenspiel, O. 1962. Chemical Reaction Engineering. 2nd Ed. John Wiley and Sons, Inc., New York, N.Y.

34. Mason, E. A., Malinauskas, A. P., Evans, R. B. 1967. Flow and Diffusion of Gases in Porous Media. J. Chem. Phys. 46(8): 3199-3216.

35. Mason, E. A., and Marrero, T. R. 1970. The Diffusion of Atoms and Molecules. Advan. At. Mol. Phys. 6: 155-232.

36. O'Neill, E. P., Keairns, D. L., and Kittle, W. F. 1976. A Thermogravimetric Study of the Sulfation of Limestone and Dolomite--The Effect of Calcination Conditions. Thermochimica Acta. 14: 209-220.

37. Pigford, R. L., and Sliger, G. 1973. Rate of Diffusion-Controlled Reaction Between a Gas and a Porous Solid Sphere. Ind. Eng. Chem. Proc. Des. Dev. 12(1): 85-91.

38. Potter, A. E. 1969. Sulfur Oxide Capacity of Limestones. Ceramic Bulletin 48(9): 855-858.

39. Ramachandran, P. A., and Smith, J. M. 1977. A Single Pore Model for Gas-Solid Non-Catalytic Reactions. AIChE J. 23(3): 353-361.

40. Ramachandran, P. A., and Smith, J. M. 1977. Effect of Sintering and Porosity Changes on Rates of Gas-Solid Reactions. Chem. Eng. J. 14: 137-146.

41. Ranade, P. 1977. Effects of Sintering of Solids on the Kinetics of Non-Catalytic Gas-Solid Reactions. Ph.D. Thesis. Louisiana State University.

42. Reid, W. T. 1970. Basic Factors in the Capture of Sulfur Dioxide by Limestone and Dolomite. J. of Engineering for Power 92: 11-16.

43. Sampath, B. S., Ramachandran, P. A., and Hughes, R. 1975. Modelling of Non-Catalytic Gas-Solid Reactions. I. Transient Analysis of the Particle-Pellet Model. Chem. Eng. Sci. 30: 125-134.

44. Simons, G. A., and Rawlins, W. T. 1980. Reaction of Sulfur Dioxide and Hydrogen Sulfide with Porous Calcined Limestone. Ind. Eng. Chem. Proc. Des. Dev. 19(4): 565-572.

45. Slack, A. V. 1971. SO_2 Removal from Waste Gases. Noyes Development Corporation, Park Ridge, N.J.

46. Smith, J. M. 1962. Chemical Engineering Kinetics. 2nd ed. McGraw-Hill, New York, N.Y.

47. Szekely, J., and Evans, J. W. 1970. A Structural Model for Gas-Solid Reactions with a Moving Boundary. Chem. Eng. Sci. 25: 1091-1107.

48. Szekely, J., Evans, J. W., and Sohn, H. Y. 1976. Gas-Solid Reactions. Academic Press, New York, N.Y.

49. Szekely, J., Lin, C. I., and Sohn, H. Y. 1973. A Structural Model for Gas-Solid Reactions with a Moving Boundary. V. An Experimental Study of the Reduction of Porous Nickel Oxide Pellets with Hydrogen. Chem. Eng. Sci. 28: 1975-1989.

50. Szekely, J., and Propster, M. 1975. Structural Model for Gas-Solid Reactions with a Moving Boundary. VI. The Effect of Grain Size Distribution on the Conversion of Porous Solids. Chem. Eng. Sci. 30: 1049-1055.

51. Ulerich, N. H., O'Neill, E. P., and Keairns, D. L. 1977. A Thermogravimetric Study of the Effect of Pore Volume--Pore Size Distribution on the Sulfation of Calcined Limestones. Annual Meeting of the North American Thermal Analysis Society, St. Louis, MO.

52. Ulrichson, D. L., and Yake, D. E. 1980. Numerical Analysis of a Finite Cylindrical Pellet Model in Solid-Gas Reactions. Chem. Eng. Sci. 35: 2207-2212.

53. Wakao, N., and Smith, J. M. 1962. Diffusion in Catalyst Pellets. Chem. Eng. Sci. 17: 825-834.

54. Wen, C. Y., and Ishida, M. 1973. Reaction Rate of Sulfur Dioxide with Particles Containing Calcium Oxide. Environ. Sci. Technol. 7(8): 703-708.

55. Woodside, W., and Messmer, J. H. 1961. Thermal Conductivity of Porous Media. I. Unconsolidated Sands. J. Applied Physics 32(9): 1688.

56. Yagi, S., and Kunii, D. 1955. Fluidized-Solid Reactors for Particles with Decreasing Diameters. Chemical Engineering (Tokyo) 19: 500.

57. Yake, D. E. 1979. Modeling of Bulk Flow, Reversibility and Pore Closure with a Grain Model for Gas-Solid Reactions. Ph.D. Thesis. Iowa State University.

58. Yake, D. E., and Ulrichson, D. L. 1981. Kinetics of Calcium Oxide Chlorination and Pore Closure Models. Chem. Eng. Commun. 12: 97-120.

59. Young, W. A. 1982. A General Grain Model for Gas-Solid Reactions in Cylindrical Pellets. M.S. Thesis. Iowa State University.

X. ACKNOWLEDGMENTS

The author wishes to thank Dr. Dean L. Ulrichson for his continuous guidance and support during this research program. It was very enlightening and gratifying working with him throughout graduate school.

Special thanks are extended to my parents, sisters, and brother for all of the love and support they have given me during this work.

The author is grateful for a graduate fellowship provided by the Amoco Foundation. This work was also supported by the Office of Basic Energy Sciences, Chemical Sciences Division, under Contract No. W-7405-ENG-82.

Appreciation is expressed to Jim Voigt for assistance with some analytical work.

The author especially wishes to thank his fellow graduate students at Iowa State and his many friends from Iowa City who have made graduate school a very exciting experience.

XI. APPENDIX A: COMPUTER PROGRAM FOR THE ONE-DIMENSIONAL EXPANDING GRAIN MODEL

```
1.      C
2.      C     ================================================================
3.      C
4.      C                        PROGRAM NAME: ODGM
5.      C
6.      C          THIS PROGRAM CONTAINS A ONE-DIMENSIONAL GRAIN MODEL
7.      C     FOR THE SIMULATION OF A SOLID-GAS REACTION WHICH MAY BE
8.      C     ACCOMPANIED BY PRODUCT EXPANSION OR CONTRACTION.  THE
9.      C     REACTING SOLID IS ASSUMED TO BE A SLAB WITH GASEOUS
10.     C     REACTANT IN CONTACT WITH THE TOP AND BOTTOM SURFACES OF
11.     C     THE SLAB.
12.     C
13.     C     ================================================================
14.     C
15.           INTEGER PRTDZ,Z,ZMAX,ZMAXM1
16.           REAL ALPHA,BETA,CHI,GAMMA,SIGMA
17.           REAL B,C,D
18.           REAL CNVLOC(30),CNVPEL,CONCB,CONCD,CONCT,DAC,DKA,DACEFF,
19.          &     DAEOE2(30),DAEPL(30),DAEGR,DELTA(30),DELTSA,DENRAT
20.           REAL DKCOEF,DZ,DZDZ,DT,PSUDT,FOFXL,FOFXM,FOFXR,KRXN,LENGTH,
21.          &     MOLWTA,ONEMC,PORLOC(30),PORPLO,PORPEL,PORMIN,PRTINT
22.           REAL PRTNEX,RAOCT(30),RADC(30),RADGR(30),RADGRO,RDGRO3,
23.          &     TDA(30),TDB(30),TDC(30),TDD(30),TDV(30),TEMP,TIME
24.           REAL TMAX,TSTERR,XL,XM,XR,YABULK,YACORE(30),YALOC(30),
25.          &     YAINIT,YATST(3),ZTERM,DT2,TIME2
26.     C
27.     C     ----------------------------------------------------------------
28.     C
29.     C     GLOSSARY:
30.     C
31.     C     ALPHA -- VARIABLE USED TO SIMPLIFY CALCULATIONS
32.     C     B -- STOICHIOMETRIC COEFFICIENT OF SOLID REACTANT
33.     C     BETA -- VARIABLE USED TO SIMPLIFY CALCULATIONS
34.     C     C -- STOICHIOMETRIC COEFFICIENT OF GASEOUS PRODUCT
35.     C     CHI -- VARIABLE USED TO SIMPLIFY CALCULATIONS
36.     C     CNVLOC -- LOCAL CONVERSION
37.     C     CNVPEL -- OVERALL PELLET CONVERSION
38.     C     CONCB -- SOLID REACTANT CONC. (G-MOLE/CM3)
39.     C     CONCD -- SOLID PRODUCT CONC. (G-MOLE/CM3)
40.     C     CONCT -- TOTAL GAS CONC. (G-MOLE/CM3)
41.     C     D -- STOICHIOMETRIC COEFFICIENT OF SOLID PRODUCT
42.     C     DAC -- BINARY MOLECULAR DIFFUSIVITY (CM2/SEC)
43.     C     DACEFF -- EFFECTIVE BINARY DIFFUSIVITY IN PRODUCT (CM2/SEC)
44.     C     DAEGR -- EFFECTIVE DIFFUSIVITY IN PRODUCT LAYER (CM2/SEC)
45.     C     DAEOE2 -- DAEPL/PORLOC**2  (CM2/SEC)
46.     C     DAEPL -- EFFECTIVE DIFFUSIVITY OF A THROUGH PELLET (CM2/SEC)
47.     C     DELTA -- DAEPL/(DAC*PORLOC**2)
48.     C     DELTSA -- DAEGR/DACEFF
49.     C     DENRAT -- DENSITY RATIO
50.     C     DKA -- KNUDSEN DIFFUSIVITY OF A THROUGH PELLET (CM2/SEC)
51.     C     DKCOEF -- FACTOR USED TO CALCULATE DKA
52.     C     DT -- TIME INCREMENT FOR REAL TIME  (SEC)
53.     C     DT2 -- SECOND TIME INCREMENT FOR REAL TIME (SEC)
54.     C     DZ -- AXIAL INCREMENT OF LENGTH
55.     C     DZDZ -- DZ*DZ
56.     C     FOFXL -- FUNCTION OF XL
57.     C     FOFXM -- FUNCTION OF XM
58.     C     FOFXR -- FUNCTION OF XR
59.     C     GAMMA -- CHI/DAEPL(Z)
60.     C     KRXN -- REACTION RATE CONSTANT (CM/SEC)
```

```
61.      C     LENGTH -- LENGTH OF PELLET (CM)
62.      C     MOLWTA -- MOLECULAR WEIGHT OF A
63.      C     ONEMC -- 1-C
64.      C     PORLOC -- LOCAL POROSITY
65.      C     PORMIN -- MINIMUM LOCAL POROSITY
66.      C     PORPEL -- PELLET POROSITY
67.      C     PORPLO -- INITIAL PELLET POROSITY
68.      C     PRTDZ -- INCREMENT FOR PRINTING LOOP
69.      C     PRTINT -- PRINTING INTERVAL (SEC)
70.      C     PRTNEX -- TIME OF NEXT PRINTOUT (SEC)
71.      C     PSUDT -- TIME INCREMENT FOR PSEUDO-TIME (SEC)
72.      C     RADC -- RADIUS OF UNREACTED CORE (CM)
73.      C     RADGR -- RADIUS OF GRAIN (CM)
74.      C     RADGRO -- INITIAL RADIUS OF GRAIN (CM)
75.      C     RAOCT -- RXN RATE PER UNIT PELLET VOL./TOTAL GAS CONC. (1/SEC)
76.      C     RDGRO3 -- RADGRO**3
77.      C     SIGMA -- VARIABLE USED TO SIMPLIFY CALCULATIONS
78.      C     TDA,TDB,TDC,TDD,TDV -- VECTORS FOR TRIDAG SUBROUTINE
79.      C     TEMP -- TEMPERATURE (CELSIUS)
80.      C     TIME -- SIMULATED TIME (SEC)
81.      C     TIME2 -- TIME AT WHICH DT = DT2 (SEC)
82.      C     TMAX -- MAXIMUM VALUE OF SIMULATED TIME (SEC)
83.      C     TSTERR -- ALLOWABLE ERROR FOR THE CONVERGENCE TEST
84.      C     XL,XM,XR -- VALUES USED IN FINDING YACORE BY REGULA-FALSI
85.      C     YABULK -- MOLE FRACTION OF A IN BULK STREAM
86.      C     YACORE -- M. F. OF A AT RXN INTERFACE
87.      C     YALOC -- M. F. OF A AT LOCAL INTRAPELLET SITES
88.      C     YAINIT -- INITIAL M. F. OF A
89.      C     YATST -- VALUE OF YALOC USED IN THE CONVERGENCE TEST
90.      C     Z -- AXIAL LENGTH SUBSCRIPT
91.      C     ZMAX -- MAXIMUM VALUE OF Z
92.      C     ZMAXM1 -- ZMAX-1
93.      C
94.      C     ------------------------------------------------------------
95.      C
96.      C     INITIALIZE CONSTANTS
97.      C
98.           READ(5,8010) ZMAX
99.           READ(5,8020) B,C,D
100.          READ(5,8020) CONCB,CONCD
101.          READ(5,8030) DAC,DACEFF,DAEGR
102.          READ(5,8025) DT,PSUDT,KRXN
103.          READ(5,8020) DT2,TIME2
104.          READ(5,8020) PORPLO,PORMIN,DAEMIN
105.          READ(5,8040) PRTINT,LENGTH,RADGRO
106.          READ(5,8020) TMAX,TSTERR,YABULK
107.          READ(5,8020) YAINIT,TEMP,MOLWTA
108.          WRITE(6,9010) ZMAX
109.          WRITE(6,9020) B,C,D
110.          WRITE(6,9025) CONCB,CONCD
111.          WRITE(6,9030) DAC,DACEFF,DAEGR
112.          WRITE(6,9040) DT,PSUDT,KRXN
113.          WRITE(6,9041) DT2,TIME2
114.          WRITE(6,9045) PORPLO,PORMIN,DAEMIN
115.          WRITE(6,9050) PRTINT,LENGTH,RADGRO
116.          WRITE(6,9070) TMAX,TSTERR,YABULK
117.          WRITE(6,9075) YAINIT,TEMP,MOLWTA
118.          ZMAXM1 = ZMAX-1
119.          DELTSA = DAEGR/DACEFF
120.          DENRAT = CONCB*D/(CONCD*B)
```

```
121.           DZ = .5*LENGTH/ZMAXM1
122.           DZDZ = DZ*DZ
123.           ONEMC = 1.0-C
124.           PRTDZ = (ZMAX+10)/11
125.           CONCT = .01218/(TEMP+273.0)
126.           RDGRO3 = RADGRO**3
127.           DKCOEF = .45*SQRT(8.314E+07*(TEMP+273.0)/MOLWTA)*RDGRO3/
128.          &          (1.0-PORPLO)
129.           DKA = DKCOEF*PORPLO*PORPLO/(RADGRO*RADGRO)
130.           WRITE(6,9080) DELTSA,DKA,DKCOEF
131.           WRITE(6,9090) DENRAT,DZ,PRTDZ
132.           WRITE(6,9999)
133.     C
134.     C     INITIALIZE PARAMETERS
135.     C
136.           CNVPEL = 0.0
137.           DAEOE2(1) = 1.0/(1.0/DAC+RADGRO*RADGRO/DKCOEF)
138.           DAEPL(1) = DAEOE2(1)*PORPLO*PORPLO
139.           DELTA(1) = DAEOE2(1)/DAC
140.           PORPEL = PORPLO
141.           PRTNEX = 0.0
142.           TIME = 0.0
143.           DO 50 Z=1,ZMAX
144.              CNVLOC(Z) = 0.0
145.              DAEOE2(Z) = DAEOE2(1)
146.              DAEPL(Z) = DAEPL(1)
147.              DELTA(Z) = DELTA(1)
148.              PORLOC(Z) = PORPLO
149.              RADC(Z) = RADGRO
150.              RADGR(Z) = RADGRO
151.              YACORE(Z) = YAINIT
152.              YALOC(Z) = YAINIT
153.              RAOCT(Z) = 3.0*(1-PORPLO)/RADGRO*KRXN*YACORE(Z)
154.        50 CONTINUE
155.     C
156.     C     BEGIN CALCULATION LOOP
157.     C
158.      100 CONTINUE
159.     C
160.     C     INSERT OUTPUT STATEMENTS
161.     C
162.              WRITE(6,9100) TIME,CNVPEL,PORPEL
163.           IF(TIME.GE.TIME2) DT = DT2
164.           IF(ABS(TIME-DT).LE..001) GO TO 150
165.           IF (TIME.LT.PRTNEX) GO TO 500
166.              PRTNEX = PRTNEX+PRTINT
167.      150     DO 200 Z=1,ZMAX,PRTDZ
168.      200        WRITE(6,9140) Z,YALOC(Z)
169.              WRITE(6,9999)
170.           IF (TIME.EQ.0.0) GO TO 500
171.              DO 250 Z=1,ZMAX,PRTDZ
172.      250        WRITE(6,9150) Z, YACORE(Z)
173.              WRITE(6,9999)
174.              DO 300 Z=1,ZMAX,PRTDZ
175.      300        WRITE(6,9170) Z,RADC(Z)
176.              WRITE(6,9999)
177.              DO 350 Z=1,ZMAX,PRTDZ
178.      350        WRITE(6,9180) Z,PORLOC(Z)
179.              WRITE(6,9999)
180.              DO 400 Z=1,ZMAX,PRTDZ
```

```
181.      400        WRITE(6,9190) Z,CNVLOC(Z)
182.               WRITE(6,9999)
183.               DO 450 Z=1,ZMAX,PRTDZ
184.      450         WRITE(6,9200) Z,DAEPL(Z)
185.               WRITE(6,9999)
186.      500   IF (TIME.GE.TMAX) STOP
187.      C
188.      C     SOLVE FOR THE NEW VALUES OF YALOC(Z) USING THE INTRAPELLET
189.      C     CONTINUITY EQUATION WRITTEN IN IMPLICIT DIFFERENCE FORM.
190.      C
191.      1000  CONTINUE
192.      C
193.      C     SET CONVERGENCE TEST VARIABLES
194.      C
195.            YATST(1) = YALOC(1)
196.            YATST(2) = YALOC(ZMAX/2)
197.            YATST(3) = YALOC(ZMAXM1)
198.      C
199.      C     STEP IMPLICITLY IN THE Z DIRECTION
200.      C
201.            DO 1200 Z=1,ZMAX
202.               CHI = 1.0-ONEMC*YALOC(Z)*DELTA(Z)
203.               GAMMA = CHI/DAEPL(Z)
204.               IF (Z.NE.1) GO TO 1100
205.                  TDB(1) = -2.0/DZDZ-GAMMA/PSUDT
206.                  TDC(1) = 2.0/DZDZ
207.                  TDD(1) = GAMMA*(RAOCT(Z)-YALOC(1)/PSUDT)
208.                  GO TO 1200
209.      1100        IF (Z.EQ.ZMAX) GO TO 1150
210.                  ZTERM = ((DAEPL(Z+1)-DAEPL(Z-1))/DAEPL(Z)+ONEMC
211.           &                 *DELTA(Z)/CHI*(YALOC(Z+1)-YALOC(Z-1))+ONEMC
212.           &                 *YALOC(Z)/CHI*(DELTA(Z+1)-DELTA(Z-1)))/4.0
213.                  TDA(Z) = (1.0-ZTERM)/DZDZ
214.                  TDB(Z) = -2.0/DZDZ-GAMMA/PSUDT
215.                  TDC(Z) = (1.0+ZTERM)/DZDZ
216.                  TDD(Z) = GAMMA*(RAOCT(Z)-YALOC(Z)/PSUDT)
217.                  GO TO 1200
218.      1150        TDA(ZMAX) = 0.0
219.                  TDB(ZMAX) = 1.0
220.                  TDD(ZMAX) = YABULK
221.      1200     CONTINUE
222.            CALL TRIDAG(1,ZMAX,TDA,TDB,TDC,TDD,TDV)
223.            DO 1250 Z=1,ZMAX
224.               IF (ABS(TDV(Z)-.5).GT.0.5) GO TO 7000
225.      1240     YALOC(Z) = TDV(Z)
226.               IF (YALOC(Z).GT.YABULK) YALOC(Z) = YABULK
227.      1250  CONTINUE
228.      C
229.      C     AT TIME = 0, YACORE(Z) = YALOC(Z) FOR ALL Z
230.      C
231.            IF (TIME.NE.0.0) GO TO 1350
232.               DO 1300 Z=1,ZMAX
233.                  YACORE(Z) = YALOC(Z)
234.                  RAOCT(Z) = 3.0*(1.0-PORPLO)/RADGRO*KRXN*YACORE(Z)
235.      1300     CONTINUE
236.      1350  CONTINUE
237.      C
238.      C     CHECK FOR CONVERGENCE OF PSUEDO-STEADY STATE SOLUTION
239.      C
240.            IF (ABS(YALOC(1)-YATST(1)).GT.TSTERR .OR.
```

```
241.          &    ABS(YALOC(ZMAX/2)-YATST(2)).GT.TSTERR .OR.
242.          &    ABS(YALOC(ZMAXM1)-YATST(3)).GT.TSTERR) GO TO 1000
243.     C
244.     C     CALCULATE THE NEW REACTION INTERFACE RADIUS
245.     C     THROUGHOUT THE PELLET
246.     C
247.           CNVPEL = 0.0
248.           PORPEL = 0.0
249.           DO 2400 Z=1,ZMAX
250.              IF (ABS(PORLOC(Z)-PORMIN).LT..0001) GO TO 1360
251.              RADC(Z) = RADC(Z)-DT*B*KRXN*CONCT*YACORE(Z)/CONCB
252.              IF (RADC(Z).GT.RADGRO) RADC(Z) = RADGRO
253.              IF (RADC(Z).LT.0.0) RADC(Z) = 0.0
254.     1360    CONTINUE
255.     C
256.     C     IF C = 1.0, CALCULATE YACORE(Z) USING THE EQUIMOLAR
257.     C     COUNTERDIFFUSION ANALYTIC SOLUTION
258.     C
259.              IF (C.NE.1.0) GO TO 2000
260.                 SIGMA = KRXN/DAEGR*(RADC(Z)-(RADC(Z)**2)/RADGR(Z))
261.                 YACORE(Z) = YALOC(Z)/(1.0+SIGMA)
262.                 GO TO 2300
263.     C
264.     C     CALCULATE NEW YACORE(Z) USING THE REGULA-FALSI METHOD
265.     C
266.     2000     ALPHA = ONEMC*DELTSA*KRXN*(RADC(Z)-(RADC(Z)**2)/RADGR(Z))
267.          &           /DAEGR
268.              BETA = 1.0-ONEMC*YALOC(Z)*DELTSA
269.              XL = 0.0
270.              FOFXL = 1.0-1.0/BETA
271.              XM = XL
272.              IF (ABS(FOFXL).LT.TSTERR) GO TO 2200
273.              XR = 2.0*YACORE(Z)
274.              FOFXR = EXP(ALPHA*XR)-1.0
275.              XM = XR
276.              IF (ABS(FOFXR).LT.TSTERR) GO TO 2200
277.     C
278.     C     FOFXL AND FOFXR MUST HAVE OPPOSITE SIGNS FOR THE
279.     C     METHOD TO WORK.  WE WANT XM SUCH THAT FOFXM = 0.0.
280.     C     YACORE(Z) MUST BE BETWEEN 0 AND YALOC(Z).
281.     C
282.              IF ((FOFXL*FOFXR).LE.0.0) GO TO 2050
283.                 WRITE(6,9400) XL,FOFXL,XR,FOFXR
284.                 STOP
285.     2050        DO 2150 I=1,50
286.                 XM = (XL*FOFXR-XR*FOFXL)/(FOFXR-FOFXL)
287.                 FOFXM = EXP(ALPHA*XM)-(1.0-ONEMC*DELTSA*XM)/BETA
288.                 IF (ABS(FOFXM).LT.TSTERR) GO TO 2200
289.                    IF (FOFXM*FOFXL.LT.0.0) GO TO 2100
290.                       XL = XM
291.                       FOFXL = FOFXM
292.                       GO TO 2150
293.     2100              XR = XM
294.                       FOFXR = FOFXM
295.     2150           CONTINUE
296.                    WRITE(6,9400) XL,FOFXL,XR,FOFXR
297.                    STOP
298.     2200        YACORE(Z) = XM
299.     C
300.     C     FINISH SETTING PARAMETERS
```

```
C     CALCULATE AVERAGE CONVERSION AND POROSITY FOR PELLET
C
2300     CONTINUE
         IF(ABS(PORLOC(Z)-PORMIN).LT..0001) GO TO 2305
         CNVLOC(Z) = 1.0-(RADC(Z)**3)/RDGRO3
         RADGR(Z) = RADGRO*(1.0+(DENRAT-1.0)*CNVLOC(Z))**.3333
         PORLOC(Z) = PORPLO-(1.0-PORPLO)*(DENRAT-1.0)*CNVLOC(Z)
         IF (PORLOC(Z).LT.PORMIN) PORLOC(Z) = PORMIN
         DAEOE2(Z) = 1.0/(1.0/DAC+RADGR(Z)*RADGR(Z)/DKCOEF)
         DAEPL(Z) = DAEOE2(Z)*PORLOC(Z)*PORLOC(Z)
         IF(DAEPL(Z).LT.DAEMIN) DAEPL(Z) = DAEMIN
         DELTA(Z) = DAEOE2(Z)/DAC
         RAOCT(Z) = 3.0*(1.0-PORPLO)*RADC(Z)**2/RDGRO3*KRXN
     &              *YACORE(Z)
         IF (RAOCT(Z).LT.0.0)  RAOCT(Z) = 0.0
         GO TO 2310
2305     RAOCT(Z) = 0.0
2310     IF((Z.NE.1).AND.(Z.NE.ZMAX)) GO TO 2350
         CNVPEL = CNVPEL+.5*CNVLOC(Z)
         PORPEL = PORPEL+.5*PORLOC(Z)
         GO TO 2400
2350     CNVPEL = CNVPEL+CNVLOC(Z)
         PORPEL = PORPEL+PORLOC(Z)
2400  CONTINUE
      CNVPEL = CNVPEL/ZMAXM1
      PORPEL = PORPEL/ZMAXM1
C
C     INCREMENT TIME
C
      TIME = TIME+DT
      GO TO 100
C
C     END OF CALCULATION LOOP
C
C     ------------------------------------------------------------
7000  WRITE(6,9500) Z,(TDV(Z),Z=1,ZMAX)
      STOP
8010  FORMAT(I10)
8020  FORMAT(3F10.4)
8025  FORMAT(F10.3,F10.6,F10.4)
8030  FORMAT(3E10.3)
8040  FORMAT(2F10.4,F10.7)
9010  FORMAT('1','ZMAX =',I3)
9020  FORMAT('0','B =',F4.1,4X,'C =',F4.1,4X,'D =',F4.1)
9025  FORMAT('0','CONCB =',F7.5,4X,'CONCD =',F7.5)
9030  FORMAT('0','DAC =',F6.4,4X,'DACEFF =',E10.3,4X,
     &       'DAEGR =',E10.3)
9040  FORMAT('0','DT =',F5.1,4X,'PSUDT =',F8.6,4X,'KRXN =',F6.4)
9041  FORMAT('0','DT2 =',F5.2,4X,'TIME2 =',F7.2)
9045  FORMAT('0','PORPLO =',F6.4,4X,'PORMIN =',F6.4,4X,
     &       'DAEMIN =',F6.4)
9050  FORMAT('0','PRTINT =',F4.1,4X,'LENGTH =',F5.3,4X,
     &       'RADGRO =',F8.6)
9070  FORMAT('0','TMAX =',F5.1,4X,'TSTERR =',F7.5,4X,
     &       'YABULK =',F7.5)
9075  FORMAT('0','YAINIT =',F6.4,4X,'TEMP =',F6.1,4X,
     &       'MOLWTA =',F7.2)
9080  FORMAT('0','DELTSA =',F7.4,4X,'DKA =',E10.3,4X,
     &       'DKCOEF =',E10.3)
9090  FORMAT('0','DENRAT =',F7.4,4X,'DZ =',F7.5,4X,
```

```
361.          &       'PRTDZ =', I3)
362.      9100  FORMAT('0','TIME (SEC) =',F7.1,4X,'CNVPEL =',F6.4,4X,
363.          &       'PORPEL =',F6.4)
364.      9140  FORMAT(' ','YALOC (AT Z =',I3,')  =',F7.4)
365.      9150  FORMAT(' ','YACORE (AT Z =',I3,')  =',F9.6)
366.      9170  FORMAT(' ','RADC (AT Z =',I3,')  =',F10.7)
367.      9180  FORMAT(' ','PORLOC (AT Z =',I3,')  =',F7.4)
368.      9190  FORMAT(' ','CNVLOC (AT Z =',I3,')  =',F7.4)
369.      9200  FORMAT(' ','DAEPL (AT Z =',I3,')  =',F7.4)
370.      9400  FORMAT('0','REGULA-FALSI NOT CONVERGING',4(F10.6,3X))
371.      9500  FORMAT('0','MOLEFRACTIONS TOO LARGE/SMALL AT Z =',I3,
372.          &       30(F7.4,3X))
373.      9999  FORMAT('0',F10.3)
374.            END
375.            SUBROUTINE TRIDAG (IF,L,A,B,C,D,V)
376.      C
377.      C     SUBROUTINE FOR SOLVING A SYSTEM OF LINEAR SIMULTANEOUS
378.      C     EQUATIONS HAVING A TRIDIAGONAL COEFFICIENT MATRIX. THE
379.      C     EQUATIONS ARE NUMBERED FROM IF TO L, AND THEIR SUB-DIAGONAL,
380.      C     DIAGONAL,AND SUPER-DIAGONAL COEFFICIENTS ARE STORED IN
381.      C     ARRAYS A,B,AND C. THE COMPUTED SOLUTION IS IN VECTOR V.
382.      C
383.            DIMENSION A(L),B(L),C(L),D(L),V(L),BETA(101),GAMMA(101)
384.      C
385.      C     COMPUTE ARRAYS BETA AND GAMMA
386.      C
387.            BETA(IF) = B(IF)
388.            GAMMA(IF) = D(IF)/BETA(IF)
389.            IFP1 = IF+1
390.            DO 10 I=IFP1,L
391.               BETA(I) = B(I)-A(I)*C(I-1)/BETA(I-1)
392.       10      GAMMA(I) = (D(I)-A(I)*GAMMA(I-1))/BETA(I)
393.      C
394.      C     COMPUTE FINAL SOLUTION VECTOR
395.      C
396.            V(L) = GAMMA(L)
397.            LAST = L-IF
398.            DO 20 K=1,LAST
399.               I = L-K
400.       20      V(I) = GAMMA(I)-C(I)*V(I+1)/BETA(I)
401.            RETURN
402.            END
```

XII. APPENDIX B: COMPUTER PROGRAM FOR THE ONE-DIMENSIONAL EXPANDING GRAIN MODEL WITH GRAIN SIZE DISTRIBUTION

```
1.      C
2.      C     ================================================================
3.      C
4.      C                        PROGRAM NAME: ODGMSD
5.      C
6.      C          THIS PROGRAM CONTAINS A ONE-DIMENSIONAL GRAIN MODEL
7.      C     FOR THE SIMULATION OF A SOLID-GAS REACTION WHICH MAY BE
8.      C     ACCOMPANIED BY PRODUCT EXPANSION OR CONTRACTION.  THE
9.      C     REACTING SOLID IS ASSUMED TO BE A SLAB WITH GASEOUS
10.     C     REACTANT IN CONTACT WITH THE TOP AND BOTTOM SURFACES OF
11.     C     THE SLAB.
12.     C          THE PELLET IS ASSUMED TO BE MADE UP OF GRAINS OF
13.     C     VARIOUS SIZES. THE GRAIN SIZE DISTRIBUTION IS SPECIFIED
14.     C     AS SEVERAL INITIAL GRAIN RADII WITH A GIVEN MASS FRACTION
15.     C     ASSOCIATED WITH EACH INITIAL GRAIN RADIUS.
16.     C
17.     C     ================================================================
18.     C
19.           INTEGER PRTDZ,Z,ZMAX,ZMAXM1,G,GMAX
20.           REAL ALPHA,BETA,CHI,GAMMA,SIGMA
21.           REAL B,C,D
22.           REAL CNVLOC(10,30),CNVPEL,CONCB,CONCD,CONCT,DAC,DKA,DACEFF,
23.          &     DAEOE2(30),DAEPL(30),DAEGR,DELTA(30),DELTSA,DENRAT
24.           REAL DKCOEF,DZ,DZDZ,DT,PSUDT,FOFXL,FOFXM,FOFXR,KRXN,LENGTH,
25.          &     MOLWTA,ONEMC,PORLOC(30),PORPLO,PORPEL,PORMIN,PRTINT
26.           REAL PRTNEX,RAOCT(30),RADC(10,30),RADGR(10,30),RADGRO(10),
27.          &     TDA(30),TDB(30),TDC(30),TDD(30),TDV(30),TEMP,TIME
28.           REAL TMAX,TSTERR,XL,XM,XR,YABULK,YACORE(10,30),YALOC(30),
29.          &     YAINIT,YATST(3),ZTERM,DT2,TIME2,RDGRO3(10)
30.           REAL F(10),RDAVGO,RAVGO3,CNVAVG(30),RGRAVG(30)
31.     C
32.     C     ----------------------------------------------------------
33.     C
34.     C     GLOSSARY:
35.     C
36.     C     ALPHA -- VARIABLE USED TO SIMPLIFY CALCULATIONS
37.     C     B -- STOICHIOMETRIC COEFFICIENT OF SOLID REACTANT
38.     C     BETA -- VARIABLE USED TO SIMPLIFY CALCULATIONS
39.     C     C -- STOICHIOMETRIC COEFFICIENT OF GASEOUS PRODUCT
40.     C     CHI -- VARIABLE USED TO SIMPLIFY CALCULATIONS
41.     C     CNVAVG -- AVERAGE LOCAL CONVERSION
42.     C     CNVLOC -- LOCAL CONVERSION
43.     C     CNVPEL -- OVERALL PELLET CONVERSION
44.     C     CONCB -- SOLID REACTANT CONC. (G-MOLE/CM3)
45.     C     CONCD -- SOLID PRODUCT CONC. (G-MOLE/CM3)
46.     C     CONCT -- TOTAL GAS CONC. (G-MOLE/CM3)
47.     C     D -- STOICHIOMETRIC COEFFICIENT OF SOLID PRODUCT
48.     C     DAC -- BINARY MOLECULAR DIFFUSIVITY (CM2/SEC)
49.     C     DACEFF -- EFFECTIVE BINARY DIFFUSIVITY IN PRODUCT (CM2/SEC)
50.     C     DAEGR -- EFFECTIVE DIFFUSIVITY IN PRODUCT LAYER (CM2/SEC)
51.     C     DAEOE2 -- DAEPL/PORLOC**2  (CM2/SEC)
52.     C     DAEPL -- EFFECTIVE DIFFUSIVITY OF A THROUGH PELLET (CM2/SEC)
53.     C     DELTA -- DAEPL/(DAC*PORLOC**2)
54.     C     DELTSA -- DAEGR/DACEFF
55.     C     DENRAT -- DENSITY RATIO
56.     C     DKA -- KNUDSEN DIFFUSIVITY OF A THROUGH PELLET (CM2/SEC)
57.     C     DKCOEF -- FACTOR USED TO CALCULATE DKA
58.     C     DT -- TIME INCREMENT FOR REAL TIME  (SEC)
59.     C     DT2 -- SECOND TIME INCREMENT FOR REAL TIME (SEC)
60.     C     DZ -- AXIAL INCREMENT OF LENGTH
```

```
61.      C     DZDZ -- DZ*DZ
62.      C     F -- MASS FRACTION OF A GIVEN GRAIN SIZE GROUP
63.      C     FOFXL -- FUNCTION OF XL
64.      C     FOFXM -- FUNCTION OF XM
65.      C     FOFXR -- FUNCTION OF XR
66.      C     G -- GRAIN GROUP NUMBER
67.      C     GAMMA -- CHI/DAEPL(Z)
68.      C     GMAX -- TOTAL NUMBER OF GRAIN GROUPS
69.      C     KRXN -- REACTION RATE CONSTANT (CM/SEC)
70.      C     LENGTH -- LENGTH OF PELLET (CM)
71.      C     MOLWTA -- MOLECULAR WEIGHT OF A
72.      C     ONEMC -- 1-C
73.      C     PORLOC -- LOCAL POROSITY
74.      C     PORMIN -- MINIMUM LOCAL POROSITY
75.      C     PORPEL -- PELLET POROSITY
76.      C     PORPLO -- INITIAL PELLET POROSITY
77.      C     PRTDZ -- INCREMENT FOR PRINTING LOOP
78.      C     PRTINT -- PRINTING INTERVAL (SEC)
79.      C     PRTNEX -- TIME OF NEXT PRINTOUT (SEC)
80.      C     PSUDT -- TIME INCREMENT FOR PSEUDO-TIME (SEC)
81.      C     RADC -- RADIUS OF UNREACTED CORE (CM)
82.      C     RADGR -- RADIUS OF GRAIN (CM)
83.      C     RADGRO -- INITIAL RADIUS OF GRAIN (CM)
84.      C     RAOCT -- RXN RATE PER UNIT PELLET VOL./TOTAL GAS CONC. (1/SEC)
85.      C     RAVGO3 -- RDAVGO**3
86.      C     RDAVGO -- AVERAGE INITIAL GRAIN RADIUS (CM)
87.      C     RGRAVG -- AVERAGE GRAIN RADIUS (CM)
88.      C     RDGRO3 -- RADGRO**3
89.      C     SIGMA -- VARIABLE USED TO SIMPLIFY CALCULATIONS
90.      C     TDA,TDB,TDC,TDD,TDV -- VECTORS FOR TRIDAG SUBROUTINE
91.      C     TEMP -- TEMPERATURE (CELSIUS)
92.      C     TIME -- SIMULATED TIME (SEC)
93.      C     TIME2 -- TIME AT WHICH DT = DT2 (SEC)
94.      C     TMAX -- MAXIMUM VALUE OF SIMULATED TIME (SEC)
95.      C     TSTERR -- ALLOWABLE ERROR FOR THE CONVERGENCE TEST
96.      C     XL,XM,XR -- VALUES USED IN FINDING YACORE BY REGULA-FALSI
97.      C     YABULK -- MOLE FRACTION OF A IN BULK STREAM
98.      C     YACORE -- M. F. OF A AT RXN INTERFACE
99.      C     YALOC -- M. F. OF A AT LOCAL INTRAPELLET SITES
100.     C     YAINIT -- INITIAL M. F. OF A
101.     C     YATST -- VALUE OF YALOC USED IN THE CONVERGENCE TEST
102.     C     Z -- AXIAL LENGTH SUBSCRIPT
103.     C     ZMAX -- MAXIMUM VALUE OF Z
104.     C     ZMAXM1 -- ZMAX-1
105.     C
106.     C     ------------------------------------------------------------
107.     C
108.     C     INITIALIZE CONSTANTS
109.     C
110.           READ(5,8010) ZMAX
111.           READ(5,8020) B,C,D
112.           READ(5,8020) CONCB,CONCD
113.           READ(5,8030) DAC,DACEFF,DAEGR
114.           READ(5,8025) DT,PSUDT,KRXN
115.           READ(5,8020) DT2,TIME2
116.           READ(5,8020) PORPLO,PORMIN,DAEMIN
117.           READ(5,8040) PRTINT,LENGTH
118.           READ(5,8020) TMAX,TSTERR,YABULK
119.           READ(5,8020) YAINIT,TEMP,MOLWTA
120.           READ(5,8010) GMAX
```

```
121.            DO 10 G=1,GMAX
122.               READ(5,8015) RADGRO(G),F(G)
123.         10 CONTINUE
124.            WRITE(6,9010) ZMAX
125.            WRITE(6,9020) B,C,D
126.            WRITE(6,9025) CONCB,CONCD
127.            WRITE(6,9030) DAC,DACEFF,DAEGR
128.            WRITE(6,9040) DT,PSUDT,KRXN
129.            WRITE(6,9041) DT2,TIME2
130.            WRITE(6,9045) PORPLO,PORMIN,DAEMIN
131.            WRITE(6,9050) PRTINT,LENGTH
132.            WRITE(6,9070) TMAX,TSTERR,YABULK
133.            WRITE(6,9075) YAINIT,TEMP,MOLWTA
134.            WRITE(6,9076) GMAX
135.            WRITE(6,9077) (RADGRO(G),G=1,GMAX)
136.            WRITE(6,9078) (F(G),G=1,GMAX)
137.            DO 15 G=1,GMAX
138.         15 CONTINUE
139.            ZMAXM1 = ZMAX-1
140.            DELTSA = DAEGR/DACEFF
141.            DENRAT = CONCB*D/(CONCD*B)
142.            DZ = .5*LENGTH/ZMAXM1
143.            DZDZ = DZ*DZ
144.            ONEMC = 1.0-C
145.            PRTDZ = (ZMAX+10)/11
146.            CONCT = .01218/(TEMP+273.0)
147.            DO 20 G=1,GMAX
148.               RDGRO3(G) = RADGRO(G)**3
149.         20 CONTINUE
150.            RDAVGO=0.0
151.            DO 30 G=1,GMAX
152.               RDAVGO = RDAVGO+F(G)*RADGRO(G)
153.         30 CONTINUE
154.            RAVGO3 = RDAVGO**3
155.            DKCOEF = .45*SQRT(8.314E+07*(TEMP+273.0)/MOLWTA)*RAVGO3/
156.           &         (1.0-PORPLO)
157.            DKA = DKCOEF*PORPLO*PORPLO/(RDAVGO*RDAVGO)
158.            WRITE(6,9079) RDAVGO
159.            WRITE(6,9080) DELTSA,DKA,DKCOEF
160.            WRITE(6,9090) DENRAT,DZ,PRTDZ
161.            WRITE(6,9999)
162.      C
163.      C     INITIALIZE PARAMETERS
164.      C
165.            CNVPEL = 0.0
166.            DAEOE2(1) = 1.0/(1.0/DAC+RDAVGO*RDAVGO/DKCOEF)
167.            DAEPL(1) = DAEOE2(1)*PORPLO*PORPLO
168.            DELTA(1) = DAEOE2(1)/DAC
169.            PORPEL = PORPLO
170.            PRTNEX = 0.0
171.            TIME = 0.0
172.            DO 50 Z=1,ZMAX
173.               DAEOE2(Z) = DAEOE2(1)
174.               DAEPL(Z) = DAEPL(1)
175.               DELTA(Z) = DELTA(1)
176.               PORLOC(Z) = PORPLO
177.            DO 40 G=1,GMAX
178.               CNVLOC(G,Z) = 0.0
179.               RADC(G,Z) = RADGRO(G)
180.               RADGR(G,Z) = RADGRO(G)
```

```
181.                YACORE(G,Z) = YAINIT
182.          40  CONTINUE
183.                YALOC(Z) = YAINIT
184.                RAOCT(Z) = 3.0*(1-PORPLO)/RDAVGO*KRXN*YAINIT
185.          50  CONTINUE
186.        C
187.        C     BEGIN CALCULATION LOOP
188.        C
189.         100  CONTINUE
190.        C
191.        C     INSERT OUTPUT STATEMENTS
192.        C
193.                WRITE(6,9100) TIME,CNVPEL,PORPEL
194.              IF(TIME.GE.TIME2) DT = DT2
195.              IF(ABS(TIME-DT).LE..001) GO TO 150
196.              IF (TIME.LT.PRTNEX) GO TO 500
197.                PRTNEX = PRTNEX+PRTINT
198.          150   DO 200 Z=1,ZMAX,PRTDZ
199.          200     WRITE(6,9140) Z,YALOC(Z)
200.                WRITE(6,9999)
201.              IF (TIME.EQ.0.0) GO TO 500
202.                DO 250 Z=1,ZMAX,PRTDZ
203.          250     WRITE(6,9150) Z,(YACORE(G,Z),G=1,GMAX)
204.                WRITE(6,9999)
205.                DO 300 Z=1,ZMAX,PRTDZ
206.          300     WRITE(6,9170) Z,(RADC(G,Z),G=1,GMAX)
207.                WRITE(6,9999)
208.                DO 350 Z=1,ZMAX,PRTDZ
209.          350     WRITE(6,9180) Z,PORLOC(Z)
210.                WRITE(6,9999)
211.                DO 400 Z=1,ZMAX,PRTDZ
212.          400     WRITE(6,9190) Z,(CNVLOC(G,Z),G=1,GMAX)
213.                WRITE(6,9999)
214.                DO 450 Z=1,ZMAX,PRTDZ
215.          450     WRITE(6,9200) Z,DAEPL(Z)
216.                WRITE(6,9999)
217.          500  IF (TIME.GE.TMAX) STOP
218.        C
219.        C     SOLVE FOR THE NEW VALUES OF YALOC(Z) USING THE INTRAPELLET
220.        C     CONTINUITY EQUATION WRITTEN IN IMPLICIT DIFFERENCE FORM.
221.        C
222.         1000 CONTINUE
223.        C
224.        C     SET CONVERGENCE TEST VARIABLES
225.        C
226.              YATST(1) = YALOC(1)
227.              YATST(2) = YALOC(ZMAX/2)
228.              YATST(3) = YALOC(ZMAXM1)
229.        C
230.        C     STEP IMPLICITLY IN THE Z DIRECTION
231.        C
232.              DO 1200 Z=1,ZMAX
233.                 CHI = 1.0-ONEMC*YALOC(Z)*DELTA(Z)
234.                 GAMMA = CHI/DAEPL(Z)
235.                 IF (Z.NE.1) GO TO 1100
236.                    TDB(1) = -2.0/DZDZ-GAMMA/PSUDT
237.                    TDC(1) = 2.0/DZDZ
238.                    TDD(1) = GAMMA*(RAOCT(Z)-YALOC(1)/PSUDT)
239.                    GO TO 1200
240.          1100      IF (Z.EQ.ZMAX) GO TO 1150
```

```
241.                ZTERM = ((DAEPL(Z+1)-DAEPL(Z-1))/DAEPL(Z)+ONEMC
242.          &             *DELTA(Z)/CHI*(YALOC(Z+1)-YALOC(Z-1))+ONEMC
243.          &             *YALOC(Z)/CHI*(DELTA(Z+1)-DELTA(Z-1)))/4.0
244.                TDA(Z) = (1.0-ZTERM)/DZDZ
245.                TDB(Z) = -2.0/DZDZ-GAMMA/PSUDT
246.                TDC(Z) = (1.0+ZTERM)/DZDZ
247.                TDD(Z) = GAMMA*(RAOCT(Z)-YALOC(Z)/PSUDT)
248.                GO TO 1200
249.      1150      TDA(ZMAX) = 0.0
250.                TDB(ZMAX) = 1.0
251.                TDD(ZMAX) = YABULK
252.      1200    CONTINUE
253.           CALL TRIDAG(1,ZMAX,TDA,TDB,TDC,TDD,TDV)
254.           DO 1250 Z=1,ZMAX
255.              IF (ABS(TDV(Z)-.5).GT.0.5) GO TO 7000
256.      1240    YALOC(Z) = TDV(Z)
257.              IF (YALOC(Z).GT.YABULK) YALOC(Z) = YABULK
258.      1250  CONTINUE
259.      C
260.      C     AT TIME = 0, YACORE(Z) = YALOC(Z) FOR ALL Z
261.      C
262.           IF (TIME.NE.0.0) GO TO 1350
263.              DO 1300 Z=1,ZMAX
264.                 RAOCT(Z) = 0.0
265.                 DO 1310 G=1,GMAX
266.                    YACORE(G,Z) = YALOC(Z)
267.                    RAOCT(Z) = RAOCT(Z)+F(G)*3.0*(1.0-PORPLO)/RADGRO(G)
268.          &          *KRXN*YACORE(G,Z)
269.      1310        CONTINUE
270.      1300     CONTINUE
271.      1350  CONTINUE
272.      C
273.      C     CHECK FOR CONVERGENCE OF PSUEDO-STEADY STATE SOLUTION
274.      C
275.           IF (ABS(YALOC(1)-YATST(1)).GT.TSTERR .OR.
276.          &    ABS(YALOC(ZMAX/2)-YATST(2)).GT.TSTERR .OR.
277.          &    ABS(YALOC(ZMAXM1)-YATST(3)).GT.TSTERR) GO TO 1000
278.      C
279.      C     CALCULATE THE NEW REACTION INTERFACE RADIUS
280.      C     THROUGHOUT THE PELLET
281.      C
282.           CNVPEL = 0.0
283.           PORPEL = 0.0
284.           DO 2400 Z=1,ZMAX
285.              RAOCT(Z) = 0.0
286.              DO 2500 G=1,GMAX
287.              IF (ABS(PORLOC(Z)-PORMIN).LT..0001) GO TO 1360
288.              RADC(G,Z) = RADC(G,Z)-DT*B*KRXN*CONCT*YACORE(G,Z)/CONCB
289.              IF (RADC(G,Z).GT.RADGRO(G)) RADC(G,Z) = RADGRO(G)
290.              IF (RADC(G,Z).LT.0.0) RADC(G,Z) = 0.0
291.      1360    CONTINUE
292.      C
293.      C     IF C = 1.0, CALCULATE YACORE(G,Z) USING THE EQUIMOLAR
294.      C     COUNTERDIFFUSION ANALYTIC SOLUTION
295.      C
296.              IF (C.NE.1.0) GO TO 2000
297.                 SIGMA = KRXN/DAEGR*(RADC(G,Z)-(RADC(G,Z)**2)/RADGR(G,Z))
298.                 YACORE(G,Z) = YALOC(Z)/(1.0+SIGMA)
299.                 GO TO 2300
300.      C
```

```
      C     CALCULATE NEW YACORE(G,Z) USING THE REGULA-FALSI METHOD
      C
      2000     ALPHA = ONEMC*DELTSA*KRXN*(RADC(G,Z)-(RADC(G,Z)**2)/
     &              RADGR(G,Z))/DAEGR
               BETA = 1.0-ONEMC*YALOC(Z)*DELTSA
               XL = 0.0
               FOFXL = 1.0-1.0/BETA
               XM = XL
               IF (ABS(FOFXL).LT.TSTERR) GO TO 2200
               XR = 2.0*YACORE(G,Z)
               FOFXR = EXP(ALPHA*XR)-1.0
               XM = XR
               IF (ABS(FOFXR).LT.TSTERR) GO TO 2200
      C
      C     FOFXL AND FOFXR MUST HAVE OPPOSITE SIGNS FOR THE
      C     METHOD TO WORK.  WE WANT XM SUCH THAT FOFXM = 0.0.
      C     YACORE(Z) MUST BE BETWEEN 0 AND YALOC(Z).
      C
               IF ((FOFXL*FOFXR).LE.0.0) GO TO 2050
                  WRITE(6,9400) XL,FOFXL,XR,FOFXR
                  STOP
      2050     DO 2150 I=1,50
                  XM = (XL*FOFXR-XR*FOFXL)/(FOFXR-FOFXL)
                  FOFXM = EXP(ALPHA*XM)-(1.0-ONEMC*DELTSA*XM)/BETA
                  IF (ABS(FOFXM).LT.TSTERR) GO TO 2200
                     IF (FOFXM*FOFXL.LT.0.0) GO TO 2100
                        XL = XM
                        FOFXL = FOFXM
                        GO TO 2150
      2100              XR = XM
                        FOFXR = FOFXM
      2150        CONTINUE
                  WRITE(6,9400) XL,FOFXL,XR,FOFXR
                  STOP
      2200     YACORE(G,Z) = XM
      C
      C     FINISH SETTING PARAMETERS
      C     CALCULATE AVERAGE CONVERSION AND POROSITY FOR PELLET
      C
      2300     CONTINUE
               IF(ABS(PORLOC(Z)-PORMIN).LT..0001) GO TO 2306
               CNVLOC(G,Z) = 1.0-(RADC(G,Z)**3)/RDGRO3(G)
               RADGR(G,Z) = RADGRO(G)*(1.+(DENRAT-1.0)*CNVLOC(G,Z))**.3333
               RAOCT(Z) = RAOCT(Z)+F(G)*3.0*(1.0-PORPLO)*
     &         RADC(G,Z)**2/RDGRO3(G)*KRXN*YACORE(G,Z)
      2500  CONTINUE
               CNVAVG(Z) = 0.0
               RGRAVG(Z) = 0.0
               DO 2305 G=1,GMAX
                  CNVAVG(Z) = CNVAVG(Z)+F(G)*CNVLOC(G,Z)
                  RGRAVG(Z) = RGRAVG(Z)+F(G)*RADGR(G,Z)
      2305     CONTINUE
               PORLOC(Z) = PORPLO-(1.0-PORPLO)*(DENRAT-1.0)*CNVAVG(Z)
               IF (PORLOC(Z).LT.PORMIN) PORLOC(Z) = PORMIN
               DAEOE2(Z) = 1.0/(1.0/DAC+RGRAVG(Z)*RGRAVG(Z)/DKCOEF)
               DAEPL(Z) = DAEOE2(Z)*PORLOC(Z)*PORLOC(Z)
               DELTA(Z) = DAEOE2(Z)/DAC
               IF (RAOCT(Z).LT.0.0)  RAOCT(Z) = 0.0
               GO TO 2310
      2306     RAOCT(Z) = 0.0
```

```
      2310     IF((Z.NE.1).AND.(Z.NE.ZMAX)) GO TO 2350
               CNVPEL = CNVPEL+.5*CNVAVG(Z)
               PORPEL = PORPEL+.5*PORLOC(Z)
               GO TO 2400
      2350     CNVPEL = CNVPEL+CNVAVG(Z)
               PORPEL = PORPEL+PORLOC(Z)
      2400  CONTINUE
            CNVPEL = CNVPEL/ZMAXM1
            PORPEL = PORPEL/ZMAXM1
      C
      C     INCREMENT TIME
      C
            TIME = TIME+DT
            GO TO 100
      C
      C     END OF CALCULATION LOOP
      C
      C     ------------------------------------------------------------
      7000  WRITE(6,9500) Z,(TDV(Z),Z=1,ZMAX)
            STOP
      8010  FORMAT(I10)
      8015  FORMAT(F10.7,F10.4)
      8020  FORMAT(3F10.4)
      8025  FORMAT(F10.3,F10.6,F10.4)
      8030  FORMAT(3E10.3)
      8040  FORMAT(2F10.4,F10.7)
      9010  FORMAT('1','ZMAX =',I3)
      9020  FORMAT('0','B =',F4.1,4X,'C =',F4.1,4X,'D =',F4.1)
      9025  FORMAT('0','CONCB =',F7.5,4X,'CONCD =',F7.5)
      9030  FORMAT('0','DAC =',F6.4,4X,'DACEFF =',E10.3,4X,
     &       'DAEGR =',E10.3)
      9040  FORMAT('0','DT =',F5.1,4X,'PSUDT =',F8.6,4X,'KRXN =',F6.4)
      9041  FORMAT('0','DT2 =',F5.2,4X,'TIME2 =',F7.2)
      9045  FORMAT('0','PORPLO =',F6.4,4X,'PORMIN =',F6.4,4X,
     &       'DAEMIN =',F6.4)
      9050  FORMAT('0','PRTINT =',F4.1,4X,'LENGTH =',F5.3)
      9070  FORMAT('0','TMAX =',F5.1,4X,'TSTERR =',F7.5,4X,
     &       'YABULK =',F7.5)
      9075  FORMAT('0','YAINIT =',F6.4,4X,'TEMP =',F6.1,4X,
     &       'MOLWIA =',F7.2)
      9076  FORMAT('0','GMAX =',I5)
      9077  FORMAT('0','RADGRO(G=1,GMAX) =',10(F8.6,3X))
      9078  FORMAT('0','F(G=1,GMAX) =',10(F5.3,3X))
      9079  FORMAT('0','RDAVGO =',F8.6)
      9080  FORMAT('0','DELTSA =',F7.4,4X,'DKA =',E10.3,4X,
     &       'DKCOEF =',E10.3)
      9090  FORMAT('0','DENRAT =',F7.4,4X,'DZ =',F7.5,4X,
     &       'PRTDZ =', I3)
      9100  FORMAT('0','TIME (SEC) =',F7.1,4X,'CNVPEL =',F6.4,4X,
     &       'PORPEL =',F6.4)
      9140  FORMAT(' ','YALOC (AT Z =',I3,')  =',F7.4)
      9150  FORMAT(' ','YACORE (AT Z =',I3,',G=1,GMAX) =',10F9.6)
      9170  FORMAT(' ','RADC (AT Z =',I3,',G=1,GMAX) =',10F10.7)
      9180  FORMAT(' ','PORLOC (AT Z =',I3,')  =',F7.4)
      9190  FORMAT(' ','CNVLOC (AT Z =',I3,',G=1,GMAX) =',10F7.4)
      9200  FORMAT(' ','DAEPL (AT Z =',I3,')  =',F7.4)
      9400  FORMAT('0','REGULA-FALSI NOT CONVERGING',4(F10.6,3X))
      9500  FORMAT('0','MOLEFRACTIONS TOO LARGE/SMALL AT Z =',I3,
     &       30(F7.4,3X))
      9999  FORMAT('0',F10.3)
```

```
      END
      SUBROUTINE TRIDAG (IF,L,A,B,C,D,V)
C
C     SUBROUTINE FOR SOLVING A SYSTEM OF LINEAR SIMULTANEOUS
C     EQUATIONS HAVING A TRIDIAGONAL COEFFICIENT MATRIX. THE
C     EQUATIONS ARE NUMBERED FROM IF TO L, AND THEIR SUB-DIAGONAL,
C     DIAGONAL,AND SUPER-DIAGONAL COEFFICIENTS ARE STORED IN
C     ARRAYS A,B,AND C. THE COMPUTED SOLUTION IS IN VECTOR V.
C
      DIMENSION A(L),B(L),C(L),D(L),V(L),BETA(101),GAMMA(101)
C
C     COMPUTE ARRAYS BETA AND GAMMA
C
      BETA(IF) = B(IF)
      GAMMA(IF) = D(IF)/BETA(IF)
      IFP1 = IF+1
      DO 10 I=IFP1,L
         BETA(I) = B(I)-A(I)*C(I-1)/BETA(I-1)
   10    GAMMA(I) = (D(I)-A(I)*GAMMA(I-1))/BETA(I)
C
C     COMPUTE FINAL SOLUTION VECTOR
C
      V(L) = GAMMA(L)
      LAST = L-IF
      DO 20 K=1,LAST
         I = L-K
   20    V(I) = GAMMA(I)-C(I)*V(I+1)/BETA(I)
      RETURN
      END
```